UNIVERSITY OF OKLAHOMA GRADUATE COLLEGE

DEVELOPMENT OF A COMPATIBILITY ASSESSMENT MODEL FOR EXISTING PIPELINES FOR HANDLING HYDROGEN-CONTAINING NATURAL GAS

A THESIS

SUBMITTED TO THE GRADUATE FACULTY

in partial fulfillment of the requirements for the

Degree of

MASTER OF SCIENCE

By

ZAINAB OLOLADE IYIOLA

Norman, Oklahoma

2026

DEVELOPMENT OF A COMPATIBILITY ASSESSMENT MODEL FOR EXISTING PIPELINES FOR HANDLING HYDROGEN-CONTAINING NATURAL GAS

A THESIS APPROVED FOR THE

MEWBOURNE SCHOOL OF PETROLEUM AND GEOLOGICAL ENGINEERING

BY THE COMMITTEE CONSISTING OF

Dr. Ramadan Ahmed, Chair

Dr. Catalin Teodoriu, Co-Chair

Dr. Baharak Sajjadi, Committee Member

ACKNOWLEDGMENTS

All praise is due to Almighty Allah, the Most Merciful, the Most Compassionate.

I would like to express my sincere gratitude to my advisor, Dr. Ramadan Ahmed, for giving me the opportunity to be here in the United States and for supporting my academic growth throughout my graduate studies. I am especially thankful for his mentorship, patience, and high standards, which pushed me to become a stronger researcher and professional. His guidance and encouragement enabled me to complete two master's degrees, and I remain grateful for the trust he placed in me and the opportunities he created for my development.

I also extend my appreciation to my thesis committee members, Dr. Catalin Teodoriu and Dr. Baharak Sajjadi, for their time, guidance, and thoughtful feedback. I would like to thank our graduate coordinator, Kathleen Shapiro, for her exceptional support throughout my master's program.

I am thankful to my lab colleagues, Nayem Ahmed, Samin Rythm, and Michael Larbi Gyaabeng, for their collaboration and support. To my friends, Oluchi Ejehu, Patience Ojoboh, Bilal Ibrahim, Deborah Rufus, and Chinedu Nwosu, thank you for being my rock throughout these years.

To my siblings, Barakah, Jamal, Najeebah, and Abdul Qahaar, thank you for your love, prayers, and constant support. To my parents, thank you for your sacrifices, unwavering belief in me, and your outpour of love and support.

Finally, I sincerely thank the U.S. Department of Transportation Pipeline and Hazardous Materials Safety Administration (PHMSA) for sponsoring this research (Award No. 693JK32250004CAAP), and the University of Oklahoma for institutional support.

TABLE OF CONTENTS

LIST OF TABLES

LIST OF FIGURES

ABSTRACT

Hydrogen blending in existing natural gas pipelines offers a practical pathway for using established infrastructure in emerging low-carbon energy systems. However, hydrogen exposure can degrade pipeline steels by reducing ductility and fracture toughness and accelerating fatigue crack growth, thereby raising important questions about the compatibility and remaining life of existing pipeline assets. Conventional integrity assessment methods often rely on conservative material limits or simplified assumptions and may not fully capture the combined influence of hydrogen concentration, steel grade, defect geometry, and cyclic loading on crack-driven failure. This study develops an integrated compatibility assessment model for existing pipelines transporting hydrogen-containing natural gas by coupling machine-learning-based material degradation predictions with fracture-mechanics-based integrity and lifetime assessment.

The proposed framework uses machine-learning surrogate models to predict hydrogen-sensitive degradation metrics, including reduction of area (RA), fracture toughness (FT), elongation, and fatigue crack growth behavior for API 5L pipeline steels. These predictions are integrated into stress-intensity-factor-based fracture mechanics models to simulate crack growth evolution under cyclic internal-pressure loading. The complete workflow is implemented as the University of Oklahoma Hydrogen Embrittlement Assessment Tool (OU HEAT), a graphical user interface that combines property prediction, stress intensity factor calculation, fatigue crack growth simulation, sensitivity analysis, model comparison, and integrity-relevant output visualization within a single assessment platform.

Case study evaluations were conducted on API 5L X52, X60, and X70 pipeline steels under varying hydrogen concentrations and operating conditions. The results show that predicted RA and FT generally decrease with increasing hydrogen concentration, with degradation trends approaching a plateau at higher blend levels. Remaining fatigue life also decreases significantly with increasing

hydrogen concentration, underscoring the importance of explicitly accounting for hydrogen-assisted fatigue crack growth in pipeline compatibility assessments. Sensitivity analysis further demonstrates that hydrogen concentration, material properties, defect geometry, and operating pressure can strongly influence predicted crack growth and lifetime. Model comparison with standard fatigue-curve approaches shows that the integrated framework provides physically consistent lifetime predictions across different cyclic pressure scenarios.

Overall, this study presents a scalable and practical assessment methodology for screening existing pipelines intended for hydrogen-natural gas service. By linking hydrogen-induced material degradation to crack driving forces, flaw tolerance, and remaining life, the developed framework supports more informed pipeline integrity management, inspection planning, and risk-based decision-making for hydrogen-exposed pipeline systems.

CHAPTER 1

INTRODUCTION

1.1 Overview

Hydrogen blending into existing natural gas pipeline networks is increasingly viewed as a near-term pathway for decarbonization because it can leverage large-scale, already-deployed infrastructure. However, shifting from pure natural gas service to hydrogen-containing blends introduces compatibility and integrity concerns that conventional natural gas assumptions and procedures do not fully address [1], [2]. Industry- and regulatory-focused assessments emphasize that uncertainty in materials performance and threat evolution remain among the main barriers to confident repurposing decisions [3]. A central technical risk is hydrogen embrittlement, which encompasses hydrogen-assisted degradation mechanisms that can reduce ductility and FT and accelerate fatigue crack growth in pipeline steels [2], [4]. From an integrity standpoint, these shifts can lower failure pressure, reduce tolerable defect sizes, and shorten safe inspection intervals for pipelines that previously met requirements under natural gas service [5], [6]. This concern is especially relevant for carbon and low-alloy pipeline steels commonly used in transmission systems, including API 5L grades in the X42 to X70 range, where hydrogen effects can be material-dependent and strongly influenced by the local stress state and microstructure [5], [7].

Pipeline performance in hydrogen blends must be evaluated as a system, since the limiting behavior may be governed by the most vulnerable regions, particularly weld metal and heat-affected zones. Several studies highlight that weldments can exhibit higher susceptibility than base metal because of microstructural heterogeneity, residual stress, and local hardness variation, which can magnify hydrogen assisted damage [7], [8]. This vulnerability matters for legacy infrastructure because weld quality, material pedigree, and defect populations vary widely across pipeline networks, making blanket assumptions unreliable [1], [3]. From a fracture mechanics perspective, hydrogen-related reductions in fracture resistance and increases in fatigue crack growth are especially consequential when crack-like flaws control failure. Fitness-for-service-style evaluations show that hydrogen can reduce the predicted failure pressure and the critical flaw size, particularly in regimes where fracture, rather than plastic collapse, governs the limit state [4], [9]. At the same time, mechanistic modeling continues to evolve beyond simple property knockdowns, with approaches such as hydrogen-informed damage models and virtual crack growth simulations that attempt to capture hydrogen-sensitive fracture behavior under realistic constraint conditions [8], [10]. These advances reinforce the need for compatibility assessment methods that can connect hydrogen-dependent material performance to flaw tolerance in a way that aligns with established assessment logic.

Hydrogen blending also affects cyclic integrity. Under pressure cycling, hydrogen can accelerate fatigue crack growth and reduce remaining life, which directly impacts reassessment intervals and inspection planning [6], [11]. Modeling studies for API 5L steels have shown that hydrogen-assisted crack growth can depend on loading frequency and hydrogen pressure, which suggests that operating conditions and duty cycles must be considered explicitly in life calculations [11], [12]. Experimental findings also indicate that welds can experience greater fatigue-life reduction than the base metal under hydrogen exposure, supporting the need for conservative treatment of welded regions in integrity workflows [7]. In addition to fracture and fatigue, pipeline integrity decisions often involve interacting threats such as corrosion, which can coexist with hydrogen effects in older pipelines. Recent work has extended numerical and data-driven approaches to evaluate burst strength and remaining life of corroded pipelines under hydrogen-blend conditions, with results indicating that hydrogen-induced strength reduction can be more pronounced in higher-strength steels than in lower-grade steels under certain conditions [5]. This motivates compatibility models that can handle realistic defect morphologies and prioritize crack-like flaws, weld anomalies, and high-consequence segments.

Given these technical drivers, this work develops a compatibility assessment model for existing pipelines intended to transport hydrogen-containing natural gas. The model integrates data-driven predictions of hydrogen-sensitive material properties, including reduction of area, fracture toughness, and fatigue crack growth behavior, with a fracture mechanics-based integrity evaluation consistent with ASME fitness-for-service principles, thereby supporting engineering screening and decision-making across hydrogen blend levels [9], [13]. Recent literature suggests that improved assessment fidelity may require representing hydrogen effects beyond a single conservative toughness value, including accounting for gradients in hydrogen-affected toughness through the wall and recognizing the limitations of standard failure assessment methods near welds and in regions of residual stress [8], [14]. Building on these insights, the compatibility assessment framework developed in this study is structured to link machine-learning-informed hydrogen degradation trends to crack driving forces, crack growth evolution, and remaining-life metrics that are directly actionable for pipeline integrity management [5], [15].

1.2 Statement of the Problem and Motivation

The introduction of hydrogen into existing natural gas pipeline systems presents a fundamental assessment challenge rather than a purely design problem. While hydrogen blending is widely promoted as a transitional decarbonization strategy that leverages existing infrastructure, the majority of in-service pipelines were neither qualified nor evaluated for hydrogen exposure during their original design life [1], [2]. As a result, operators lack a clear, quantitative basis for determining whether pipelines that have demonstrated acceptable performance under natural gas service remain fit for continued operation when hydrogen is introduced [3], [5]. At the core of this challenge is hydrogen embrittlement, which alters the mechanical response of pipeline steels by reducing ductility and fracture toughness and accelerating fatigue crack growth [4], [16]. These degradation mechanisms can shift governing failure modes from plastic collapse toward fracture-controlled behavior, particularly in the presence of sharp defects, thereby reducing allowable operating margins [5], [9]. Consequently, integrity assessments that implicitly assume natural-gas-based material behavior may underestimate fracture risk when hydrogen-containing gas is transported, even at moderate blend levels [2].

This problem is exacerbated by the heterogeneity of legacy pipeline systems. Transmission networks include a wide range of API 5L steel grades, including X42, X52, X60, X70, X80, and X100, spanning low- to high-strength classes and produced across multiple decades using different manufacturing and welding practices [1], [5]. Hydrogen embrittlement susceptibility depends strongly on local microstructure, stress state, and hydrogen exposure conditions, so pipeline integrity may be governed by localized weak regions rather than nominal base metal properties [7], [8]. In such cases, uniform conservative assumptions can obscure defect-specific risks and lead to either unsafe operation or unnecessary restriction of viable infrastructure. Existing fitness-for-service methodologies provide a structured framework for assessing flaws in pressurized components, but their direct application to hydrogen service remains challenging. Fracture mechanics-based assessments, grounded in API 579-1 and ASME FFS concepts, indicate that hydrogen exposure can significantly reduce the critical flaw size and failure pressure, particularly when fracture resistance governs the limit state [4], [9]. Under these conditions, lower-level assessments may no longer be sufficient, and more detailed treatment of crack geometry, residual stresses, and hydrogen-affected material properties becomes necessary [8], [17]. However, such higher-fidelity evaluations are often computationally intensive and impractical for large-scale screening of existing pipeline assets.

The challenge extends beyond static integrity considerations. Hydrogen exposure also alters time-dependent damage processes. Under cyclic pressure loading, hydrogen can substantially accelerate fatigue crack propagation and shorten remaining service life, directly affecting reassessment intervals and inspection planning [6], [11]. The magnitude of hydrogen-assisted fatigue degradation depends on interacting variables such as hydrogen concentration, loading frequency, stress-intensity range, and steel grade, making it difficult to capture with simplified deterministic rules or a single safety factor [12]. This limits the effectiveness of assessment approaches that focus solely on burst pressure or short-term failure criteria. Although standards such as ASME B31.12 provide guidance for hydrogen pipeline design and repurposing, they largely rely on conservative material limits and do not explicitly quantify the combined effects of hydrogen embrittlement, defect characteristics, and cyclic loading on structural integrity [9]. At the same time, system-level hydrogen-blending studies and network-planning tools address feasibility and compliance at a high level but do not replace the need for defect-specific integrity evaluations required for pipeline operation and regulatory compliance [1]. This disconnect highlights a critical gap between hydrogen-blending strategies and actionable integrity-management decisions for existing pipelines.

Further limitation arises from the increasing volume and complexity of hydrogen embrittlement data. Experimental and numerical studies have generated extensive datasets linking hydrogen concentration, steel chemistry, mechanical response, fracture toughness degradation, and fatigue crack growth behavior across multiple pipeline steel grades [10], [16]. Integrating this multidimensional information into conventional fracture mechanics workflows remains challenging, particularly when rapid evaluation across multiple blend scenarios and material conditions is required. These challenges motivate the incorporation of machine-learning into hydrogen compatibility assessment. Data-driven models offer the ability to capture nonlinear relationships between hydrogen exposure conditions and material degradation, enabling efficient prediction of RA, FT, and fatigue crack growth behavior across a broad parameter space [14], [15]. When combined with physics-based fracture mechanics, machine learning provides a practical means to translate complex material behavior into assessment-ready inputs while maintaining consistency with established integrity evaluation frameworks.

Motivated by these gaps, this study develops a compatibility assessment model for existing pipelines transporting hydrogen-containing natural gas that integrates machine-learning-based material property predictions with fracture mechanics-based fitness-for-service evaluation, consistent with the ASME FFS methodology. The goal is to provide a structured and scalable framework that links hydrogen-dependent degradation in ductility, FT, and fatigue crack growth to crack driving forces, flaw tolerance, and remaining life metrics, thereby directly supporting pipeline integrity management decisions.

1.3 Objectives of the Study

The principal objective of this study is to develop a compatibility assessment model for existing pipelines transporting hydrogen-containing natural gas by integrating machine–learning–based predictions of hydrogen-induced material degradation with fracture-mechanics-based fitness-for-service evaluation.

The specific objectives are to:

i. Develop machine-learning surrogate models that predict hydrogen-induced degradation metrics in pipeline steels, including RA, FT, elongation, and fatigue crack growth behavior under hydrogen-natural gas blending conditions.
ii. Integrate machine learning–predicted material degradation with stress intensity factor–based fracture mechanics models to simulate crack growth evolution and evaluate pipeline integrity outcomes, including stress intensity response, crack growth rates, critical crack depth, remaining life, and fatigue life under cyclic loading conditions.
iii. Quantify the effects of hydrogen exposure and operating conditions on the mechanical and fracture response of API 5L pipeline steels, focusing on grades X52, X60, and X70 across relevant hydrogen-natural gas blend levels.
iv. Conduct sensitivity analysis to determine the relative impact of material properties, hydrogen blend level, defect geometry, and operating parameters on predicted integrity outcomes and to identify the dominant drivers of risk within the proposed framework.

1.4 Significance of the Work

This work provides a practical pathway for evaluating whether existing natural gas transmission pipelines can safely accommodate hydrogen blending, a key near-term decarbonization strategy. By integrating machine-learning-based predictions of hydrogen-induced degradation with stress-intensity-factor-based fracture mechanics, the proposed framework connects material property deterioration to the crack-driving conditions that govern structural integrity, thereby overcoming the limitations of using purely data-driven or purely mechanistic models in isolation. The approach translates predicted changes in RA, FT, and fatigue crack growth behavior into integrity-relevant outcomes, including stress intensity response, crack growth evolution, critical crack depth, and remaining life under cyclic loading, which are directly useful for integrity management decisions. In addition, the framework reduces reliance on extensive experimental campaigns by enabling efficient evaluation across multiple API 5L steel grades, hydrogen natural gas blend levels, operating conditions, and defect geometries, while the sensitivity analysis clarifies which parameters most strongly influence predicted integrity outcomes and therefore where inspection, mitigation, and operational controls should be prioritized. Collectively, the study contributes a scalable assessment methodology that supports safer implementation of hydrogen blending in pipeline systems and provides a foundation for improving engineering guidance and risk-informed decision-making for hydrogen-exposed pipeline operation.

1.5 Methodology Overview

This study adopts an integrated methodology that combines data driven machine-learning with fracture mechanics-based integrity modeling to assess the compatibility of existing pipelines with hydrogen containing natural gas. A curated dataset from experimental measurements and relevant literature is used to train machine-learning surrogate models that predict key hydrogen induced degradation metrics in API 5L pipeline steels across representative hydrogen-natural gas blend levels and operating conditions. These machine-learning predictions are then coupled with a stress intensity factor-based crack driving force formulation and implemented within a fatigue crack growth simulation framework to model crack evolution under cyclic loading and estimate integrity outcomes such as stress intensity response, crack growth progression, critical crack depth, final number of cycles, and remaining life in hours and years. To evaluate how uncertainty in selected inputs influences integrity predictions, the framework includes a sensitivity module that runs three comparative cases: baseline, -25% of baseline, and +25% of baseline perturbations of a chosen parameter and summarizes the resulting shifts in predicted degradation and life outcomes. Finally, the complete assessment workflow is packaged into a graphical user interface to support practical use for screening studies and pipeline integrity decision-making.

1.6 Outline

The structure of this study is organized to present a clear, end-to-end compatibility assessment framework for pipelines transporting hydrogen-containing natural gas. CHAPTER 1 introduces research overview, motivation, objectives, significance, and a high-level description of the methodology and thesis organization. CHAPTER 2 provides a comprehensive literature review covering the fundamentals of hydrogen embrittlement; mechanisms of hydrogen transport and damage in pipeline steels; conditions that influence embrittlement; and documented degradation in ductility, FT, and fatigue crack growth. It also reviews fracture mechanics-based integrity assessment approaches, experimental methods used in hydrogen embrittlement studies, and recent machine-learning applications, while identifying key knowledge gaps that motivate this work.

CHAPTER 3 describes the development and validation of the machine-learning framework, including data sources and preprocessing; input features and target variables; model selection; training; and performance evaluation for predicting reductions in area, FT, and fatigue crack growth rate. CHAPTER 4 presents the fracture mechanics-based integrity and lifetime assessment methodology, including crack geometry and loading characterization, stress-intensity-factor solutions, fatigue crack growth formulation, failure and termination criteria, and the overall lifetime prediction procedure. CHAPTER 5 integrates the machine-learning and fracture mechanics components into the developed assessment tool, presents case-study applications, validation results, sensitivity analysis, and robustness comparisons, and discusses the engineering implications for pipeline integrity decision-making. Finally, CHAPTER 6 summarizes the study's main conclusions and provides recommendations for future research and practical deployment.

CHAPTER 2

LITERATURE REVIEW

2.1 Definitions and Fundamentals of Hydrogen Embrittlement (HE)

Hydrogen embrittlement (HE) refers to the deterioration of the mechanical properties of a metallic material caused by interaction with hydrogen in atomic or molecular form. Specifically, HE manifests as reduced RA, FT, and resistance to fatigue crack growth, even in materials that retain their yield and tensile strength under the same conditions [20], [21]. First formally documented by William Johnson in 1875, HE has been studied extensively for over a century and remains an active area of research owing to the complexity of its operating mechanisms and its sensitivity to material, environmental, and loading conditions [22], [23]. The growing interest in hydrogen as a clean energy carrier, and in particular the repurposing of existing natural gas pipelines for hydrogen-natural gas blend transport, has renewed the urgency of understanding and quantifying HE for engineering applications [24], [25].

HE is broadly classified into three categories based on the source of hydrogen and the conditions under which damage occurs, as summarized in Table 2.1. Internal Hydrogen Embrittlement (IHE) occurs when hydrogen is introduced into the material during manufacturing or processing operations such as welding, electroplating, or acid pickling, and subsequently diffuses under residual or applied stress [26]. Hydrogen Environment Embrittlement (HEE) occurs when a material is simultaneously stressed and exposed to a hydrogen-containing gas or liquid, with hydrogen absorbed continuously at the surface during loading [21], [27]. A third category, Hydrogen Reaction Embrittlement, involves chemical reaction of hydrogen with alloying elements to form brittle hydride phases, but this is generally secondary for ferritic pipeline steels [22]. For pipelines repurposed to transport hydrogen-natural gas blends, HEE under cyclic operational loading is the governing damage mode [24].

Table 2-1 Classification of Hydrogen Embrittlement

HE Type	Hydrogen Source	Operative Condition	Pipeline Relevance
Internal HE (IHE)	Processing: welding, plating, pickling	Residual or applied stress post-fabrication	Weld regions in legacy pipelines
Hydrogen Environment Embrittlement (HEE)	External gas or electrolyte environment	Simultaneous hydrogen exposure and mechanical loading	Primary concern for H2-NG blend service
Hydrogen Reaction Embrittlement	Reaction with alloying elements	Formation of brittle hydride phases	Secondary; not dominant in ferritic steels

Source: [21], [22], [26].

HE is an inherently multi-factorial phenomenon that requires the simultaneous presence of three conditions: a susceptible material, a hydrogen-containing environment, and applied or residual tensile stress [26], [28]. The absence of any one of these three conditions prevents embrittlement from occurring. This is illustrated schematically in Figure 2.1, a widely adopted conceptual representation in the hydrogen embrittlement literature [21], [28]. For pipeline repurposing scenarios, all three conditions coexist: ferritic pipeline steels are inherently susceptible, pressurized hydrogen-natural gas blends constitute the hydrogen environment, and operational pressure cycling and weld residual stresses provide the mechanical loading [4], [24].

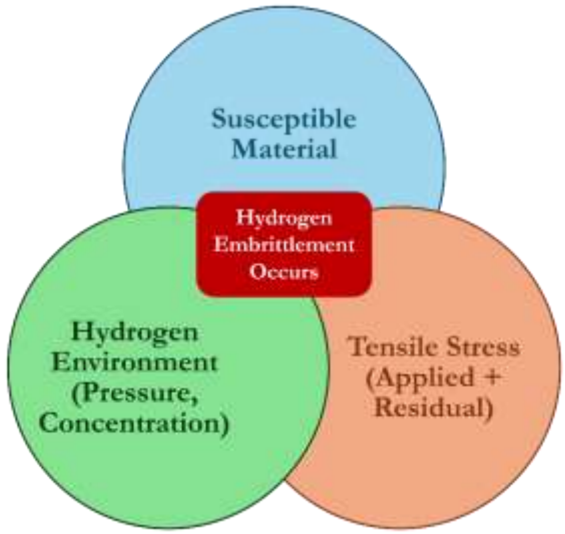

Figure 2-1 The Three critical conditions required for hydrogen embrittlement to occur: susceptible material, hydrogen environment, and tensile stress. Adapted from [28]

At the macroscopic level, HE in pipeline steels is most clearly evidenced by a reduction in ductility under tensile loading. As illustrated in Figure 2.2, specimens tested in 20% and 100% hydrogen environments fracture at substantially lower displacements compared to those tested in the inert CH_4 reference, while yield strength and ultimate tensile strength remain largely unchanged across all test conditions [27], [29], [30]. This characteristic signature means that conventional strength-based qualification tests conducted in air do not capture HE susceptibility. The severity of ductility loss is commonly quantified using the Embrittlement Index (EI), defined in terms of RA as:

$$EI\ (\%) = \left[\frac{(RA_{air} - RA_{H2})}{RA_{air}}\right] x\ 100\% \tag{2-1}$$

Where RA_{air} and RA_{H2} are the RA values measured in an inert environment and in hydrogen, respectively [28], [31]. Higher EI values indicate greater susceptibility. For the API 5L grades of interest in this study, reported EI values range from approximately 5% for X42 to over 30% for X80 in pure hydrogen environments, reflecting the general trend of increasing susceptibility with steel strength grade [23], [28].

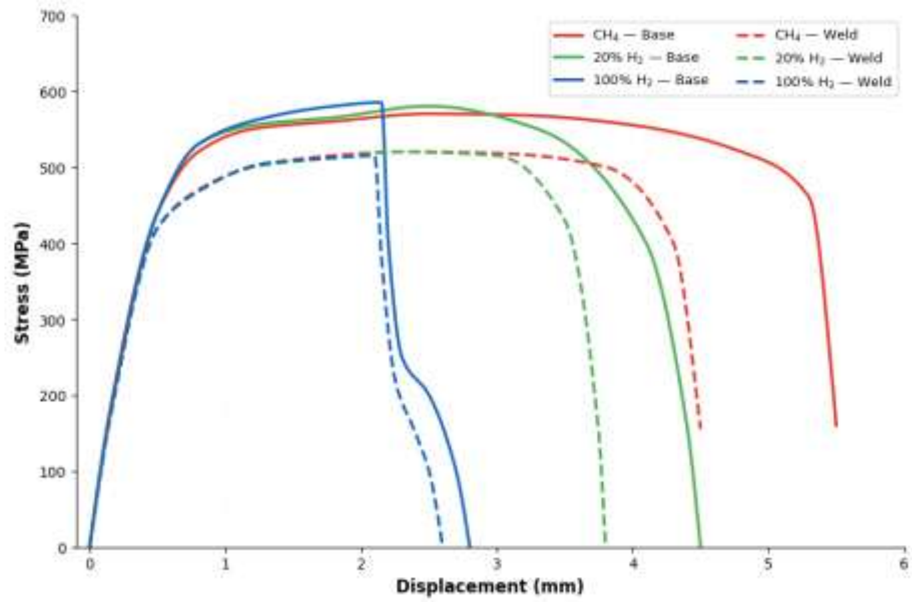

Figure 2-2 Stress-displacement curves for API 5L X60 pipeline steel base material (solid lines) and welded material (dashed lines) tested in CH4, 20% H2, and 100% H2 at 2.07 MPa using slow strain rate tensile testing, showing preserved yield and tensile strength alongside progressive reduction in displacement to fracture with increasing hydrogen concentration. Redrawn from [29]**.**

At the microscale, hydrogen-induced damage is reflected in a transition in fracture surface morphology. In air, pipeline steels fracture with ductile cup-and-cone morphology dominated by microvoid coalescence. Under hydrogen exposure, the fracture mode shifts to quasi-cleavage and intergranular features, as shown in Figure 2.3, consistent with the operation of hydrogen-assisted crack tip damage mechanisms discussed in Section 2.4 [22], [27]. In the gaseous HEE scenario relevant to pipeline service, hydrogen uptake into the steel is governed by Sievert's law:

$$C_H = K_S \sqrt{P_{\{H2\}}} \qquad 2\text{-}2$$

Where C_H is the subsurface hydrogen concentration, K_S is the Sievert's constant for the steel, and P_{H2} is the hydrogen partial pressure [22], [33]. This square-root dependence means that increasing the hydrogen blend fraction raises the hydrogen concentration in the steel nonlinearly, with implications for how blend level influences degradation severity across pipeline operating pressure ranges.

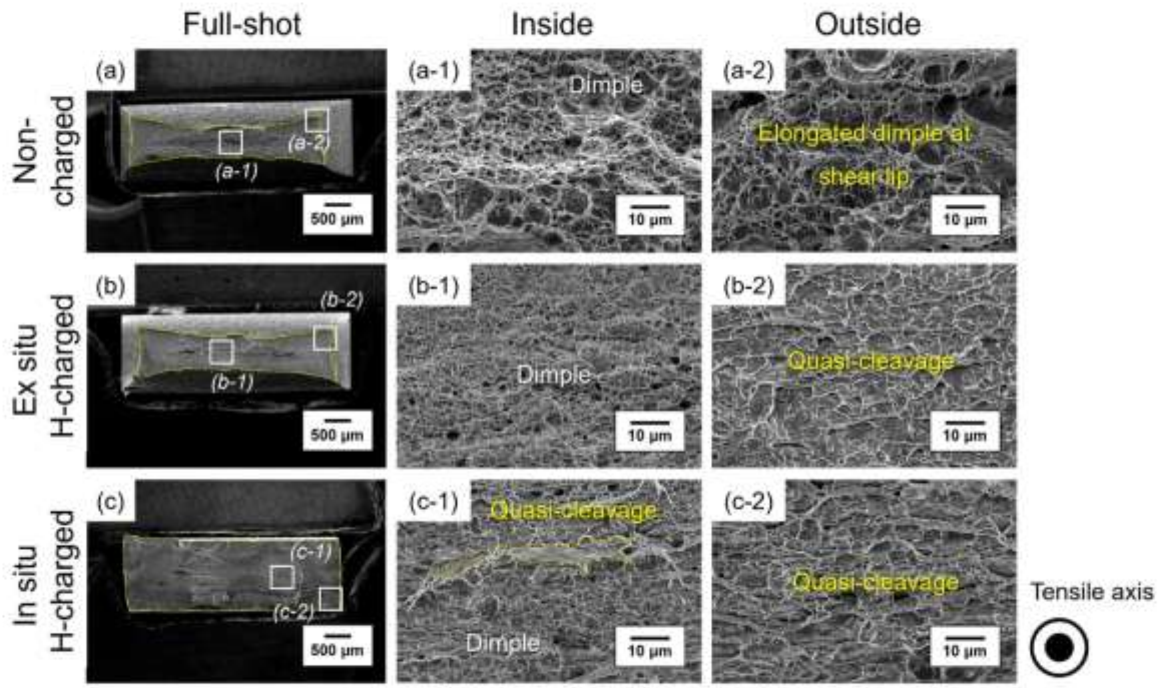

Figure 2-3 SEM fractographs of API 5L X70 pipeline steel fracture surfaces under (a) uncharged, (b) ex situ hydrogen-charged, and (c) in situ hydrogen-charged conditions [34].

The transition from ductile to brittle fracture morphology under hydrogen exposure is clearly evidenced at the microscopic level. As shown in Figure 2.3, SEM fractographs of API 5L X70 pipeline steel reveal equiaxed dimples characteristic of ductile micro-void coalescence in the uncharged condition, progressively transitioning to quasi-cleavage fracture features under ex situ and in situ hydrogen charging, with the most severe brittle morphology observed across the entire fracture surface under in situ conditions [34].

Hydrogen embrittlement is a system-level degradation process driven by the synergistic interaction of material susceptibility, hydrogen exposure, and mechanical loading. For pipeline repurposing, HE under cyclic pressurization is the dominant degradation mechanism, and a complete characterization of HE severity requires evaluating ductility loss, FT reduction, and fatigue crack growth acceleration in combination. The specific environmental and material factors that govern HE severity in API 5L pipeline steels are reviewed in Sections 2.2 and 2.3, while the operative damage mechanisms are examined in detail in Section 2.4.

2.2 Hydrogen Embrittlement in Pipeline Steels

Pipeline steels used in natural gas transmission belong predominantly to the API 5L series, a family of high-strength low-alloy (HSLA) steels classified by their specified minimum yield strength (SMYS). Their susceptibility to hydrogen embrittlement (HE) increases systematically with strength grade, governed primarily by microstructural character. Lower grades such as X42 are generally accepted as non-susceptible under service conditions, while grades from X60 upward exhibit measurable ductility loss and FT degradation on hydrogen exposure [5]. Table 2.2 summarizes the key HE characteristics of the grades most relevant to transmission and blending applications.

Table 2-2 API 5L Pipeline Steel Grades and Their Hydrogen Embrittlement Susceptibility Characteristics.

Grade	SMYS (MPa)	Microstructure	HE Susceptibility	Application
X42	290	Ferrite-pearlite	Low; not susceptible in practice	Distribution mains
X52	359	Ferrite-pearlite	Low to moderate; HEI rises with temperature	Legacy transmission lines
X60	414	Ferrite-bainite	Moderate; HEI ~12-18% at 20-100% H2	Transition-era transmission
X65	448	Acicular ferrite / bainite	Moderate to high; more sensitive than X52	Modern long-distance lines
X70	483	Bainite / acicular ferrite (TMCP)	High; brittle fracture shift at 0.7% H2	High-pressure transmission
X80	552	Low-carbon bainite / M-A constituent	High; FT reduced up to 32%	High-pressure trunk lines
X100	690	Tempered martensite / bainite	Very high; clear SSRT embrittlement	Ultra-high-pressure pipelines

SMYS = Specified Minimum Yield Strength; TMCP = Thermomechanical Controlled Processing; M-A = Martensite-Austenite constituent; HEI = Hydrogen Embrittlement Index.

The microstructural transitions that accompany increasing grade are central to understanding this susceptibility gradient. The soft ferrite-pearlite banding of X52 offers relatively few irreversible trap sites, limiting hydrogen accumulation at critical locations. By contrast, the low-carbon bainitic and martensite-austenite (M-A) microstructures of X70 and X80 present higher dislocation densities and greater hydrogen trap concentrations, facilitating localized damage under stress. Kim *et al.,* 2022 [30] demonstrated for X80 that hydrogen exposure substantially reduces ductility and accelerates subcritical crack propagation, while for X70 the literature records a shift from ductile to brittle fracture at hydrogen concentrations as low as 0.7 vol% in a mixed gas environment [27].

Weld regions consistently show higher susceptibility than parent metal across all grades, owing to microstructural gradients in the heat-affected zone (HAZ), locally elevated hardness, and residual stress. Stalheim *et al.,* 2010 [29] quantified this for X60, finding that welded material recorded a hydrogen embrittlement index (HEI) of 14.6% at a 20% hydrogen blend and 18.0% under pure hydrogen at 2.07 MPa, compared to 11.6% and 12.4% for the base material under the same conditions. Notably, strength and stiffness were unaffected, with ductility loss being the primary manifestation of damage. Figure 2.4 presents these HEI values by material condition, illustrating that even low hydrogen concentrations produce embrittlement levels approaching those of pure hydrogen service.

Figure 2-4 Hydrogen Embrittlement Index (HEI) of API 5L X60 base and welded materials at 20% and 100% H_2 at 2.07 MPa, measured by hollow-specimen slow strain rate tensile testing. Data sourced from [29].

These findings establish a clear susceptibility hierarchy across the API 5L range, with weld zones representing particularly high-risk locations regardless of grade. The environmental and loading conditions that govern the severity of hydrogen uptake and the onset of degradation are examined in detail in Section 2.3.

2.3 Conditions Influencing Hydrogen Embrittlement

Hydrogen embrittlement is not a fixed material property but a condition-dependent outcome. Its severity in pipeline steel depends on the interplay among environmental exposure conditions, the material's inherent susceptibility, and the stress and loading regime acting on the structure. These three domains are examined separately in the subsections below, as each exerts a distinct and often non-linear influence on the rate of hydrogen uptake, accumulation, and mechanical damage.

2.3.1 Environmental Conditions

The principal environmental driver of hydrogen embrittlement in pipeline steels is the hydrogen fugacity at the steel surface, a thermodynamic quantity that accounts for the non-ideal behavior of gaseous hydrogen at elevated pressures and more accurately reflects the effective chemical potential driving hydrogen entry than total pressure alone. Michler *et al.,* 2021 [35] compiled FT and tensile data across a range of API 5L grades and concluded that results from hydrogen-natural gas blend environments and from pure hydrogen environments at equivalent fugacity are broadly equivalent, confirming that fugacity governs hydrogen uptake rather than the nominal hydrogen fraction. Below a fugacity threshold of approximately 1.2 MPa, smooth tensile specimens typically show reduction-of-area values near 100%, suggesting negligible degradation. Above this threshold, ductility and toughness losses increase markedly.

Temperature introduces a further complication. Rather than a simple monotonic relationship, hydrogen embrittlement severity peaks within a critical temperature range close to room temperature. For X70 pipeline steel under controlled cathodic hydrogen charging, Xing *et al.,* 2024 [36] identified a most severe temperature threshold of 20°C at moderate charging intensities, with HE weakening both below and above this temperature. The low-temperature limit arises from reduced hydrogen diffusivity, which slows accumulation at crack tips; at higher temperatures, thermally assisted recovery mechanisms begin to counteract hydrogen damage.

The composition of the gas stream also plays a controlling role, particularly the presence of trace impurity species. Oxygen acts as a potent inhibitor of hydrogen embrittlement: O_2 molecules adsorb competitively on the steel surface and impede the dissociation of H_2 into atomic hydrogen, thereby reducing the flux of hydrogen into the lattice. In fatigue crack growth tests on L360 pipeline steel, Zhou *et al.,* 2024 [32] demonstrated that O_2 strongly mitigated hydrogen-promoted crack propagation, and that when O_2 and CO_2 were simultaneously present in the hydrogen stream, the inhibitory action of O_2 dominated. CO_2, by contrast, promotes hydrogen uptake through surface reactions that enhance hydrogen permeation. The qualitative and quantitative significance of these impurity gas interactions is illustrated through the grade-level FT data in Figure 2.5, which shows that even in pure hydrogen at 6.9 MPa, reductions of 18–45% are observed across API 5L grades [38], [39], underscoring why even partial mitigation through O_2 addition carries meaningful structural consequences. Figure 2.5 shows the FT reduction (%) of API 5L pipeline steels at 6.9 MPa gaseous hydrogen relative to air, tested in situ per ASTM E1820. Values for X42 (40%) and X52 (37%) are explicitly reported by Gangloff and Somerday, 2012 [40]. Values for X60 (~45%) and X70 (~18%) are derived from Cialone and Holbrook, 1988 [41], as compiled in San March *et al.,* 2010 [42]. Error bars indicate inter-specimen scatter.

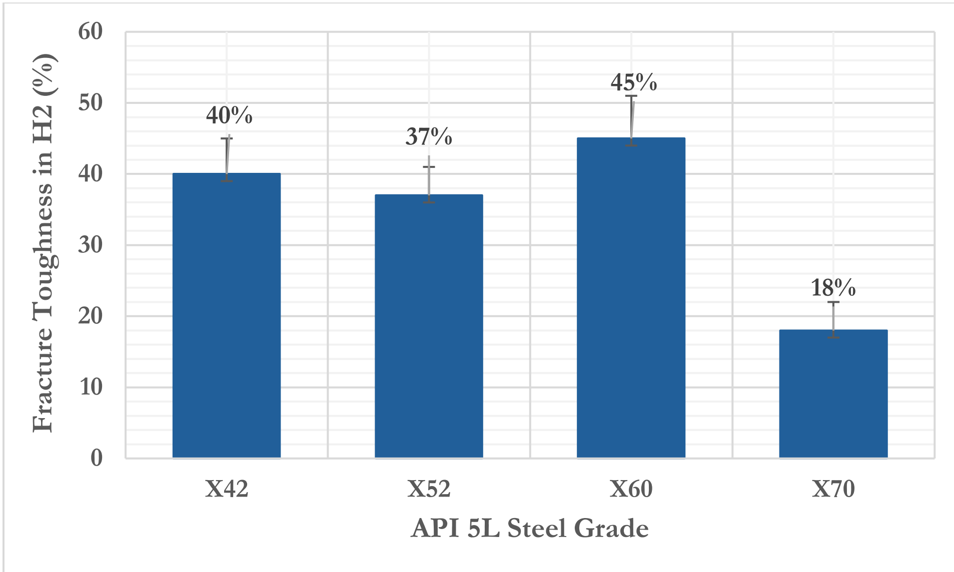

Figure 2-5 FT reduction (%) of API 5L pipeline steels at 6.9 MPa gaseous hydrogen relative to air, tested in situ per ASTM E1820.

2.3.2 Material Susceptibility

The intrinsic susceptibility of a pipeline steel to hydrogen embrittlement is governed primarily by its microstructure and mechanical strength. Across the API 5L grade family, susceptibility increases systematically with yield strength, though the relationship is not strictly linear and is strongly mediated by the specific microstructural phases present. Figure 2.6 illustrates elongation losses across X52, X65, and X100 tested under identical conditions by Nanninga *et al.,* 2012 [27] at 13.8 MPa gaseous hydrogen. X52 exhibits approximately 22% elongation loss, rising to 28% for X65 and 50% for X100, reflecting the increasing dislocation density and hydrogen trap concentration associated with higher-strength tempered martensitic microstructures [27].

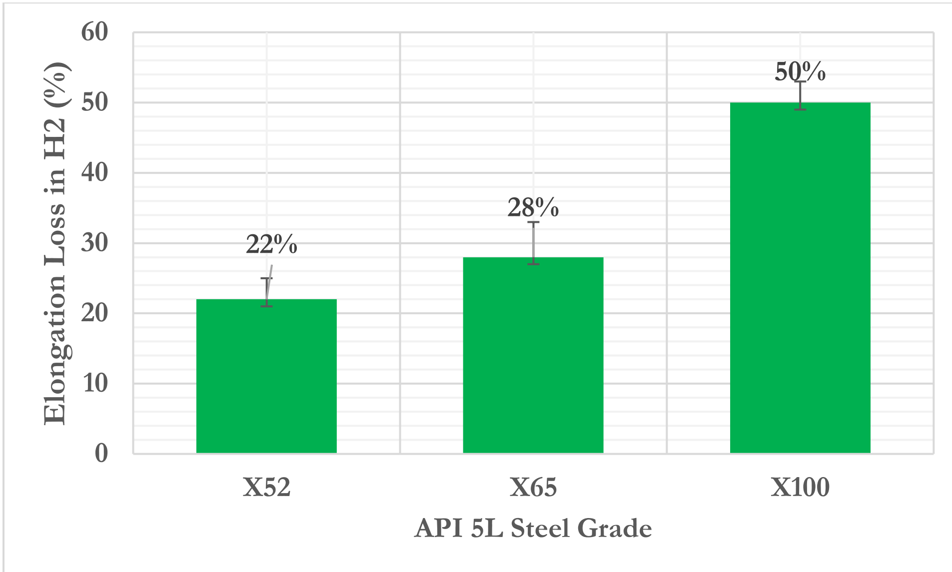

Figure 2-6 Elongation loss (%) of API 5L X52, X65, and X100 pipeline steels tested in 13.8 MPa gaseous hydrogen relative to air, measured by slow strain rate tensile testing at a strain rate of 7×10^{-3} s^{-1}. Data Source: [27].

The microstructural phase composition determines both the density of irreversible hydrogen traps and the ease of diffusion. Ferrite-pearlite banding in lower grades (X42, X52) offers few reversible trap sites and moderate hydrogen diffusivity, limiting local hydrogen accumulation. In higher grades, thermomechanical processing produces acicular ferrite, bainite, and martensite-austenite (M-A) constituents. These phases exhibit elevated dislocation densities and subgrain boundaries that trap hydrogen more effectively, concentrating it near regions of high stress triaxiality. Bainitic microstructures typical of X70 and X80 show intermediate diffusivity, while the tempered martensite of X100 offers the most severe combination of trap density and stress amplification at crack tips [38]. Material hardness, closely correlated with yield strength, is an additional amplifier: this is the basis for ASME B31.12 imposing a maximum weld heat-affected zone hardness of HV250 as a practical control against hydrogen-induced cracking initiation in pipeline welds.

Weld regions and their heat-affected zones deserve particular note. As demonstrated for X60 in Section 2.2, HAZ microstructures consistently exhibit higher hydrogen embrittlement susceptibility than adjacent base metal, owing to steep microstructural gradients, locally elevated hardness, and residual tensile stresses introduced during fabrication. For X70, Alvaro *et al.,* 2014 [44] established that the critical hydrogen pressure for the onset of HE in the HAZ was between 0.1 and 0.6 MPa, considerably lower than in the base metal, confirming that welds represent the first failure locus even in otherwise moderate-susceptibility grades.

2.3.3 Influence of Stress and Loading

Stress state and loading history interact with hydrogen exposure through a well-established coupling mechanism: applied tensile stress increases the hydrostatic pressure ahead of a crack tip, which, in turn, attracts hydrogen atoms via diffusion down a chemical potential gradient [45]. Hydrogen accumulates preferentially at the region of maximum stress triaxiality, weakening atomic bonds and facilitating either decohesion or localized plastic instability [45]. This diffusion-driven accumulation is time-dependent, which is why loading rate has a profound effect on observed HE severity. At lower strain rates, more time is available for hydrogen to diffuse to the crack tip before fracture occurs, maximizing damage [46]. This underpins the use of slow-strain-rate tensile (SSRT) testing at strain rates of 10^{-5} to 10^{-6} s^{-1} as the standard laboratory method for conservatively assessing hydrogen embrittlement susceptibility in pipeline steels [46].

Under cyclic loading, hydrogen embrittlement manifests most severely through hydrogen-assisted fatigue crack growth (HA-FCG), where the presence of hydrogen simultaneously lowers the threshold stress intensity range (ΔK_{th}) required to initiate crack growth and elevates fatigue crack growth rates (FCGR) across all stress intensity ranges [46]. Figure 2.7 illustrates this schematically: in

Region I, the threshold for crack growth is reduced, so pre-existing defects that would be benign in air can begin to propagate in hydrogen; in Region II, crack growth rates are substantially higher than in air for the same ΔK, with reported acceleration factors of 10 to 150 times depending on grade, pressure, and frequency [45], [46]. For X42 pipeline steel at 6.9 MPa hydrogen, baseline fatigue crack growth rates near the threshold were up to 150 times those observed in nitrogen at the same stress-intensity range [41].

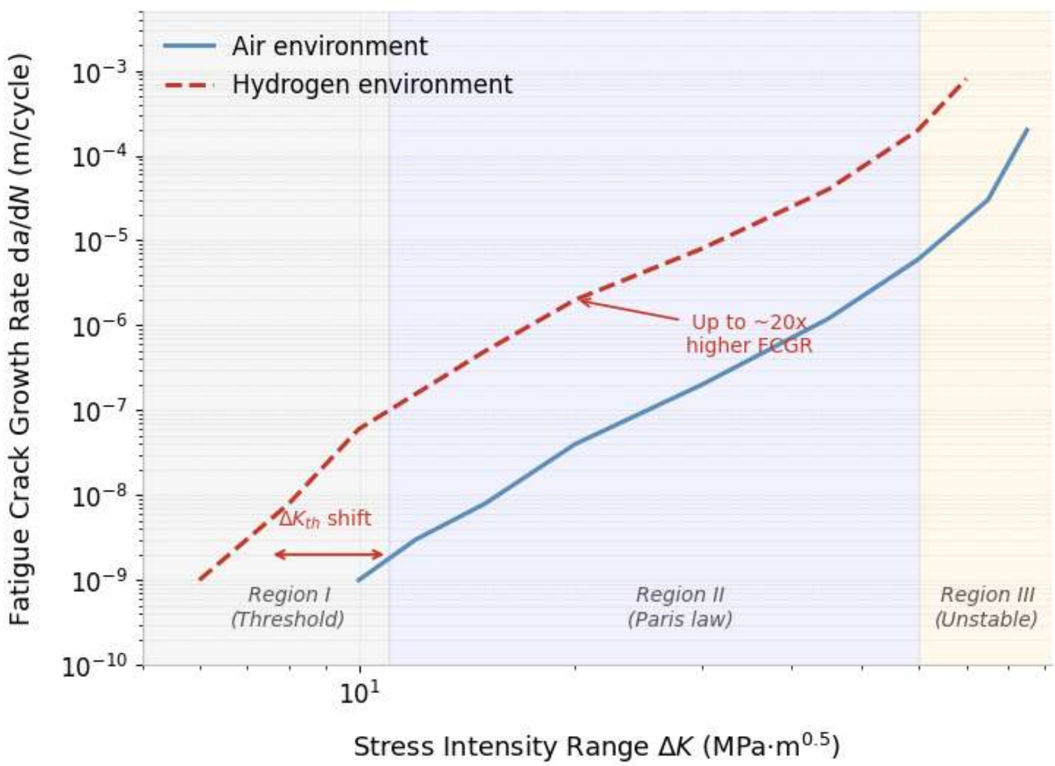

Figure 2-7 Schematic fatigue crack growth rate (da/dN) versus stress intensity range (ΔK) for pipeline steel in air and in a hydrogen environment, illustrating the reduction in threshold ΔK and the elevation of crack growth rates across all three propagation regions [35], [46].

Loading frequency is a further variable of practical concern. Below a critical frequency, the crack growth rate plateaus as hydrogen supply becomes the rate-limiting step rather than the mechanical driving force. At very low frequencies, comparable to the pressure fluctuations in actual pipeline operation, hydrogen has sufficient time to fully saturate the plastic zone ahead of the crack tip, producing worst-case crack growth behavior. Fatigue life reductions in hydrogen-blend service can be severe: Walallawita *et al.,* 2024 [25] reported that X80 pipeline steel exhibited a reduction in fatigue life from approximately 24,400 cycles in nitrogen to only 2,130 cycles at a 5 vol% hydrogen blend at 12 MPa, a 91% reduction driven by the combined effect of elevated pressure and cyclic loading. Even at lower blend fractions, [43] found that only 3% hydrogen in a blended gas stream could cause a 67.7% reduction in fatigue life compared to nitrogen, underscoring the outsized influence of even modest hydrogen additions under cyclic loading conditions.

Together, these three domains establish that the onset and severity of hydrogen embrittlement in service cannot be attributed to any single variable. Rather, it emerges from the simultaneous overlap of a sufficiently high hydrogen fugacity, a material microstructure with adequate trap density, and a stress state that drives hydrogen accumulation to a critical threshold. Quantifying these conditions in a fitness-for-service context requires fracture mechanics tools capable of incorporating hydrogen-modified material parameters, which are reviewed in Section 2.4.

2.4 Hydrogen Embrittlement Mechanisms

The degradation of pipeline steel mechanical properties in hydrogen service results from a sequence of physical and chemical processes: hydrogen molecules must dissociate and enter the steel lattice at the surface, diffuse through the microstructure to sites of stress concentration, interact with microstructural traps, and ultimately trigger one or more atomic-scale damage mechanisms. Understanding this causal chain is essential for interpreting experimental data and for developing physically grounded models for pipeline integrity assessment under hydrogen-blend service conditions.

2.4.1 Hydrogen Entry, Permeation, and Transport

Hydrogen entry into pipeline steel from a gaseous environment proceeds through a well-established sequence of surface and sub-surface reactions. H_2 molecules first physisorb onto the structurally defective sites of steel surface, then dissociate into atomic hydrogen through chemisorption, followed by absorption into sub-surface interstitial lattice sites and subsequent diffusion through the bulk material [45]. The subsurface hydrogen concentration driving this uptake follows Sievert's law, scaling with the square root of the hydrogen partial pressure, so that increasing the hydrogen fraction in a blended gas raises the lattice hydrogen concentration nonlinearly [24]. Once absorbed, hydrogen occupies the interstitial tetrahedral and octahedral sites of the body-centred cubic (BCC) iron lattice. The diffusivity of hydrogen in ferritic pipeline steels is several orders of magnitude higher than in austenitic face-centered cubic steels, making ferritic grades particularly susceptible to rapid hydrogen redistribution under applied stress.

Hydrogen transport through the bulk is characterized by an effective diffusion coefficient (Deff) that is substantially lower than the intrinsic lattice diffusion coefficient (DL), because microstructural trap sites retard hydrogen mobility. Oriani, 1970 [48] formalized this relationship, later adopted by [45], as:

$$\text{Deff} = \frac{DL}{(1+\frac{NT}{NL})} \qquad \text{2-3}$$

where NT is the trap site density and NL is the lattice site density. In higher-strength pipeline grades with greater trap densities, Deff is markedly reduced relative to lower-grade steels. This, however, does not reduce the risk of embrittlement because more hydrogen is retained at microstructurally damaging locations, such as grain boundaries and dislocation cores [49]. The overall physical process of hydrogen entry and transport in pipeline steel is illustrated in Figure 2.8.

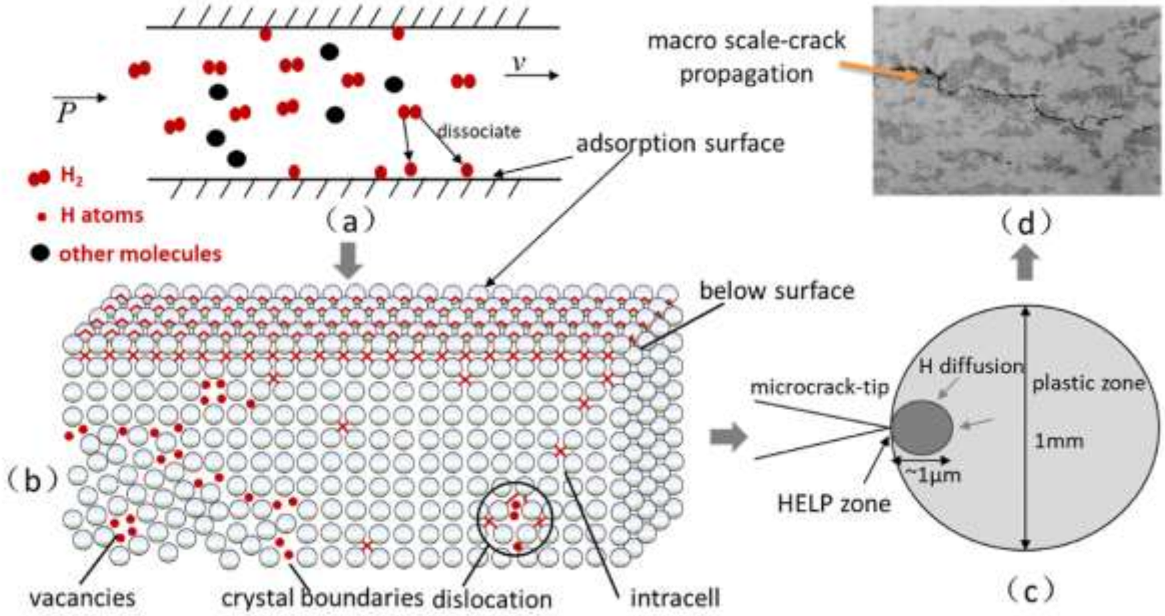

Figure 2-8 Physical process of hydrogen entry and embrittlement in pipeline steel, showing (a) H2 dissociation and surface adsorption, (b) H atom interaction with the metal lattice, (c) microcrack initiation and propagation, and (d) macroscopic crack development. Reproduced from [24].

2.4.2 Trap Sites and Microstructural Effects

Not all hydrogen within the steel lattice is equally mobile or equally damaging. Microstructural features with binding energies above the thermal energy available to diffusing hydrogen atoms act as trap sites, sequestering hydrogen from the lattice and governing its local distribution. Traps are broadly classified as reversible or irreversible based on binding energy. Reversible traps, including grain boundaries, low-angle boundaries, elastic stress fields around precipitates, and dislocation strain fields, retain hydrogen with relatively low binding energies and release it under modest applied energy at ambient temperature. Irreversible traps, such as incoherent carbides (TiC, NbC), non-metallic inclusions, and voids, bind hydrogen with sufficiently high activation energy to prevent re-release under normal service conditions [23], [24].

This distinction carries direct engineering significance. Reversible traps act as mobile hydrogen reservoirs: hydrogen stored at dislocations is transported with them during plastic deformation, delivering hydrogen to sites of stress concentration such as crack tips [49]. Irreversible traps can act as permanent sinks that reduce the concentration of diffusible hydrogen available to participate in damage processes, although at high hydrogen fugacities these traps saturate and cease to provide protection [24]. The diversity of trap sites across multiple length scales in structural steel is illustrated in Figure 2.9 [23], [50]. [49] demonstrated experimentally that dislocations accumulate at grain boundaries during plastic deformation, establishing these interfaces as primary sites for hydrogen concentration under applied stress. In higher-strength grades such as X70, X80, and X100, the elevated dislocation density and the presence of bainite and martensite-austenite constituents substantially increase total trap density, raising local hydrogen concentrations at critical microstructural sites under stress [23].

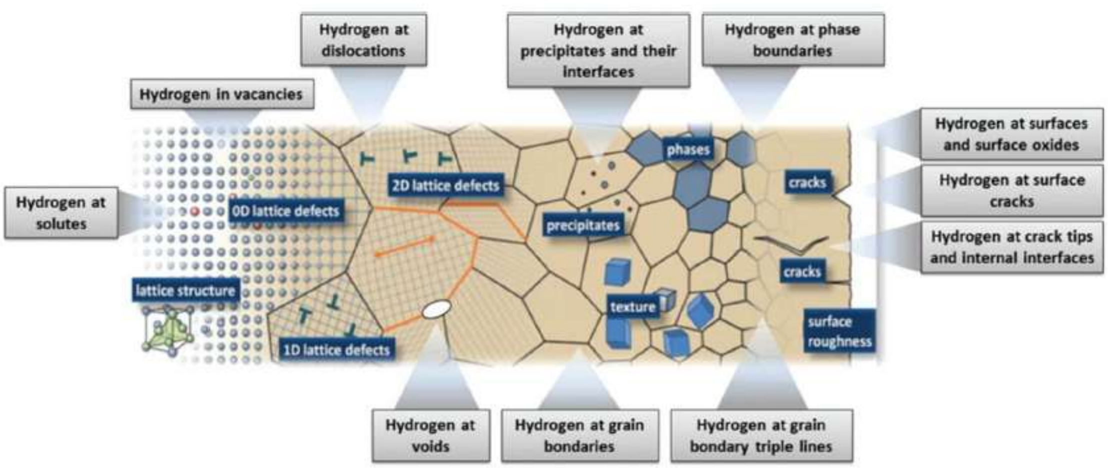

Figure 2-9 Hydrogen trapping sites across multiple length scales in structural steels, including lattice defects (vacancies, dislocations), grain boundaries, triple lines, precipitates and their interfaces, phase boundaries, and crack tips [50].

2.4.3 Hydrogen-Enhanced Decohesion (HEDE)

The hydrogen-enhanced decohesion (HEDE) mechanism proposes that dissolved hydrogen accumulated at a crack tip or grain boundary reduces the maximum cohesive force per unit area of which the iron lattice is capable, thereby lowering the stress required to separate atomic planes without prior gross plastic deformation [49]. The physical basis is that hydrogen atoms adsorbed at or diffused to a prospective fracture plane alter the electronic charge density between adjacent iron atoms, weakening the interatomic bonds. Because hydrogen is attracted to the region of maximum hydrostatic stress ahead of a crack tip by diffusion down a chemical potential gradient, localized hydrogen concentrations at that critical location can far exceed the bulk lattice concentration, providing the driving force for decohesion [23].

HEDE is most clearly operative at grain boundaries and phase interfaces, where it produces fracture surfaces characterized by quasi-cleavage or featureless intergranular morphology with relatively little macroscopic plastic deformation [49]. The mechanism is supported by first-principles density functional theory (DFT) calculations showing that hydrogen coverage reduces the work of fracture of iron grain boundaries, and by the fractographic observation that hydrogen-embrittled fracture surfaces in pipeline steels exhibit intergranular and quasi-cleavage features that are absent in specimens tested in inert environments [22], [23]. A practical implication for pipeline service is that HEDE tends to become the dominant operative mechanism at higher hydrogen concentrations, where the critical hydrogen accumulation ahead of grain boundaries or along slip band intersections is reached more rapidly [23]. The HEDE mechanism is illustrated schematically in Figure 2.10.

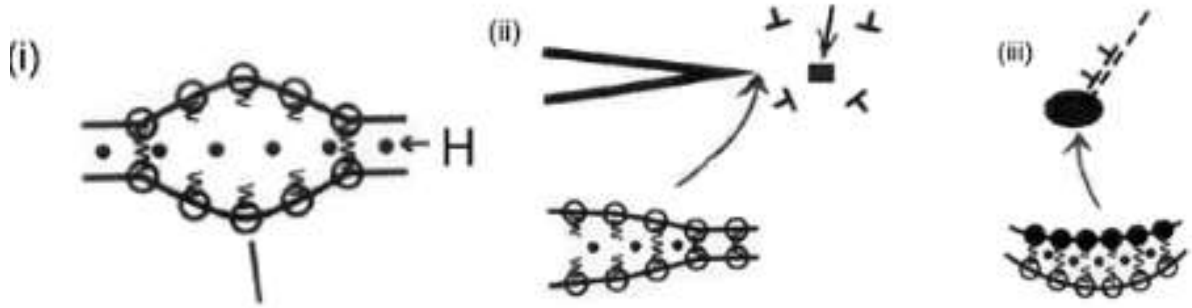

Figure 2-10 Schematic of the HEDE mechanism: (i) hydrogen atoms accumulate at a grain boundary or interface, reducing interatomic cohesive forces; (ii) weakened atomic bonds separate under applied tensile stress; (iii) decohesion at particle or phase interfaces [51].

2.4.4 Hydrogen-Enhanced Local Plasticity (HELP)

The hydrogen-enhanced localized plasticity (HELP) mechanism theorizes that dissolved hydrogen does not suppress dislocation motion but rather actively promotes it, thereby reducing the stress required for dislocation glide and increasing dislocation velocity in the vicinity of stress concentrations [49], [52]. The physical basis was established through in situ transmission electron microscopy (TEM) experiments conducted in a gaseous hydrogen environment, in which the introduction of hydrogen gas was observed to accelerate dislocation motion and activate dislocation sources in iron and other metals, with the effect reversing immediately upon removal of the gas [49]. The operative mechanism is hydrogen shielding: hydrogen atoms segregated to the stress fields of dislocations reduce the elastic interaction energy between neighboring dislocations and between dislocations and other obstacles, lowering the effective barrier to slip. A natural consequence is that cross-slip is suppressed, as redistributing the hydrogen atmosphere required for shielding is energetically unfavorable, confining dislocation motion to primary slip planes and producing the highly localized, planar slip bands characteristic of hydrogen-embrittled microstructures [49].

At the macroscopic level, HELP manifests paradoxically: although hydrogen enhances local plasticity at the nanoscale, the confinement of deformation to narrow slip bands produces macroscopic brittleness by concentrating damage rather than distributing it. Fracture surfaces produced under HELP-dominated conditions exhibit quasi-cleavage features and localized micro-void coalescence, reflecting the intense but spatially restricted plastic deformation preceding failure [22], [23]. HELP is most active at moderate hydrogen concentrations and in microstructures with high dislocation mobility, such as the acicular ferrite and bainite of X70 and X80 grades. It is now widely accepted that HELP and HEDE do not operate in isolation but interact synergistically: HELP-driven dislocation activity transports hydrogen to grain boundaries and interfaces, where accumulated hydrogen then drives HEDE-type decohesion, a sequence formalized as the HELP-mediated HEDE model by [23]. The HELP mechanism is illustrated schematically in Figure 2.11.

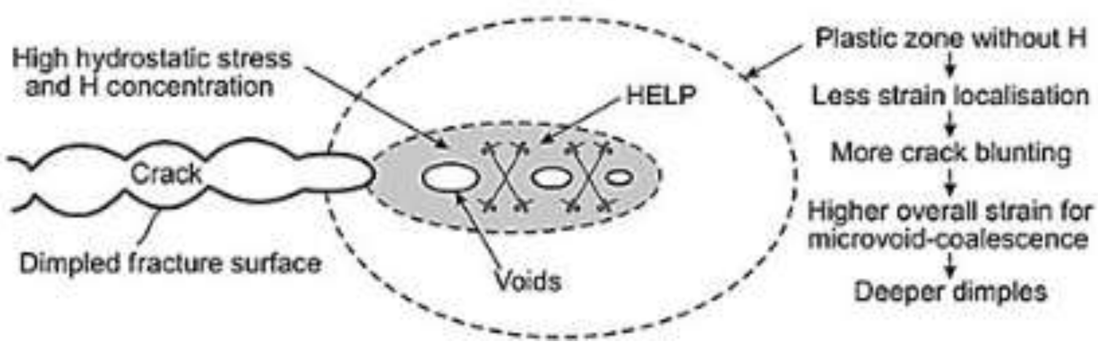

Figure 2-11 Schematic of the hydrogen-enhanced localized plasticity (HELP) mechanism: hydrogen concentrates in the high hydrostatic stress region ahead of the crack tip, promoting localized dislocation activity, void nucleation, and dimpled fracture surface morphology. In the absence of hydrogen, deformation is more distributed, producing greater crack blunting and deeper dimples [51].

2.4.5 Adsorption-Induced Dislocation Emission (AIDE)

The adsorption-induced dislocation emission (AIDE) mechanism, proposed by [22], attributes hydrogen embrittlement to the effect of chemisorbed hydrogen at the crack tip surface rather than to hydrogen dissolved within the bulk lattice. In this model, hydrogen adsorption weakens interatomic bonds at the crack tip and lowers the energy barrier for dislocation nucleation from the crack tip itself. The result is enhanced emission of dislocations into the material on slip planes inclined to the crack front, facilitating crack advance by a combination of localized plasticity and void formation just ahead of the crack tip, rather than by lattice decohesion or remote plasticity [22].

A distinguishing feature of AIDE is that it requires hydrogen only at the crack surface and is therefore less dependent on bulk hydrogen diffusivity than HEDE or HELP. This makes it potentially significant under conditions of rapid loading or where bulk diffusion is rate-limiting, such as in high-frequency fatigue loading. AIDE predicts fracture surface morphologies that closely resemble those of liquid-metal embrittlement: shallow dimples and quasi-cleavage features with evidence of dislocation activity at the crack tip, which [22] used to argue that the mechanism is operative across a wide range of embrittling environments. For pipeline steels under hydrogen-blend service conditions, AIDE is considered a secondary contributor relative to HELP and HEDE, though its role may be more pronounced at crack initiation sites such as surface defects, weld toes, and corrosion pits where surface hydrogen concentrations are highest [22], [23].

2.5 Mechanical Property Degradation in Hydrogen

The embrittlement mechanisms reviewed in Section 2.4 manifest at the component level as three inter-related but experimentally distinct forms of mechanical degradation: a reduction in ductility under monotonic tensile loading, a reduction in FT under quasi-static crack opening, and an acceleration of fatigue crack growth under cyclic loading. Each of these has direct implications for pipeline integrity assessment, as they alter the material parameters used in design codes and fitness-for-service calculations. This section reviews the experimental evidence for each mode of degradation across the API 5L grade range relevant to hydrogen-blend service.

2.5.1 Ductility Loss

The most consistently reported effect of hydrogen on pipeline steel is a reduction in ductility under tensile loading, while yield strength and ultimate tensile strength are largely unaffected. This dissociation between strength retention and ductility loss is one of the defining characteristics of hydrogen embrittlement in ferritic steels and has been confirmed across the API 5L grade range from X42 through X100 [27], [45]. Ductility is typically quantified by two complementary measures: elongation to fracture (EL), measured from the load-displacement record, and reduction in area (RA), measured post-mortem on the fractured specimen. Shang *et al.,* 2024 [53] conducted tensile tests on X52 steel in air and in hydrogen gas across five orders of magnitude of strain rate and confirmed that elastic modulus, yield strength, and ultimate tensile strength showed no measurable dependence on either environment or strain rate, while ductility was substantially reduced in hydrogen at all rates, with the reduction becoming more severe at lower strain rates. The study also noted that RA consistently provides a less conservative measure of ductility loss than EL, a methodological distinction with direct consequences for how the hydrogen embrittlement index is calculated and compared across studies.

The strain rate dependence of ductility loss is mechanistically consistent with hydrogen diffusion kinetics: at lower strain rates, more time is available for hydrogen to diffuse to regions of peak stress triaxiality ahead of developing necks and cracks, increasing local hydrogen concentration and the severity of HEDE and HELP-mediated damage [46]. This provides the physical basis for slow strain rate tensile (SSRT) testing as the standard laboratory method for conservative assessment of hydrogen embrittlement susceptibility. In practice, ductility losses in pipeline steels under hydrogen-blend conditions can be substantial even at low hydrogen fractions. Stalheim *et al.,* 2010 [29] recorded HEI values of 11.6% and 14.6% for X60 base and weld metal at only 20% hydrogen blending at 2.07 MPa, rising to 12.4% and 18.0% at 100% hydrogen. At higher grades, Nanninga *et al.,* 2012 [27] reported elongation losses of approximately 22%, 28%, and 50% for X52, X65, and X100 respectively at 13.8 MPa pure hydrogen, demonstrating a clear positive correlation between strength level and ductility loss severity. Fractographic analysis consistently reveals a corresponding transition in fracture morphology from the cup-and-cone ductile fracture with dimple features observed in air to a mixed mode of quasi-cleavage and micro-void coalescence in hydrogen environments, with secondary cracking becoming more prevalent as hydrogen concentration and pressure increase [27], [29].

2.5.2 Fracture Toughness Reduction

Fracture toughness, expressed as KIC, JIC, or the J-resistance curve (J-R), quantifies a material's resistance to crack extension under quasi-static loading and is a primary input to fracture mechanics-based fitness-for-service assessments such as those prescribed by ASME B31.12 for hydrogen pipelines. Hydrogen degrades FT through the same HEDE- and HELP-mediated mechanisms that govern ductility loss, with hydrogen accumulation at the crack tip reducing cohesive energy and confining plastic deformation to a narrow process zone, thereby reducing the energy consumed in crack propagation [23], [49]. As reported in Section 2.3.1, FT reductions of 18 to 45% relative to air have been measured across API 5L grades at 6.9 MPa hydrogen [45], and the magnitude of degradation increases non-linearly with hydrogen pressure. Wei, 2025 [54] characterized FT degradation of X80 pipeline steel at hydrogen pressures from 0 to 12 MPa and found that toughness decreased progressively in a logarithmic or power-law trend with rising pressure, while fracture mode shifted from ductile dimple-dominated failure to quasi-cleavage as pressure increased. Notably, the steepest toughness decline occurred at low to moderate pressures, with the rate of reduction diminishing above approximately 8 MPa, suggesting an approach to a saturation condition at higher pressures.

The relationship between microstructure and FT degradation in hydrogen is not straightforward. While higher-strength grades generally exhibit lower absolute toughness in both air and hydrogen, the relative degradation in toughness across grades is more complex. Ronevich *et al.,* 2025 [55] found that despite large differences in yield strength and microstructure spanning ferrite-pearlite, acicular ferrite, bainite, and martensite across grades X52 through X120, fracture resistance in gaseous hydrogen remained within a factor of two to three across the grade range, with elastic-plastic fracture behavior maintained in all cases. Higher-strength steels showed lower fracture resistance and lower tearing modulus in hydrogen, consistent with the general air-environment trends, but the grade dependence was less severe than for monotonic ductility loss. Weld regions and heat-affected zones consistently exhibit lower FT in hydrogen than adjacent base metal, a consequence of microstructural heterogeneity, elevated dislocation density, and residual tensile stress [45]. These findings collectively indicate that FT reductions in hydrogen service must be accounted for explicitly in defect assessment calculations, and that use of air-environment toughness values without correction is non-conservative for any pipeline steel grade operated in hydrogen or hydrogen-blend service.

2.5.3 Fatigue Crack Growth Acceleration

Hydrogen-assisted fatigue crack growth (HA-FCG) represents the most practically significant form of mechanical property degradation for pressurized pipeline systems, as pipelines are subject to continuous cyclic pressure fluctuations throughout their service life. The presence of hydrogen accelerates fatigue crack growth rates (FCGR) across all three Paris Law regions: it reduces the threshold stress intensity range ΔKth below which cracks do not propagate (Region I), elevates crack growth rates per cycle da/dN at intermediate stress intensity ranges (Region II), and reduces the critical stress intensity at which unstable fast fracture occurs (Region III) [45], [46]. For X42 pipeline steel at 6.9 MPa hydrogen, FCGR near the threshold were up to 150 times those in nitrogen at the same stress intensity range [41], a level of acceleration that carries direct consequences for the inspection intervals and maximum allowable operating pressures of legacy pipelines considered for hydrogen-blend service.

An important finding from recent comprehensive testing programs is that FCGR in gaseous hydrogen is broadly consistent across pipeline steel grades despite large differences in strength and microstructure. Ronevich *et al.,* 2025 [55] tested steels spanning X52 to X120 with microstructures ranging from ferrite-pearlite to martensite and found that FCGR in high-pressure hydrogen gas (210 bar) fell within a factor of two to three for all grades, with steels containing higher fractions of pearlite, typical of older vintage lines, showing modestly lower crack growth rates. This grade consistency underpins the single-material fatigue design curves recently codified in ASME B31 Code Case 220 for piping and pipelines in hydrogen service, which capture the observed dependence of FCGR on stress ratio and hydrogen partial pressure through a semi-empirical correction factor. Crucially, it is hydrogen partial pressure rather than hydrogen volume fraction that governs FCGR: a 10% hydrogen blend in a 100-bar transmission pipeline carries a hydrogen partial pressure of 10 bar, which produces substantially greater crack growth acceleration than the same blend fraction in a 1 bar distribution network [55].

Within a given pipeline, weld regions and the heat-affected zone (HAZ) exhibit the highest FCGR in hydrogen environments. Tang *et al.,* 2025 [56] examined the FCGR of X80 welded joints under 12 MPa with 0, 10, and 30 vol% hydrogen, finding that the HAZ displayed the highest crack growth rates owing to its bainitic microstructure and the presence of hard, brittle martensite-austenite

(M-A) constituents, while weld metal with a fine acicular ferrite microstructure showed superior hydrogen embrittlement resistance relative to both base metal and HAZ. The FCGR curves exhibited non-linear behavior in log-log coordinates, comprising a transition regime followed by a distinct acceleration regime as hydrogen content increased. Gas stream impurities further modify FCGR: Shang *et al.,* 2023 [57] demonstrated that CO_2 content in a hydrogen-enriched natural gas stream progressively accelerated the FCGR of X80 above that measured in pure hydrogen, attributed to CO_2 adsorption on the iron surface promoting hydrogen migration from surface to subsurface lattice sites. These findings establish that fatigue life in hydrogen-blend service cannot be predicted reliably from air-environment crack growth data alone, and that fitness-for-service assessments must account for the combined influence of hydrogen partial pressure, loading frequency, weld microstructure, and gas stream composition on effective FCGR.

2.6 Fracture Mechanics-Based Integrity Assessment

The mechanical property degradation reviewed in Section 2.5 acquires practical engineering significance through its role as an input to fracture mechanics-based integrity assessment. Pipelines inevitably contain pre-existing flaws introduced during manufacture, welding, or service, and the central question for hydrogen-blend repurposing is whether those flaws will remain stable, grow sub critically to a critical size, or propagate to failure within a defined service interval under degraded-property conditions. Fracture mechanics provides the quantitative framework for answering this question, through a combination of stress intensity factor solutions for crack geometries, material resistance parameters measured in hydrogen gas, fitness-for-service (FFS) assessment procedures, and design codes that encode permissible operating conditions. This section reviews each component of that framework with emphasis on developments relevant to hydrogen pipeline service.

2.6.1 Fracture Mechanics Parameters for Hydrogen Service

The fracture mechanics of hydrogen-exposed pipeline steels is characterized by three distinct categories of material resistance parameter, each governing a different failure mode. For fracture under quasi-static loading, the relevant parameters are the hydrogen-assisted FT, KIH, which replaces the air-environment value KIC as the resistance to unstable crack extension; the J-integral at crack initiation, JIC, when elastic-plastic conditions prevail; and the J-resistance curve (J-R), which quantifies stable crack extension capacity. For sustained-load subcritical crack growth, the threshold stress intensity factor KTH defines the lowest applied stress intensity below which a pre-existing crack will not propagate under constant displacement or constant load in a hydrogen environment; values of KTH are typically substantially lower than KIC, with reductions of 30 to 60 percent reported for pipeline-grade ferritic steels in high-pressure hydrogen gas [45]. For cyclic loading, the fatigue crack growth rate relationship da/dN as a function of the applied stress intensity range ΔK, measured in hydrogen gas, captures the three-regime behaviour reviewed in Section 2.5.3. Each of these parameters must be determined experimentally in the relevant hydrogen environment because empirical correlations from air-environment values are insufficiently reliable for use in design-level assessments [5], [42].

A practical complication in measuring these parameters for pipeline-service materials is that the specimen size requirements of standard fracture mechanics testing protocols are difficult to satisfy using coupons extracted from pipe walls. Kappes and Perez, 2023b [5] noted that wedge-opening-loaded (WOL) constant-displacement specimens conforming to ASTM E1681, as referenced by ASME B31.12 for KTH measurement, cannot in most cases be machined from the wall thicknesses typical of existing gas transmission pipelines, requiring modified specimen geometries and alternative stress intensity calibration equations. This testing constraint means that the material-specific hydrogen fracture resistance data needed for high-fidelity FFS assessment is often unavailable for the actual pipe steel under evaluation, and design must instead rely on conservative bounding values or data from comparable grades. The resolution of this gap represents an ongoing practical challenge for operators pursuing performance-based qualification under ASME B31.12 Option B [5].

2.6.2 ASME B31.12 Design Code Framework

The primary design code governing hydrogen transmission pipelines in North America is ASME B31.12, Hydrogen Piping and Pipelines, which provides two qualification routes for pipeline materials. Option A is a prescriptive route that limits material yield strength to a maximum of 483 MPa (approximately grade X60) and imposes reduced design factors through a material performance factor Hf, which is tabulated as a function of hydrogen partial pressure and specified minimum yield strength with values ranging from 0.542 to 1.0. The Hf factor is applied multiplicatively to reduce the allowable hoop stress relative to the ASME B31.8 natural gas pipeline standard, effectively building conservative hydrogen-embrittlement margins into the wall thickness or pressure rating without requiring explicit fracture mechanics analysis (ASME B31.12, 2019). When the design hoop stress exceeds 40% of the specified minimum yield strength, ASME B31.12 additionally requires a fracture control and arrest criterion to be satisfied, drawing on the hydrogen-assisted crack growth curves standardized in ASME B31 Code Case 220 for this purpose [55]. Option B is a performance-based route that removes the yield strength ceiling (up to 550 MPa, approximately X80) in exchange for explicit fracture mechanics qualification, including measurement of FT and fatigue crack growth rates in gaseous hydrogen, and design life calculations using those data against an initial assumed flaw consistent with the resolution limits of the applied non-destructive examination method. Option B references the API 579-1/ASME FFS-1 Fitness-for-Service standard for the fracture mechanics evaluation procedures [13].

Oesterlin *et al.,* 2025 [13] compared the lifetime predictions of ASME B31.12 against the German technical rule DVGW G 464 (2023), which adopts a conceptually similar fracture mechanics-based design approach but differs in assumed crack geometry (axially oriented semi-elliptical surface crack in a cylinder for B31.12 versus a semi-elliptical surface flaw in a flat plate for G 464) and in the reference stress solutions used for the Failure Assessment Diagram calculation. Applying both codes to a use-case study with material-specific hydrogen-assisted fatigue crack growth data, Oesterlin *et al.,* 2025 [13] found that both codes produced relatively similar lifetime estimates for typical operating scenarios, with ASME B31.12 generally predicting somewhat more allowable pressure cycles than DVGW G 464 due primarily to differences in the assumed initial crack aspect ratio rather than fundamental differences in the fracture mechanics treatment. The authors identified initial crack size detection capability as the single most influential parameter for extending predicted service life, ahead of material-specific crack growth rates, underscoring the importance of high-resolution inline inspection in any fracture mechanics-based requalification program.

2.6.3 Fitness-for-Service and the Failure Assessment Diagram

For pipelines already in service that contain detected or assumed flaws, the fitness-for-service assessment determines whether those flaws are acceptable for continued operation. The internationally recognized procedure for crack-like flaw assessment is the Failure Assessment Diagram (FAD), which forms the basis of both BS 7910:2019 and API 579-1/ASME FFS-1. In the FAD framework, a component with a given flaw geometry and loading condition is characterized by two normalized parameters: the fracture ratio Kr, defined as the ratio of the applied stress intensity factor KI to the material fracture toughness Kmat; and the load ratio Lr, defined as the ratio of the applied reference stress to the material flow stress. The FAD envelope, a failure assessment line (FAL), bounds the safe region in Kr-Lr space and reflects the interaction between brittle fracture and plastic collapse failure modes. An assessment point (Kr, Lr) that falls inside the FAL is considered acceptable; one that falls on or outside it represents predicted failure. Three levels of assessment are available in both standards, with increasing accuracy and decreasing conservatism as material-specific stress-strain data are incorporated [5].

The transition from natural gas to hydrogen service shifts assessment points toward the failure envelope through two simultaneous effects: hydrogen increases the applied stress intensity factor indirectly by enabling subcritical crack growth between inspection intervals, while simultaneously reducing Kmat from KIC to the lower hydrogen-assisted value KIH. Kappes and Perez 2023b [5] illustrated this using a FAD constructed for API 579-1/ASME FFS-1, showing that if hydrogen reduces FT by approximately 50% (a value consistent with the reductions reviewed in Section 2.5.2), the Kr coordinate of each assessment point doubles at constant operating pressure, moving flaws that were safely inside the FAL in natural gas service to a position on or outside the failure envelope in hydrogen service. The implication is that some flaw sizes that are currently tolerated under natural gas fitness-for-service assessments become unacceptable without remediation when the same pipeline is repurposed for hydrogen transport, even at unchanged operating pressure.

A limitation of conventional FAD assessments as applied to hydrogen pipelines is that they treat the material as homogeneous, which is not representative of welded regions where the HAZ and weld metal have markedly different strength, toughness, and hydrogen sensitivity compared to base metal. Wijnen *et al.,* 2025 [8] addressed this by developing virtual FADs using a coupled thermo-metallurgical welding simulation combined with diffusion-elastic-plastic phase-field fracture modelling for an X60 girth-welded pipeline. Their computationally generated FADs were in good agreement with the standard BS 7910 / API 579 approaches for homogeneous base metal, but showed that the standard FAD is non-conservative when the crack tip is located within or adjacent to the hard, brittle regions of the HAZ where hydrogen preferentially accumulates and where local fracture resistance is substantially below the base metal value used in homogeneous assessments. The authors proposed mechanistically derived FAD safety factors that account explicitly for the role of residual stresses from welding and for the presence of hard microstructural regions, representing a significant advancement toward more physically representative FFS assessments of welded hydrogen pipelines.

2.6.4 Safe-Life Prediction and Critical Crack Size

Safe-life prediction for hydrogen pipelines requires integration of the fatigue crack growth relationship from an initial flaw size, representative of the detection threshold of the applied inspection method, to a critical crack depth at which the FAD assessment predicts failure at the design operating pressure. ASME B31.12 defines the critical crack depth conservatively as acrit = 0.8t, where t is the pipe wall thickness, as this represents the upper bound of the API 579-1/ASME FFS-1 stress intensity solutions for semi-elliptical surface cracks in a cylinder. The number of allowable pressure cycles N over the design life is then calculated by integrating the hydrogen-assisted da/dN-ΔK relationship from the assumed initial crack depth to acrit, with the crack driving force ΔK expressed as a function of the pressure-induced hoop stress and the evolving crack geometry. The result is highly sensitive to the assumed initial crack depth, the hydrogen partial pressure (which governs the elevation of the FCGR curve relative to the air baseline), the loading frequency, and the stress ratio R = Kmin/Kmax, all of which must be incorporated in a manner consistent with the hydrogen-assisted crack growth data used for calibration [5], [13].

While deterministic safe-life calculations provide a conservative design basis, probabilistic fracture mechanics methods allow the conservatism inherent in code-prescribed assumptions to be quantified and, where appropriate, reduced. Hasanli, 2025 [9] applied an integrated FAD and Monte Carlo simulation framework to evaluate the conservatism of ASME B31.12 Option A, using a semi-elliptical flaw of depth 0.25t and length 1.5t as the assumed reference defect and sampling wall thickness and yield strength from statistical distributions while holding FT fixed at 69.3 MPa√m. Across three design scenarios spanning safety factor products from 0.388 to 0.720 at temperatures of 0 and 20°C, the study found that flaw acceptability was maintained in all deterministic cases and that the computed probability of failure remained below 10^{-6} for all scenarios, with no failures predicted when the safety factor product fell below 0.637. These results confirm that Option A embeds substantial conservatism relative to a reliability-based criterion and support the use of reliability methods to rationalize operating constraints when pursuing performance-based qualification of existing pipelines for hydrogen service.

2.6.5 Integrity Challenges for Repurposed and Vintage Pipelines

The integrity challenges associated with repurposing existing natural gas infrastructure for hydrogen service are particularly acute for vintage pipelines, which represent the majority of installed capacity in many transmission networks. Vintage pipelines were typically manufactured using electric resistance welding (ERW) or submerged arc welding (SAW) processes that predate the Charpy impact testing requirements of modern API 5L specifications, and their base metal and weld toughness in hydrogen environments is often unknown and may be substantially lower than that of modern controlled-rolled steels. ASME B31.12 Option A was specifically designed to accommodate such cases by providing conservative design margins without requiring explicit fracture mechanics characterization, and its applicability is broadly limited to steels with yield strengths at or below 483 MPa, a restriction that effectively excludes grade X70 and above from the prescriptive route [5], [58].

A further complication in assessing blend pipelines is the absence of any demonstrated safe lower threshold for hydrogen partial pressure below which material degradation does not occur. Kappes and Perez 2023b [5] reviewed the available literature and concluded that no lower bound of hydrogen partial pressure has been identified for transmission-pressure pipelines at which mechanical property degradation is absent, meaning that even modest blending fractions of 5 to 10 vol% at operating pressures of 70 to 100 bar can produce hydrogen partial pressures sufficient to influence FT and fatigue crack growth rates. This finding has significant implications for the fitness-for-service assessment of pipelines currently designed and inspected to natural gas standards, as flaw acceptance criteria developed for non-hydrogenated service may be systematically non-conservative once any hydrogen is introduced to the gas stream. The combination of degraded FT, accelerated fatigue crack growth, and the potential non-conservatism of standard homogeneous FAD approaches in welded regions collectively define the principal integrity challenges that must be addressed through material testing, high-resolution inspection, and code development as the hydrogen economy scales up through repurposed existing infrastructure [5], [8], [13].

2.7 Experimental Methods for Hydrogen Embrittlement Evaluation

Characterizing the susceptibility of pipeline steels to hydrogen embrittlement requires a suite of experimental methods capable of reproducing the conditions encountered in high-pressure gaseous hydrogen service and translating material responses into parameters usable in design codes and fitness-for-service assessments. The principal methods employed in the literature and referenced by relevant standards, including ASME B31.12 and the supporting ASTM test protocols, fall into three categories: tensile and slow-strain-rate testing for ductility-based embrittlement indices; fracture mechanics testing for toughness and sustained-load crack-growth thresholds; and fatigue crack-growth testing for cyclic-loading resistance. Supplementary microstructural and fractographic characterization is routinely combined with mechanical testing to interpret failure mechanisms. The choice of hydrogen charging method, whether high-pressure gaseous exposure or electrochemical pre-charging, is a critical experimental variable that governs the fidelity of the simulated environment and the relevance of the resulting data to field conditions [5], [59].

Tensile testing in hydrogen environments is the most widely applied first-pass assessment of hydrogen embrittlement susceptibility. The hydrogen embrittlement index (HEI) is commonly calculated from the loss in elongation to fracture or reduction in area between specimens tested in air and specimens tested in or pre-charged with hydrogen. A threshold value of HEI = 10% is commonly used in the literature as a reference for meaningful susceptibility, with values exceeding this level considered warranting further evaluation of structural integrity. Slow strain rate testing (SSRT), standardized in ASTM G129, uses deliberately low crosshead displacement rates, typically in the range of 10^{-6} to 10^{-4} s^{-1}, to allow sufficient time for hydrogen to diffuse to regions of peak stress triaxiality as damage develops, thereby maximizing the measured embrittlement severity [60], [61].

Various authors have demonstrated on X52 steel that hydrogen-induced ductility loss was consistently more severe at lower strain rates while strength was unaffected across five orders of magnitude of rate, confirming the diffusion-kinetic basis of the SSRT approach. Both in-situ testing, in which the specimen is directly exposed to pressurized hydrogen gas during the test, and ex-situ testing of electrochemically pre-charged specimens are used in practice. In-situ gaseous testing under high-pressure autoclave conditions more faithfully replicates pipeline service but involves substantial infrastructure cost and safety requirements; electrochemical pre-charging is less expensive and more widely accessible but introduces higher near-surface hydrogen concentrations that do not always reflect the lower bulk concentrations typical of gaseous pipeline service [29], [59] demonstrated a hollow-specimen geometry as a practical alternative that enables in-situ testing at moderate pressures using a minimal gas volume, a configuration applicable to both base metal and welded joints.

Fracture mechanics testing provides the material resistance parameters needed for structural integrity assessment: the hydrogen-assisted fracture toughness KIH and J-integral at crack initiation JIC, measured using compact tension (CT) or single-edge notched bend (SENB) specimens following ASTM E1820; and the threshold stress intensity factor for sustained-load crack growth KTH, measured using wedge-opening-loaded (WOL) constant-displacement specimens following ASTM E1681. Testing is conducted with specimens directly exposed to high-pressure gaseous hydrogen in an autoclave vessel, which is the required configuration under ASME B31.12 Option B qualification. Loading rates must be sufficiently slow to allow hydrogen equilibration at the advancing crack tip; Paterlini *et al.,* 2025 [59] identify loading rate as one of the two most important test variables alongside hydrogen partial pressure, since rates that are too high underestimate the toughness reduction and produce non-conservative material data. Electrochemical pre-charging followed by testing in air is used in some studies as a lower-cost alternative, but hydrogen concentration profiles in pre-charged specimens decay during testing, making the results sensitive to the time elapsed between charging and testing and to specimen dimensions [45], [59]. A further practical constraint is that WOL specimens that meet the size requirements of ASTM E1681 typically cannot be extracted from the walls of existing transmission pipelines, necessitating modified geometries and recalibrated stress-intensity-factor solutions [4].

Fatigue crack growth testing in hydrogen is conducted using CT specimens cycled under controlled stress intensity range ΔK in a high-pressure gaseous hydrogen autoclave, following protocols adapted from ASTM E647 with modifications for the pressurized environment. The test produces da/dN–ΔK curves that capture the three-regime hydrogen-assisted fatigue crack growth (HA-FCG) behaviour reviewed in Section 2.5.3. Key test variables are hydrogen partial pressure, loading frequency, and stress ratio $R = K_{min}/K_{max}$, all of which independently influence the measured crack growth rates and must therefore be controlled and reported to allow inter-laboratory comparison [55], [59]. Frequency is particularly significant because lower frequencies increase the time per cycle available for hydrogen to diffuse to the crack tip, producing higher per-cycle crack advance; the design curves in ASME B31 Code Case 220 were developed from data at a reference frequency of 0.1 Hz and include a correction factor for frequency dependence [62]. Because fatigue crack growth rates in welded regions differ substantially from base metal behavior, with the HAZ typically exhibiting the highest rates owing to its bainitic microstructure and hard martensite-austenite constituents, specimens must be machined to locate the notch and starter crack in the specific region of interest [56].

Fractographic and microstructural characterization are integral to the interpretation of mechanical test results. Scanning electron microscopy (SEM) of fracture surfaces documents the transition from the ductile cup-and-cone morphology with equiaxed dimples characteristic of air-environment failure to the quasi-cleavage, intergranular, and mixed-mode features associated with hydrogen-assisted fracture, providing qualitative confirmation that the mechanical test was sensitive to the hydrogen environment [27], [29]. Hydrogen permeation testing using a Devanathan-Stachurski electrochemical cell, combined with Fick's law analysis, quantifies the effective diffusivity and subsurface hydrogen concentration, which are required inputs for calibrating the hydrogen content achieved in test specimens [59]. Electron backscatter diffraction (EBSD) mapping reveals grain-boundary character, dislocation-density distributions via kernel-average misorientation, and the fraction and spatial distribution of hard microstructural constituents, all of which modulate local hydrogen trapping and embrittlement susceptibility [45]. Thermal desorption spectroscopy (TDS) characterizes the binding energies and densities of hydrogen trap sites and can be used to verify the total and diffusible hydrogen content introduced during pre-charging. Taken together, these complementary techniques establish the connection between microstructure, hydrogen content, and observed mechanical response, which is essential for the microstructure-informed interpretation required by modern performance-based qualification routes.

2.8 Machine-learning Applications in Hydrogen Embrittlement Modeling

The resource-intensive nature of high-pressure hydrogen testing, combined with the complexity of the embrittlement mechanisms reviewed in the preceding sections, has motivated the application of machine-learning (ML) as a complement to experimental and physics-based approaches. ML models offer the ability to identify nonlinear relationships among steel composition, microstructure, test environment, and measured properties without requiring explicit mechanistic assumptions, and they can substantially reduce the number of costly experiments needed to characterize a new material or operating condition. Since approximately 2022, ML methods have been applied across several overlapping areas relevant to pipeline hydrogen service: prediction of tensile and ductility properties, FT estimation, fatigue crack growth rate modeling, physics-informed neural networks, atomistic simulation via machine-learning interatomic potentials, and operational leak detection. Table 2.3 provides a comparative summary; selected studies are discussed below.

Several research have produced relevant contributions. Ahmed *et al.,* 2024 [14] applied supervised ML algorithms to predict the necking area reduction (RA) of carbon steel in hydrogen environments, identifying hydrogen partial pressure and yield strength as the two dominant input variables and demonstrating applicability to pipeline integrity planning. Building on this, Gyaabeng *et al.,* 2025 [15] developed gradient boosting, random forest, KNN, and decision tree models to predict fracture toughness (KIH) for API 5L X52, X60, and X70 steels under pressurized hydrogen, finding that hydrogen pressure alone accounted for approximately 32% of toughness variance and that a saturation plateau exists above roughly 8 MPa. Carbon and phosphorus content were the most influential alloying variables, and oxygen concentrations below 200 ppm were associated with reduced embrittlement, consistent with competitive adsorption arguments. Iyiola *et al.,* 2025 [60] addressed the data scarcity problem that limits all hydrogen ML studies by constructing a stacked hybrid ensemble combining random forest, LightGBM, and a bagging regressor to predict elongation loss in low-carbon pipeline steels, achieving better generalization than any single-algorithm model.

Ahmed *et al.,* 2025 [61] introduced a cross-test transfer approach in which ML models originally trained on tensile test data were applied to fatigue crack growth (FCG) datasets to predict RA, exploiting the mechanistic coupling between static and cyclic hydrogen damage to circumvent the even smaller body of available FCG data. Kim *et al.,* 2022 [34] established the first ML framework for predicting the hydrogen environment embrittlement index of austenitic steels, with random forest consistently outperforming linear and Bayesian models and correlation analysis identifying Ni and Mo as dominant compositional features. Campari *et al.,* 2024 [65] developed ANN and random forest models for hydrogen-assisted fatigue crack growth rate in X52, X70, and X100 pipeline steels, with the ANN demonstrating the ability to interpolate accurately to hydrogen pressures outside the training distribution, a critical capability given the limited pressure coverage of available datasets.

At the physics-informed end of the spectrum, *Yu et al.,* 2025 [66] embedded stress-assisted hydrogen diffusion constraints into a transfer learning-augmented physics-informed neural network (PINN) for X65 steel, achieving R^2 values exceeding 0.8 across diverse loading conditions and outperforming both data-only neural networks and classical Paris law fitting. At the atomistic scale, Ito *et al.,* 2025 [67] developed a machine-learning interatomic potential (MLIP) for the Fe-H system that enabled large-scale molecular dynamics simulations revealing that hydrogen suppresses dislocation emission at general grain boundaries, providing the first quantitative atomistic support for the hydrogen-enhanced decohesion mechanism in ferritic steel.

Despite this progress, several limitations must be acknowledged. Available training datasets remain small and heterogeneous, cross-grade generalization is rarely demonstrated rigorously, and purely data-driven models risk learning spurious correlations that fail for vintage or non-standard steels precisely the grades most relevant to repurposing decisions. Physics-informed and MLIP approaches partially address the extrapolation problem but require well-validated governing equations and large DFT training sets respectively. The integration of atomistic MLIP insights with mesoscale and macroscale integrity frameworks remains an open research challenge.

Table 2-3 Summary of selected machine-learning studies in hydrogen embrittlement and pipeline integrity (2022-2025)

Application	Algorithm(s)	Material	Key Finding	Reference
Elongation loss prediction	Stacked hybrid ensemble (RF, LightGBM, Bagging)	Low-carbon pipeline steels	Improved accuracy over single-model baselines; addresses data scarcity in H2 testing	[60]
Fracture toughness (KIH) prediction	KNN, RF, Gradient Boosting, Decision Tree	API 5L X52, X60, X70	H2 pressure dominates (32% of variance); toughness plateaus above 8 MPa; C and P also influential	[15]
Fatigue failure in H2-transporting pipelines	Novel ML approach leveraging cross-test data	Carbon steel pipeline grades	FCG test data used to predict RA; cross-test transfer improves predictions under data scarcity	[65]
Necking area reduction (RA) prediction	Multiple supervised ML algorithms	Carbon steels	H2 pressure and yield strength most influential; model applicable to integrity planning	[14]
Embrittlement index (HEE) prediction	Random Forest, SVM, Bayesian Ridge, LR	Austenitic steels	RF most accurate; Ni and Mo identified as dominant compositional features via correlation analysis	[34]
H-assisted fatigue crack growth (da/dN)	ANN, Random Forest	API 5L X52, X70, X100	ANN outperformed RF; accurate interpolation to unseen H2 pressures outside training range	[65]
FCGR prediction via physics-informed NN	PINN + Transfer Learning (TPINN)	X65 pipeline steel	$R^2 > 0.8$; physical constraints improved extrapolation vs. data-only NN and Paris law fitting	[66]
Atomistic grain boundary embrittlement	ML Interatomic Potential (MLIP, Fe-H)	α-Iron	Hydrogen suppresses dislocation emission at general grain boundaries; promotes intergranular fracture	[67]
Leak detection, H2-blended pipelines	CNN + ANFIS (explainable AI)	H2-NG blend infrastructure	2.01% false alarm rate; ANFIS transparency addresses black-box concern for regulators	[69]

2.9 Integrity Assessment Tools and Knowledge Gaps

The literature reviewed in this chapter confirms that hydrogen embrittlement poses a measurable and grade-dependent threat to the mechanical integrity of API 5L pipeline steels under hydrogen-natural gas blend service conditions, manifesting as ductility loss, FT reduction, and fatigue crack growth acceleration that are especially pronounced in weld regions and higher-strength grades. Current regulatory frameworks, principally ASME B31.12, address these effects through either prescriptive grade limits that are overly conservative for much of the existing pipeline fleet, or performance-based qualification routes that require hydrogen-environment material data that most operators do not possess. Fitness-for-service procedures based on the failure assessment diagram provide the correct analytical structure but depend on accurate hydrogen-environment toughness inputs that are rarely available for the specific steel grades and weld conditions found in legacy infrastructure.

Machine-learning methods have demonstrated meaningful predictive capability for hydrogen-induced property degradation, yet existing models stop at property prediction and are not connected to fracture mechanics-based integrity outcomes such as stress intensity response, critical crack depth, or remaining life. No published framework currently integrates ML-predicted degradation with crack growth simulation across the full API 5L grade range, a range of blend levels, and a sensitivity analysis capable of identifying the dominant drivers of integrity risk. This gap, between data-driven property prediction and actionable integrity assessment, is precisely what this study addresses by developing a compatibility assessment model that links machine-learning surrogate predictions of RA, FT, and fatigue crack growth rate to a fracture mechanics-based life simulation framework consistent with ASME fitness-for-service principles.

CHAPTER 3

MACHINE-LEARNING DEVELOPMENT AND VALIDATION

3.1 Overview of ML Framework

This chapter presents the machine-learning models developed to predict the degradation of mechanical properties in carbon and low-alloy pipeline steels under hydrogen exposure. Four target properties are addressed: Reduction of Area (RA), Fracture Toughness (FT), Fatigue Crack Growth (FCG) rate, and Elongation. Each model was developed independently as a dedicated predictive tool, drawing on its own experimental and literature-compiled database, feature set, and algorithm selection process, though all four share a common methodological foundation rooted in supervised regression learning, systematic hyperparameter tuning, and performance evaluation across multiple statistical metrics. The RA model by Ahmed *et al.,* 2024 [14] established the foundational modeling architecture and introduced CatBoost as the preferred algorithm for predicting hydrogen-induced ductility loss. The FT model, developed by Gyaabeng *et al.,* 2025 [15], extended this approach to predicting FT reduction under gaseous hydrogen exposure, identifying k-nearest neighbors (KNN) as the optimal algorithm through a systematic model screening procedure. The FCG rate model, published by Ahmed *et al.,* 2025 [65], introduced a novel dual-model strategy in which a previously developed RA model is used to generate predicted RA values, which are then incorporated as an additional input feature into the fatigue model, thereby partially addressing the data scarcity that characterizes hydrogen-assisted fatigue research. The elongation model, developed by Iyiola *et al.,* 2025 [60], introduced a hybrid ensemble architecture combining gradient boosting and KNN regressors through a weighted soft-voting scheme, representing the first known application of hybrid ensemble learning specifically for predicting hydrogen-induced elongation reduction in low-carbon steels. These four models constitute the ML component of the integrated framework described in this study.

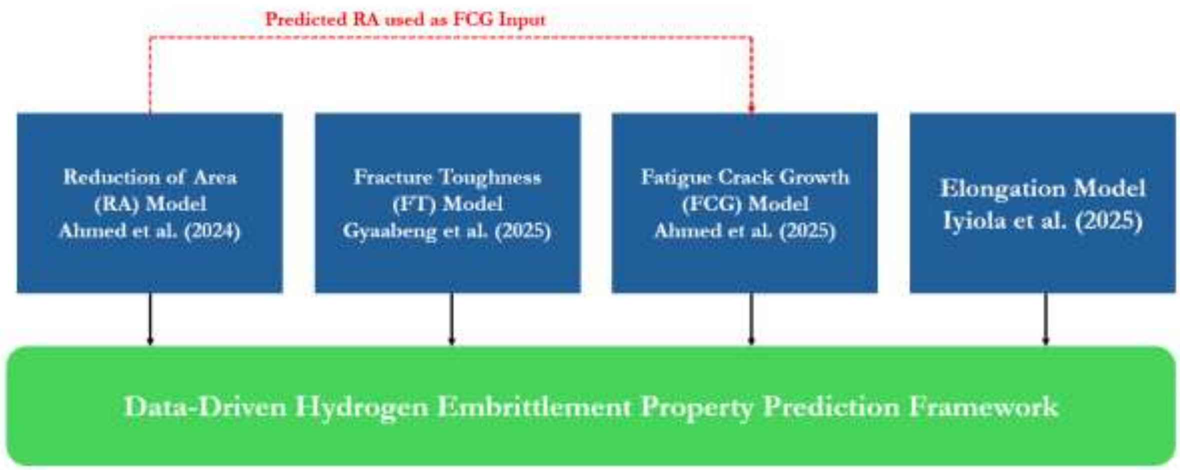

Figure 3-1 Overview of the Machine-learning Prediction Framework Developed for Hydrogen Embrittlement Assessment

3.2 Reduction of Area Model

The RA model was developed by Ahmed *et al.,* 2024 [14] to predict hydrogen embrittlement in low-carbon and low-alloy steels by quantifying the loss of ductility under pressurized hydrogen gas conditions. In this framework, RA was used as the target response because it reflects the extent of localized plastic deformation prior to fracture and therefore provides a practical measure of embrittlement severity. Since hydrogen exposure reduces ductility and promotes brittle cracking, a decrease in RA serves as an effective indicator of hydrogen-assisted material degradation. Within the overall machine-learning framework of this study, the RA model serves as the first predictive component and provides the basis for assessing hydrogen susceptibility in steels commonly used in gas transmission infrastructure. The model was built from a literature-based tensile test database compiled from authoritative published sources, including peer-reviewed journals, conference proceedings, and research reports.

The database incorporated data from studies such as [41], [45], [70], [71], [72], [73], [74], [75], [76], [77], [78], [79], [80]. These sources provided tensile test results for low-carbon and low-alloy steels exposed to air, helium, and high-pressure hydrogen gas. Only smooth-specimen tensile data were retained, while notched-specimen data were excluded because of limited availability and major data gaps. The final clean database contained 236 tensile tests from 47 distinct low-carbon and low-alloy steels and included 22 testing features. The input data captured the material chemistry, mechanical properties, and test conditions relevant to the assessment of hydrogen embrittlement. The raw database included features such as Fe, C, Mn, P, S, Si, Cr, Ni, Mo, Al, yield strength, ultimate tensile strength, aging time, hydrogen partial pressure, strain rate, heat treatment, product form, and hold stress, with RA as the response variable.

The authors emphasized that although other mechanical properties, such as ultimate tensile strength and elongation, could also reflect hydrogen effects, RA was selected because it directly represents the loss of ductility during tensile failure. The database covered a broad range of composition, strength, hydrogen pressure, and strain rate, enabling the model to learn material behavior under varied hydrogen service conditions. Data cleaning was treated as a critical step because of the sensitivity of machine-learning models to data quality. Missing values were handled by deletion rather than imputation, as the authors considered imputed values potentially unrepresentative of real-world behavior. Data authenticity was maintained by relying on primary sources rather than secondary reporting. In addition, only data obtained under direct gaseous hydrogen charging were considered, while electrochemical charging data were excluded because the method differs in how hydrogen atoms are produced, adsorbed, and absorbed, and a direct comparison between these measurements cannot be made Xu *et al.,* 2024 [78]. Suspicious or unreasonable data points were either excluded or carefully verified during compilation.

Preprocessing included feature scaling, outlier handling, and data encoding. Standardization was applied to algorithms sensitive to input magnitude, particularly ANN and GB, while tree-based models such as RF, DT, XGBoost, AdaBoost, and CatBoost were left unscaled because their split-based structure is insensitive to variable magnitude. Outliers were not removed automatically, since the authors interpreted many extreme values as real manifestations of variability among steels and test conditions rather than statistical noise. Categorical variables such as heat treatment, aging time, hold stress, and steel name were transformed into numerical form using label encoding so that they could be incorporated into regression modeling.

Feature selection was carried out using both engineering judgment and correlation analysis. Although the original database contained 22 parameters, only 17 were initially retained as potential predictors, and this set was further reduced. Product form, strain rate, and hold stress were excluded because they were inconsistently reported and contained substantial missing data. Aging time was also removed because hydrogen diffusion in low-carbon and low-alloy steels is relatively rapid, making this variable less necessary for the intended application. Correlation analysis then showed a strong positive relationship between yield strength and ultimate tensile strength, leading to the removal of yield strength to reduce redundancy. Chromium, nickel, and molybdenum were also excluded because of their strong negative correlation with iron. After these refinements, the final feature set consisted of ten parameters: Fe, C, Mn, P, S, Si, Al, heat treatment, hydrogen pressure, and ultimate tensile strength.

The model development stage compared seven supervised machine-learning algorithms: decision tree, random forest, AdaBoost, gradient boosting, XGBoost, CatBoost, and artificial neural network. The performance of the candidate models was evaluated using training and testing R^2, mean squared error, root mean square error, mean absolute error, and consistency in feature-importance ranking. Among the seven algorithms, CatBoost was selected as the optimal RA predictor because it showed the best overall balance across the evaluation metrics. CatBoost was also considered attractive because it can handle categorical and heterogeneous data efficiently, is robust to outliers, and is less prone to overfitting due to its oblivious-tree structure.

The final CatBoost model was trained on 80% of the data and tested on the remaining 20%. Hyperparameter tuning was performed using a combination of 10-fold cross-validation and a grid search. This approach reduced the risk of overfitting and systematically identified the most effective hyperparameter combination. For the selected CatBoost model, the optimized setup included a learning rate of 0.5, a tree depth of 3, and an L2-leaf regularization of 200, along with tuning of additional parameters, including subsampling, border count, random strength, and bagging temperature. The final model achieved training and testing R2 values of 0.7762 and 0.7250, respectively, with an MAE of 7.32, an MSE of 83.78, and an RMSE of 9.15. These results indicated that the CatBoost model provided the best overall fit among the tested algorithms and captured the relationships among material attributes, environmental variables, and hydrogen-related ductility loss with reasonable accuracy.

Feature-importance analysis showed that hydrogen pressure was the dominant predictor in the RA model, accounting for 47.4% of the total predictive influence. Ultimate tensile strength was the second most important feature at 19.2%, followed by iron at 9.8%, phosphorus at 7.2%, and silicon at 4.8%. Carbon and heat treatment each contributed about 3%, while manganese, aluminum, and sulfur had individually smaller effects. The strong influence of hydrogen pressure is consistent with hydrogen solubility and adsorption behavior, as higher pressure increases hydrogen uptake, thereby intensifying embrittlement. The importance of ultimate tensile strength suggests that steels with higher strength levels can still be vulnerable to hydrogen-assisted ductility loss, especially when stress concentrations facilitate hydrogen accumulation.

The contributions of phosphorus and silicon further underscore the role of microstructure and grain-boundary effects in hydrogen-assisted cracking. Sensitivity analysis was conducted using a base case for API 5L X70 steel, with selected variables changed individually while all others were held constant. The results showed that increasing hydrogen pressure caused a rapid drop in predicted RA at low pressures, after which the response approached a plateau, suggesting a saturation effect.

Increasing ultimate tensile strength led to a progressive reduction in predicted RA, consistent with the inverse relationship between strength and ductility under hydrogen exposure. Changes in iron content also influenced the predicted response, although its practical effect was smaller than those of pressure and strength. These trends confirmed that the model not only provided predictive capability but also reproduced physically meaningful hydrogen embrittlement behavior.

The RA model is a practical machine-learning tool for estimating hydrogen-assisted ductility degradation in low-carbon, low-alloy steels exposed to gaseous hydrogen. Its importance within the framework extends beyond RA prediction alone, as it later supports the fatigue crack growth study by providing predicted RA as an informative feature. As with the other models in this chapter, its reliability is strongest within the ranges of compositions, strengths, and hydrogen exposure conditions represented in the literature-derived database.

3.3 Fracture Toughness Model

The FT model was developed by Gyaabeng *et al.,* 2025 [15] to predict the degradation of fracture resistance in carbon and low-alloy steels exposed to gaseous hydrogen environments. Within the overall machine-learning framework of this study, the FT model serves as the component for estimating hydrogen-assisted loss in fracture performance under conditions relevant to pipeline materials and hydrogen transport applications. Unlike a purely experimental model derived from a single testing campaign, this model was constructed from a literature-based database assembled from multiple previously published studies. The underlying data were collected from peer-reviewed journal articles, technical reports from research organizations, and conference proceedings, with the database primarily representing FT tests conducted under ambient-temperature gaseous hydrogen exposure on carbon and low-alloy steels. The source data included works such as [38], [41], [62], [72], [82-88].

A key consideration in compiling the FT database was maintaining comparability across studies. The FT values reported in the different sources were not normalized prior to modeling because the measurements had already been obtained using recognized standardized procedures, including ASTM E1820, ASTM E399, or equivalent methods. In addition, environmental variability was reduced by selecting data generated under ambient-temperature conditions and from specimens exposed to gaseous hydrogen. This provided a more consistent basis for integrating test results from different laboratories while still preserving broad coverage of pressure, displacement rate, and material-property conditions. Initially, the database contained 210 FT records with 18 features. After data cleaning and removal of incomplete entries, 180 usable records were retained for machine-learning analysis.

The compiled dataset captured both material characteristics and test conditions relevant to hydrogen embrittlement. These included elemental composition, strength properties, hydrogen partial pressure, displacement rate, and the presence of gaseous impurities such as oxygen and carbon dioxide. During preprocessing, missing data were removed, and exploratory data analysis was performed using univariate and multivariate methods. All input variables were then normalized to account for differences in scale. Outliers were not removed indiscriminately; instead, they were treated on a case-by-case basis, as extreme observations were interpreted as potentially meaningful expressions of real material variability rather than mere noise. This approach was intended to preserve the range of physical behavior represented in the final model.

Feature selection was carried out in stages. Although the original database contained 18 variables, product form and heat treatment were excluded from the primary feature set due to inconsistent reporting and high rates of missing data. The authors still evaluated the effect of heat treatment separately, using the subset of records for which this information was available, and found that it contributed weakly compared with other predictors.

Correlation analysis showed that ultimate tensile strength and yield strength were highly correlated, so ultimate tensile strength was removed, and yield strength was retained as the representative mechanical property because it was more consistently reported and more practical for model use. After these refinements, the final input set consisted of 13 parameters: Fe, C, Mn, P, Al, Si, Cu, O_2, CO_2, displacement rate, hydrogen pressure, yield strength, and the grouped variable "other", representing the total content of minor alloying elements such as Mo, Ni, Cr, Nb, and Ti. Standardization was then applied to ensure that variables with different units contributed more evenly during model development.

The FT model development process followed a structured screening and selection procedure. Seven machine learning algorithms were initially considered: support vector machine, random forest, gradient boosting, k-nearest neighbors, artificial neural network, decision tree, and CatBoost. After feature-importance analysis and model prescreening, four models were retained for detailed comparison: KNN, RF, DT, and GB. The final model comparison relied on multiple performance indicators, including the coefficient of determination, mean absolute error, root mean square error, overfitting behavior, and 5-fold cross-validation consistency. Among the candidate models, KNN showed the strongest overall performance, with training and testing R^2 values of 0.85 and 0.84, respectively, and the lowest MAE and RMSE. It also demonstrated the most stable cross-validation performance, supporting its selection as the final FT predictor. The adopted KNN configuration used four neighbors, Euclidean distance, and distance-based weighting. Because KNN is a non-parametric method and does not directly provide feature-importance values, a surrogate gradient-boosted model was used to interpret the predictors' relative contributions. This analysis showed that hydrogen pressure was the dominant variable influencing FT prediction, accounting for approximately 32% of the modeled variation. Yield strength was the next most influential factor, followed by the grouped minor-alloying-element variable. Displacement rate and key alloying elements such as carbon and phosphorus also contributed meaningfully to the model's output. These results are physically reasonable, since hydrogen pressure governs the severity of hydrogen exposure, while material strength and composition influence crack initiation and propagation resistance in hydrogen service.

The selected KNN model was further used for parametric and sensitivity analysis to evaluate how FT responds to changes in major input variables. The model showed that FT decreases sharply at relatively low hydrogen pressures before approaching a plateau at higher pressures, suggesting that the embrittling effect intensifies quickly and then tends toward saturation. It also reproduced the inverse relationship between yield strength and FT degradation, consistent with the broader understanding that higher-strength steels are generally more susceptible to hydrogen-assisted cracking. In addition, the model indicated that low oxygen concentrations may reduce hydrogen embrittlement in X70 steel, likely by limiting hydrogen uptake, while lower displacement rates were found to be important for obtaining representative measurements during testing. These trends demonstrate that the FT model is not only predictive but also useful for interpreting the combined effects of material and environmental variables on hydrogen-related fracture behavior.

Like the other machine-learning models in this framework, the FT model is empirical and therefore most reliable within the bounds of the training data. Its predictions are best applied to steels whose chemical composition, strength level, and hydrogen exposure conditions fall within the range represented in the literature-derived database. Materials or service conditions that fall substantially outside those bounds may require additional data and retraining before the model can be used confidently. Even with this limitation, the FT model provides an efficient and practical tool for estimating hydrogen-related toughness degradation in steels relevant to existing and future hydrogen infrastructure.

3.4 Fatigue Crack Growth (FCG) Model

The fatigue crack growth (FCG) model was developed by Ahmed *et al.,* 2024 [14] to predict hydrogen-assisted crack propagation in carbon and low-alloy pipeline steels under cyclic loading conditions. Within the overall machine-learning framework of this study, the FCG model differs from the preceding models because it was designed not only as a direct predictive tool for the crack growth rate but also as a framework for mitigating the effects of data scarcity through cross-model information transfer. Specifically, the study introduced two parallel modeling strategies: a conventional model trained directly on fatigue test variables, and a novel dual-model approach in which fatigue test inputs were first passed through a previously developed RA model, after which the model-predicted RA was introduced as an additional feature for FCG prediction. This structure allowed the model to incorporate hydrogen-related ductility information that was not directly measured in every fatigue data record, thereby improving the representation of embrittlement effects in the final fatigue model.

The database used for FCG model development was assembled from published primary fatigue studies. The source data were compiled from the work of [42], [71], [74], [89], [90], [91], [92],

[93], [94]. These sources provided fatigue crack growth data for 16 unique carbon steel types, with additional welded and condition-specific variants increasing the number of sample classes to 36. In total, the full fatigue database contained 3,402 data points characterized by 26 original testing attributes. For the novel RA-assisted approach, the calculated RA value was added as an extra variable, increasing the input space to 27 attributes. The compiled records captured material chemistry, mechanical properties, and testing conditions relevant to hydrogen transport applications, while the study deliberately excluded data from electrochemical charging environments because they were not considered representative of gaseous hydrogen pipeline service. Instead, the selected measurements were limited to air, helium, and high-pressure hydrogen gas environments to preserve physical relevance to pipeline operation.

The developed database included a broad range of input variables, spanning chemical composition, strength properties, fracture mechanics parameters, and environmental loading conditions. These included elemental concentrations such as Fe, C, Mn, P, S, Si, Cr, Ni, Mo, Al, and Cu; mechanical properties such as yield strength and ultimate tensile strength; the stress intensity factor range, ΔK; hydrogen partial pressure; frequency; load ratio; product form; heat treatment; and gaseous species indicators. The target variable was the fatigue crack growth rate, da/dN, while predicted RA was used only in the novel model configuration. Summary statistics reported in the study indicate that the database covered a wide range of hydrogen pressures, loading frequencies, and crack growth rates, enabling the model to learn fatigue behavior under diverse hydrogen-assisted conditions relevant to steel pipelines.

Data preprocessing followed a structured sequence of cleaning, feature engineering, encoding, and scaling. Missing values were handled through deletion rather than imputation because the authors judged that filling missing entries from incompatible or incomplete sources could distort the physical trends represented in the data. Categorical variables such as steel name, heat treatment, and product form were label-encoded for compatibility with machine-learning algorithms. Outliers were screened using both traditional and adjusted boxplot methods. However, potentially extreme values were not automatically removed because many corresponded to valid experimental observations under unusual hydrogen-fatigue conditions. Instead, they were retained when supported by domain knowledge so that the model would preserve the full range of material behavior represented in the literature database.

Feature selection was guided by Pearson and Spearman correlation analyses. Strong correlations were used to reduce redundancy and limit multicollinearity in the final feature set. For example, yield strength and ultimate tensile strength showed a strong positive correlation, and aluminum and copper also exhibited a strong association in the rank-based analysis. To improve interpretability and avoid overfitting, yield strength and copper were excluded. In addition, the N2, CO2, and SO2 indicators were removed because they were largely binary presence-absence variables and did not provide sufficient variation for model training. After this screening process, the final feature set for the fatigue model was reduced to 18 variables: Fe, C, Mn, P, S, Si, Ni, Cr, Mo, Al, heat treatment, H2 pressure, O2 ppm, product form, frequency, load ratio, ΔK, and ultimate tensile strength.

Standardization was then applied to algorithms that benefit from scale normalization, while tree-based models such as CatBoost remained insensitive to feature scale. To improve model robustness and preserve representation across materials, the data were split using a stratified strategy based on steel type. Of the total 3,402 points, 96 data points from a single source were completely removed before training and reserved as an independent validation set. The remaining 3,306 points were then divided into 80% for training and 20% for testing. For the novel model, the withheld validation records were first passed through the RA model to obtain predicted RA values before fatigue prediction. Tenfold cross-validation was used during hyperparameter tuning to monitor generalization and reduce overfitting. This two-level validation process, consisting of both train-test evaluation and external, unseen-data validation, provided the authors with a stronger basis for comparing the conventional and RA-assisted models.

Several machine-learning algorithms were evaluated during model screening, including KNN, random forest, decision tree, XGBoost, AdaBoost, gradient boosting, and CatBoost. Model comparison was based on the coefficient of determination, mean squared error, root mean square error, mean absolute error, and consistency of feature-importance ranking. Among the tested models, CatBoost showed the strongest overall performance and was selected as the final algorithm for the FCG model. In the conventional setup, CatBoost achieved training and testing R^2 values of 0.9215 and 0.8542, respectively, with an MSE of 1.49×10^{-6}, RMSE of 0.0012, and MAE of 0.00031. This performance, together with its robustness to outliers, efficient handling of categorical variables, and balanced generalization behavior, supported its selection as the optimal model for fatigue crack growth prediction. Hyperparameter optimization for the CatBoost model was performed using a combined grid search and 10-fold cross-validation. The study explored multiple values for depth, learning rate, regularization, subsampling, number of iterations, and additional CatBoost-specific parameters. The final selected configuration used 2,000 iterations, a learning rate of 0.08, depth of 6, L2-leaf regularization of 3, RMSE as the loss function, a random seed of 42, and a subsample value of 1. This optimized setup was adopted because it provided the most favorable balance between prediction accuracy and resistance to overfitting.

A major contribution of this study was the comparison between the conventional fatigue model and the novel RA-assisted model. Although both models showed similar statistical performance on the train-test split, the novel model consistently performed better under more stringent validation criteria. The RA-assisted model produced training and testing R^2 values of 0.9192 and 0.8585, respectively, indicating slightly better test performance and reduced overfitting relative to the conventional model. It also reduced the maximum relative error from 125.13 in the conventional model to 93.90 in the RA-assisted model. When tested on the withheld independent 96-point validation set, the novel model achieved a mean relative error of 10.06, compared with 11.65 for the conventional model, corresponding to a 15.65% improvement in accuracy.

The study further reported that more than 93% of predictions from the novel model fell within a 10% error margin, indicating tighter agreement with measured values and better predictive consistency on unseen data. Model interpretation results showed that the stress intensity factor range, ΔK, was the dominant predictor of FCG behavior, followed by hydrogen pressure, ultimate tensile strength, and load ratio. This ranking is physically reasonable because ΔK directly controls the crack-driving force, hydrogen pressure influences the severity of embrittlement, and load ratio affects crack-opening and closure behavior during cyclic loading. Including predicted RA in the novel model provided complementary information on hydrogen-induced ductility loss, thereby improving predictive accuracy, even though the overall gain in traditional performance metrics was modest. The study therefore demonstrated that integrating hydrogen-sensitive mechanical indicators from other models can strengthen fatigue prediction when direct fatigue data are limited.

The FCG model provides a practical data-driven framework for estimating hydrogen-assisted fatigue crack growth in steels used for gas transmission infrastructure. Its most important contribution is not only the predictive CatBoost model itself, but also the demonstration that one hydrogen embrittlement model can inform another through model-generated features. This makes the FCG framework especially valuable in domains where experimentally measured fatigue data remain limited. Like the other models in this chapter, however, its reliability is strongest within the range of material classes, loading conditions, and gaseous environments represented in the literature-derived training database.

3.5 Elongation Model

The elongation model, developed by Iyiola *et al.,* 2025 [60], was designed to predict the hydrogen-induced reduction in tensile elongation of low-carbon steels. Within the integrated machine-learning framework of this study, elongation serves as a direct quantitative measure of ductility loss under hydrogen exposure. While RA and ultimate tensile strength also reflect hydrogen-induced mechanical degradation, elongation provides uniquely critical insight because it captures the material's ability to deform plastically prior to fracture. A reduction in elongation below accepted service thresholds signals an elevated risk of embrittlement and provides actionable information for pipeline integrity screening. As the final mechanical response targeted by the machine-learning framework, elongation complements the RA, FT, and fatigue crack growth models developed in the preceding sections, enabling a more complete characterization of hydrogen embrittlement across multiple damage modes.

Despite its physical significance, elongation had not been specifically targeted in prior machine-learning studies of hydrogen embrittlement in low-carbon steels. Although recent studies had applied ML to predict various aspects of HE in metals broadly, none had developed a predictive architecture specifically for hydrogen-induced reduction in elongation in this steel class. This study addresses that gap by constructing a literature-based database of tensile elongation data from multiple experimental sources, developing and evaluating seven machine-learning models, introducing a novel multi-metric model selection framework, and combining the two top-performing algorithms into a hybrid ensemble model using a weighted soft voting approach. The result is the first known application of hybrid ensemble learning to predict hydrogen-induced ductility loss through elongation reduction in low-carbon steels, providing a data-driven tool that can be integrated directly into pipeline compatibility assessment workflows.

3.5.1 Database Compilation

The database was compiled from 25 experimental sources, including peer-reviewed journal articles, conference proceedings, and technical reports, as listed in Table 3-1. These sources collectively provided tensile test data for low-carbon and low-alloy steels tested in air, helium, and high-pressure hydrogen gas environments. A total of 246 data points were collected from the published sources, with the largest single contribution from Hoover *et al.,* 1981 [72], which provided 54 data points. Other significant sources included [41], [73], [74], [91], [95], and [72]. The diversity of sources was intentional, ensuring the database represented a wide range of steel compositions, heat-treatment conditions, hydrogen partial pressures, and test protocols. This breadth is essential for a model intended to generalize across the pipeline steel grades commonly encountered in hydrogen transport infrastructure. The data collected for model development encompassed three categories of features: mechanical properties, chemical composition, and test conditions. Mechanical property inputs included yield strength, elongation, and RA. Chemical composition inputs covered the elemental concentrations of iron, carbon, manganese, phosphorus, sulfur, silicon, chromium, nickel, molybdenum, and aluminum. Test condition inputs included aging time, hydrogen partial pressure, strain rate, heat treatment, and hold stress. Table 3-2 presents the full range of these input features across the compiled database. The dataset specifically targets low-carbon and low-alloy steel materials and is based exclusively on smooth-specimen tensile tests conducted under direct gaseous hydrogen charging, consistent with conditions relevant to pressurized hydrogen gas transport.

Table 3-1 Data Sources and Corresponding Number of Collected Data Points

Data Source	Total Number of Collected Data Points
Hoover	54
Ningileri, Boggess	31
Walter, Chandler	25
Loginow, Phelps	22
Cialone, Holbrook	21
Hoover, Iannucci	18
Hoover, Robinson	13
Jewett, Walter	10
Campbell	09
Keller, Somerday	06
Bandyopadhyay, Kameda	05
San Marchi, Somerday	05
An, Zhang	04
Robinson	03
Wachob, Nelson	03
Walter, Chandler	02
Clark, Landes	01
Fukuyama, Yokogawa	01
Padmanabhan, Wood	01
Takeda, McMahon	01
Walter, Chandler	01
Nanninga et al.	02
Konert et al.	08
Zhao et al.	02
Michler et al.	06

Table 3-2 Dataset summary showing input feature categories, parameters, data ranges, and units [60].

Categories	Parameters	Data Range (Min/Max)	Units
Mechanical Properties	Yield Strength (YS)	41.40/1550	MPa
	Elongation	1.6/63	%
	Reduction of Area (RA)	6.50/96.00	%
Chemical Properties	Iron (Fe)	92.61/99.31	%
	Carbon (C)	0.03/0.85	%
	Manganese (Mn)	0.007/1.70	%
	Phosphorus (P)	0.00/0.04	%
	Sulfur (S)	0.00/0.05	%
	Silicon (Si)	0.00/0.32	%
	Chromium (Cr)	0.00/2.46	%
	Nickel (Ni)	0.00/4.91	%
	Molybdenum (Mo)	0.00/0.94	%
	Aluminum (Al)	0.00/0.42	%
Test Conditions	Aging Time	0.00/7.00	Day
	Hydrogen Partial Pressure	0.10/97.00	MPa
	Strain Rate	$2\times10^{-6}/3\times10^{-4}$	S^{-1}
	Heat Treatment	Different heat treatments	–
	Hold Stress	0.00/9.00	MPa

* *Pipeline, Plate, Steel Bar, Rail Web*

3.5.2 Data Preprocessing

High-quality data are fundamental to effective machine-learning model development. The preprocessing workflow for the elongation database followed a structured sequence of cleaning, standardization compliance filtering, outlier assessment, and feature scaling. A univariate statistical analysis was first performed across all 254 collected data points to examine the distribution of each feature, identify anomalies, and assess the presence of missing values. This initial review revealed that 25 elongation values were missing due to inconsistent reporting across sources and were discarded from further analysis. The resulting dataset of 229 usable records was then filtered to retain only data generated under ASTM E8/E8M standardized smooth-specimen tensile testing protocols, ensuring that input features such as yield strength and elongation were measured under comparable conditions. After applying this criterion, 211 data points were retained for model development, with 18 data points further reserved for independent validation of the final hybrid model.

Outlier detection was conducted using box plot visualization, as shown in Figure 3-2. The plots revealed outliers in several features, including hydrogen partial pressure, yield strength, carbon, manganese, phosphorus, sulfur, and silicon. Rather than automatically removing these extreme observations, each was examined in the context of physical plausibility. Extreme values were retained when they corresponded to valid experimental conditions, since high-pressure and high-strength conditions are precisely the scenarios most relevant to assessing severe hydrogen embrittlement. The presence of heterogeneity across the compiled sources was also acknowledged as a potential source of bias, arising from differences in experimental protocols, measurement methodologies, and reporting conventions. While the ASTM E8/E8M filtering, cleaning, and feature standardization steps were designed to mitigate these effects, the presence of embedded experimental noise or unaccounted covariates could not be entirely eliminated. Feature standardization was applied using z-score normalization to ensure that no single variable exerted a disproportionate influence on model predictions due to scale differences. The standardization equation used is given in Equation 3.1, where S_new is the standardized value, S is the original data point, and μ and σ denote the dataset's mean and standard deviation, respectively. This step is particularly important for distance-based algorithms such as KNN, whose predictions depend directly on the relative magnitude of input variables, and for gradient-based algorithms where unscaled inputs can cause uneven convergence.

$$\text{S\_new} = \frac{S - \mu}{\sigma} \qquad 3\text{-}1$$

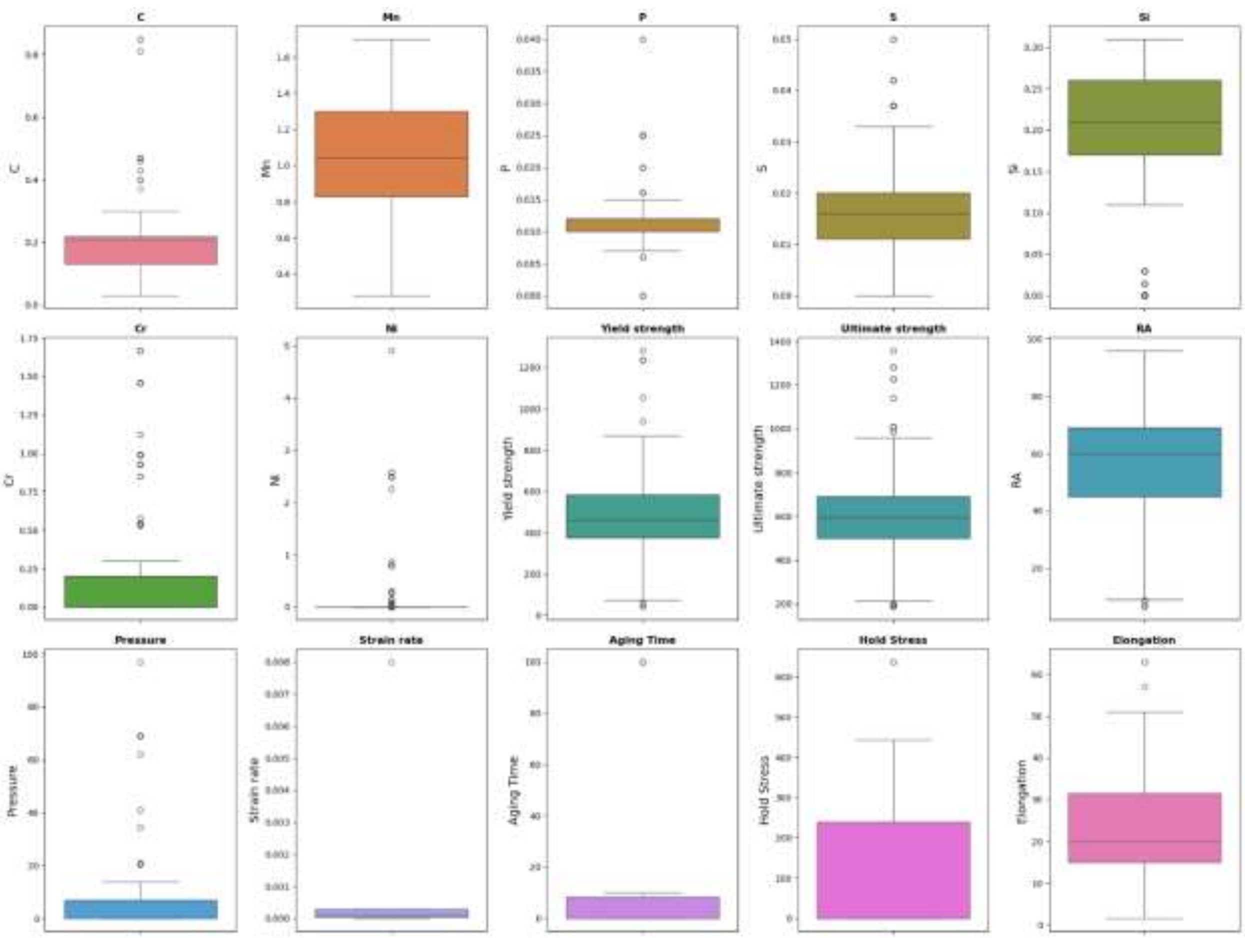

Figure 3-2 Box Plot Visualization of Feature Distributions and Variability across the Elongation Database *[60]*.

3.5.3 Feature Engineering

Feature engineering was conducted in two stages: feature selection and feature scaling. The raw database initially contained 22 parameters, of which 17 were retained as candidate inputs following an initial domain-based screening. These 17 candidates were: strain rate, hydrogen partial pressure, yield strength, ultimate tensile strength, aging time, hold stress, elemental concentrations of Fe, C, Mn, P, S, Si, Cr, Ni, Mo, and Al, and heat treatment. Strain rate was subsequently excluded because a prior study by Ronevich *et al.,* 2017 [93] demonstrated that strain rates below 8.3 x 10^{-4} s^{-1} have less than 20% impact on the HE assessment of low-carbon steel based on maximum strain. The dataset strain rates ranged from 2.1 x 10^{-6} to 3 x 10^{-4} s^{-1}, falling entirely within that low-sensitivity range, making its inclusion unlikely to improve predictive accuracy. Correlation analysis, represented in the heatmap in Figure 3-3, provided additional guidance for feature reduction. Yield strength and ultimate tensile strength exhibited a strong positive correlation ($r = 0.93$), indicating substantial redundancy. Yield strength was retained because it is a critical predictor of material susceptibility to deformation and embrittlement and was more consistently reported across the source database. The strong negative correlation between Fe and Ni (-0.81) indicated multicollinearity among elemental variables. Ridge regression was applied to mitigate multicollinearity among Fe, Ni, Cr, and Mo by regularizing their coefficient magnitudes. Hold stress and product form were excluded because they contained high rates of missing data. Heat treatment was also excluded due to inconsistent encoding across sources, which limited its utility as a modeling input. The final feature set consisted of 12 input parameters: yield strength, hydrogen partial pressure, and the elemental concentrations of Fe, C, Mn, P, S, Si, Al, Ni, Cr, and Mo.

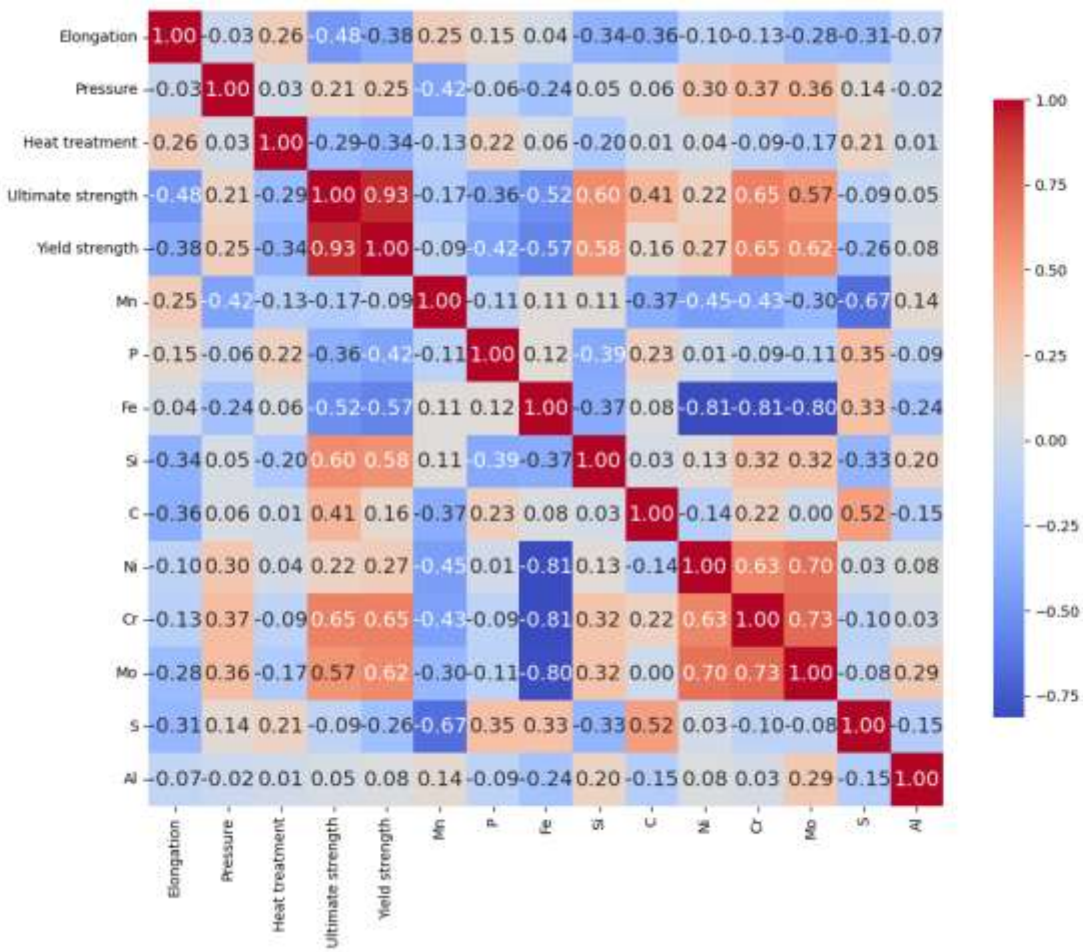

Figure 3-3 Correlation Heatmap of Input Features in the Database [60]

3.5.4 Initial Development of Seven Machine-learning Models

Seven supervised machine-learning algorithms were developed as candidate predictors for hydrogen-induced elongation reduction. The dataset was split randomly into training and testing sets using an 80:20 ratio, with 80% of the 211 usable records used for model training and 20% reserved for evaluation. For each model, hyperparameter tuning was performed using an exhaustive grid search approach combined with 5-fold cross-validation. This strategy systematically evaluates all possible combinations of specified hyperparameters and averages performance across five data folds, providing a reliable estimate of generalization performance and reducing the risk of overfitting. The seven models are described below.

Random Forest, developed by Leo Breiman, constructs an ensemble of decision trees during training and combines their outputs to enhance accuracy and reduce overfitting. Each tree is trained on a random subset of features and data to improve variance reduction and robustness. For regression, the outputs of all trees are averaged [96]. The Random Forest model achieved a training R^2 of 0.89 and a test R^2 of 0.80, with RMSE of 5.54 and MAE of 3.79, reflecting a reasonable balance between fit and generalization but with a notable gap between training and test performance, indicating some overfitting. The Decision Tree algorithm recursively partitions the feature space based on the most significant variable at each node, producing a structure where internal nodes represent feature tests, branches correspond to outcomes, and leaf nodes represent predicted values. While interpretable and easy to implement, decision trees are prone to overfitting when grown without constraint [97]. The Decision Tree model achieved a training R^2 of 0.83 and a test R^2 of 0.80, with an RMSE of 5.47 and an MAE of 3.92, the highest error values among the individual models.

The K-Nearest Neighbors (KNN) algorithm is a non-parametric, instance-based method that predicts the value of a query point by averaging the values of its k nearest neighbors in feature space, identified using Euclidean, Manhattan, or Minkowski distance metrics. The value of k is selected by cross-validation to avoid overfitting or underfitting. KNN is computationally straightforward but sensitive to irrelevant features and the scale of input variables, making standardization essential [97], [98]. The KNN model achieved a training R^2 of 0.86, a test R^2 of 0.85, RMSE of 4.77, and MAE of 3.54, showing strong generalization with the smallest gap between training and test R^2 of any individual model. Gradient Boosting constructs an ensemble of decision trees sequentially, where each new tree is trained to predict the pseudo-residuals of the previous model's predictions. This iterative error-correction approach is known for high predictive accuracy and flexibility [99], [100]. The Gradient Boosting model demonstrated the best individual performance, achieving a training R^2 of 0.88, a test R^2 of 0.86, an RMSE of 4.62, and an MAE of 3.18. These metrics, combined with minimal bias and variance, confirmed its effectiveness at capturing the nonlinear relationships governing the reduction in hydrogen-induced elongation. CatBoost, developed by Yandex, is a gradient boosting algorithm specifically designed to handle categorical features natively without requiring extensive preprocessing such as one-hot encoding. Its oblivious-tree structure offers inherent resistance to overfitting, and it is particularly effective for datasets containing a mix of categorical and continuous variables [101], [102]. XGBoost (Extreme Gradient Boosting) incorporates advanced regularization methods to prevent overfitting and is engineered for high computational efficiency, using a boosting ensemble of weak learners to progressively improve prediction accuracy [103]. Support Vector Regression (SVR) extends the principles of support vector machines to regression by finding a function that deviates from measured values by no more than a predefined margin, employing kernel functions to model nonlinear relationships in high-dimensional feature spaces [104]. Figure 3-4 shows the measured-versus-predicted elongation correlation plots for four of the seven individual models: Random Forest, KNN, Decision Tree, and Gradient Boosting. Visual inspection of the scatter plots confirms the quantitative rankings reported in the evaluation metrics, with Gradient Boosting and KNN showing the tightest alignment with the ideal 1:1 line.

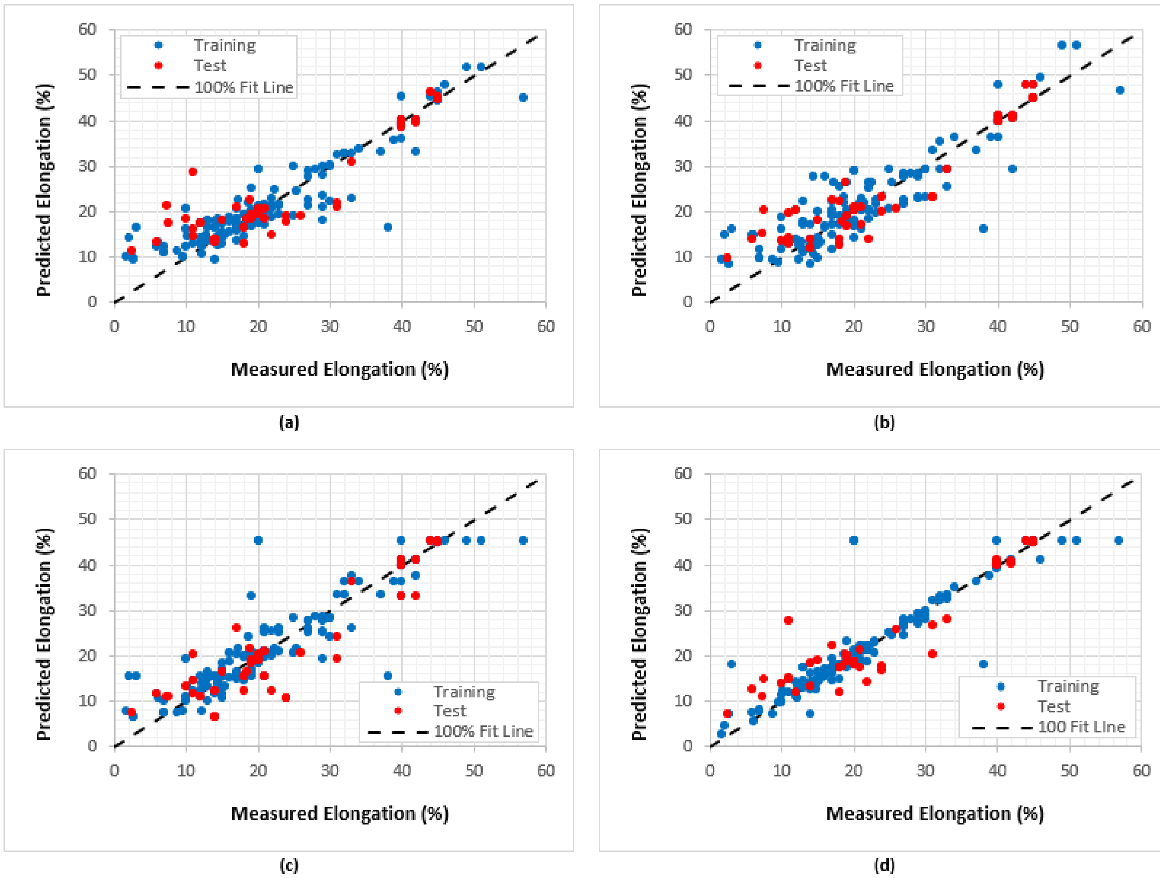

Figure 3-4 Correlation plots of measured and predicted elongation for four Individual ML Models: (a) Random Forest (b) KNN (c) Decision Tree (d) Gradient Boosting *[60]*

Figure 3-5 shows the 5-fold cross-validation RMSE values for the same four models, illustrating the variation in prediction error across validation folds. Lower and more consistent RMSE values across folds indicate better model stability and generalization capacity.

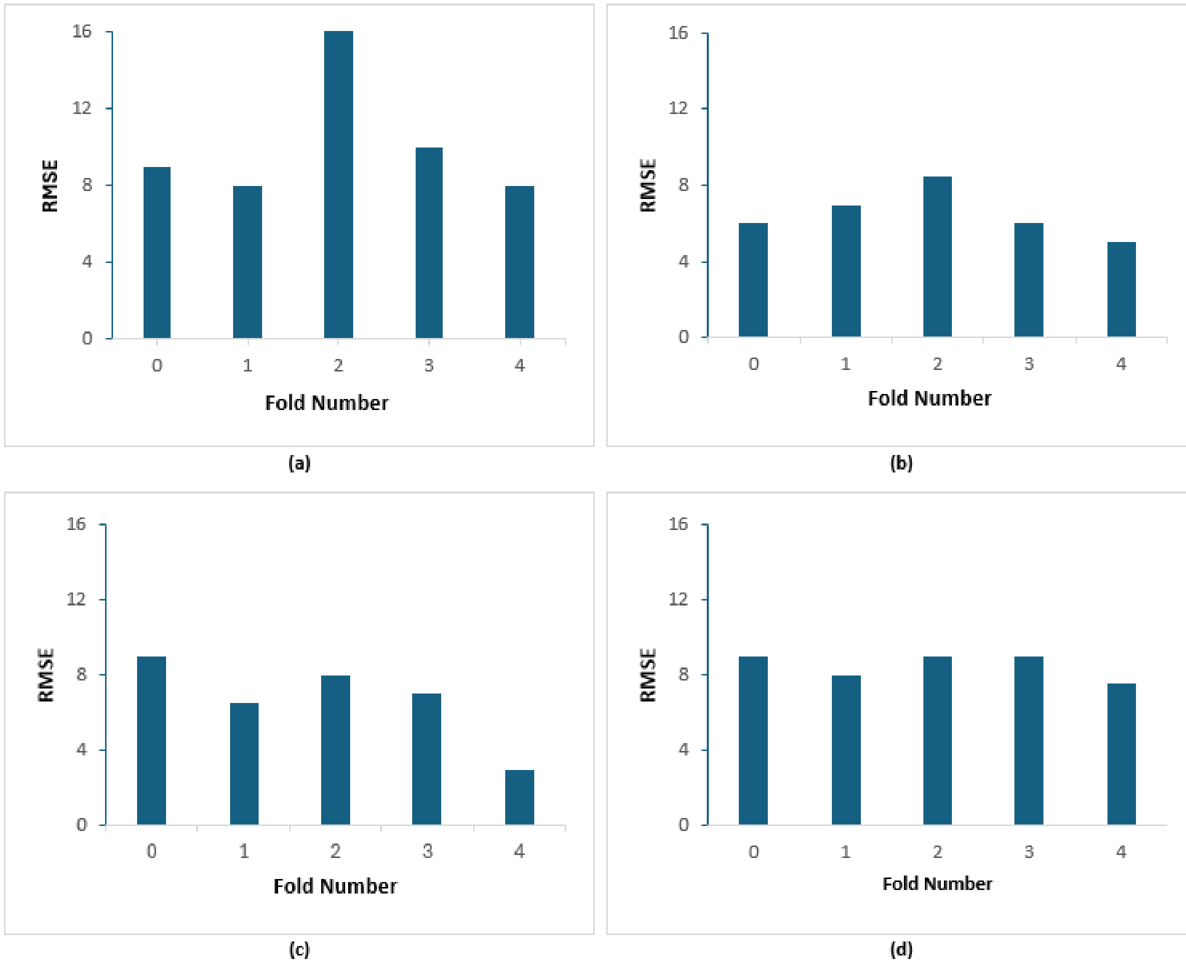

Figure 3-5 Root Mean Square Error (RMSE) Values from 5-Fold Cross-Validation for: (a) Random Forest, (b) KNN, (c) Decision Tree, (d) Gradient Boosting *[60]*

3.5.5 Novel Multi-Metric Model Selection Framework

A key methodological contribution of this study is the introduction of a novel model selection framework that evaluates candidate algorithms holistically across five distinct performance metrics rather than relying on a single criterion such as test R^2. Conventional model selection based on a single metric risks choosing a model that excels in one dimension while underperforming in others, such as a model with high R^2 but poor error metrics, large overfitting gaps, or physically inconsistent feature importance rankings. The five metrics incorporated into this framework are: (i) feature importance, (ii) training R^2, (iii) delta-R^2 (the absolute difference between training and test R^2 as a measure of overfitting), (iv) RMSE, and (v) MAE. Each model was ranked independently on each metric, and the cumulative point totals were used to identify the top-performing algorithms for hybrid ensemble development.

The first selection criterion was feature importance. Critical parameters governing hydrogen embrittlement, specifically pressure and yield strength, are well established in the literature. Models that correctly identified these as the most influential predictors were considered physically reliable and were ranked higher. Each model's feature importance outputs were compiled across all seven algorithms, and the average importance of each feature was calculated to produce a consensus ranking. Table 3-3 presents the feature importance rankings from all seven models along with the average ranks. The top four features by average importance were pressure (rank 1), yield strength (rank 2), iron (rank 3), and carbon (rank 4). Each model was then scored based on the alignment of its own feature importance rankings with these consensus top four features, and the absolute deviations from the consensus ranking were summed to produce an overall model rank by feature importance, as shown in Table 3-3.

Table 3-3 Feature Importance Ranking from Seven ML Models *[60]*

Model	Pressure	YS	Fe	C	Al	Mn	Si	S	P	Ni	Mo	Cr
Random Forest	1	2	3	5	8	6	7	4	10	11	9	12
Decision Tree	5	2	8	4	1	6	3	10	7	9	12	11
KNN	1	12	7	3	5	9	4	11	2	6	8	10
Gradient Boost	1	2	4	8	3	5	7	6	9	10	11	12
Cat Boost	2	3	1	10	5	7	4	9	8	12	6	11
XGBoost	3	1	2	4	6	8	7	5	12	9	11	10
SVR	1	10	9	5	12	2	11	3	8	6	7	4
AVERAGE	**2.0**	**4.6**	**4.9**	**5.6**	**5.7**	**6.1**	**6.1**	**6.8**	**8.0**	**9.0**	**9.1**	**10.0**
RANK	**1**	**2**	**3**	**4**	**5**	**6**	**6**	**7**	**8**	**9**	**10**	**11**

The subsequent selection criteria were applied through separate ranking tables for training R^2 (Table 3-4), ΔR^2 (Table 3-5), RMSE (Table 3-6), and MAE (Table 3-7). Models with higher training R^2 values were ranked more favorably because they demonstrated stronger learning capacity. Models with lower ΔR^2 were ranked higher because a small gap between training and test performance indicates better generalizability and reduced overfitting. Lower RMSE and MAE values reflect higher absolute prediction accuracy and were ranked accordingly. The cumulative scoring table, shown in Table 3-8, aggregates the ranks across all five criteria. Gradient Boosting emerged as the top-ranked model with a total point score of 8, followed by KNN with a total of 14. These two algorithms were selected as the component models for the development of a hybrid ensemble model. This multi-metric approach ensures that the selected models perform consistently well across accuracy, generalizability, and physical interpretability, rather than being optimized for a single statistical measure.

Table 3-4 through 3-8. Training R^2, ΔR^2 RMSE, MAE and cumulative scoring ranks for all seven individual models [60].

Table 3-4 Models' Train R^2 Rank

Model	Train R^2	Rank
Random Forest	0.89	1
Decision Tree	0.83	6
KNN	0.86	4
Gradient Boost	0.88	2
Cat Boost	0.89	1
XGBoost	0.84	5
SVR	0.87	3

Table 3-5 Models' ΔR^2 Rank

Model	ΔR^2	Rank
Random Forest	0.09	4
Decision Tree	0.03	3
KNN	0.01	1
Gradient Boost	0.02	2
Cat Boost	0.09	4
XGBoost	0.02	2
SVR	0.09	4

Table 3-6 Models' RMSE Rank

Model	RMSE	Rank
Random Forest	5.54	6
Decision Tree	5.47	4
KNN	4.77	2
Gradient Boost	4.62	1
Cat Boost	5.48	5
XGBoost	5.18	3
SVR	5.76	7

Table 3-7 Models' MAE Rank

Model	MAE	Rank
Random Forest	3.79	4
Decision Tree	3.92	5
KNN	3.54	3
Gradient Boost	3.18	1
Cat Boost	3.99	6
XGBoost	3.54	3
SVR	3.35	2

Table 3-8 Cumulative Scoring Rank

Model	Feature Importance	Train R^2	ΔR^2	RMSE	MAE	Total Points	Overall Rank
Random	1	1	4	6	4	16	3rd (tie)
Decision	5	6	3	4	5	23	6th
KNN	**4**	**4**	**1**	**2**	**3**	**14**	**2nd**
Gradient	**2**	**2**	**2**	**1**	**1**	**8**	**1st**
Cat Boost	4	1	4	5	6	20	4th
XGBoost	3	5	2	3	3	16	3rd (tie)
SVR	5	3	4	7	2	21	5th

3.5.6 Hybrid Ensemble Model Development

Hybrid ensemble models combine the predictive strengths of multiple individual algorithms to improve overall accuracy, reduce variance, and mitigate the specific limitations of any single model. This approach is particularly valuable in complex prediction tasks where diverse data patterns must be captured simultaneously. In the context of predicting reduced elongation under hydrogen exposure, a hybrid architecture is advantageous because the two component models contribute complementary capabilities: Gradient Boosting excels at capturing complex, nonlinear interactions within the feature space, while KNN offers simplicity and strong performance on datasets of moderate size by leveraging the proximity of training observations. By combining these two models, the ensemble is designed to achieve a more reliable and accurate prediction system than either component could provide independently. The hybrid model was constructed by combining the outputs of the two top-performing individual models through a weighted soft voting strategy. In ensemble learning, voting-based methods work by allowing each constituent model to generate an independent prediction, which is then aggregated into a single final output [105], [106]. Hard voting achieves this by selecting whichever prediction appears most frequently, whereas soft voting computes a continuous aggregate by averaging the predicted values across models, which tends to produce a more refined and stable result [106]. A weighted formulation of soft voting was adopted here so that the two component models contributed unequally to the final prediction, with their respective weights reflecting their relative predictive performance as determined during the model selection stage. Weighted soft voting has been shown to outperform individual models by combining probabilistic outputs to dampen prediction variance and improve overall reliability [105]. Accordingly, the Gradient Boosting model was assigned a weight of 80%, consistent with its first-place ranking across all five evaluation criteria, while the KNN model was assigned the remaining 20%, a contribution sufficient to provide complementary predictive information without undermining the dominant influence of the stronger component.

The hybrid ensemble model achieved a training R^2 of 0.89 and a test R^2 of 0.87, with RMSE of 4.45 and MAE of 3.16. These results represent a meaningful improvement over both individual component models. Compared to Gradient Boosting alone (test R^2 = 0.86, RMSE = 4.62, MAE = 3.18) and KNN alone (test R^2 = 0.85, RMSE = 4.77, MAE = 3.54), the hybrid model reduced RMSE by 3.7% relative to Gradient Boosting and by 6.7% relative to KNN, while also reducing MAE relative to both components. Figure 3-6 shows the cross-plot of measured versus predicted elongation for the hybrid model, with data points showing tighter clustering around the ideal Y = X line and a greater concentration within the +/-25% error bounds compared to the individual models.

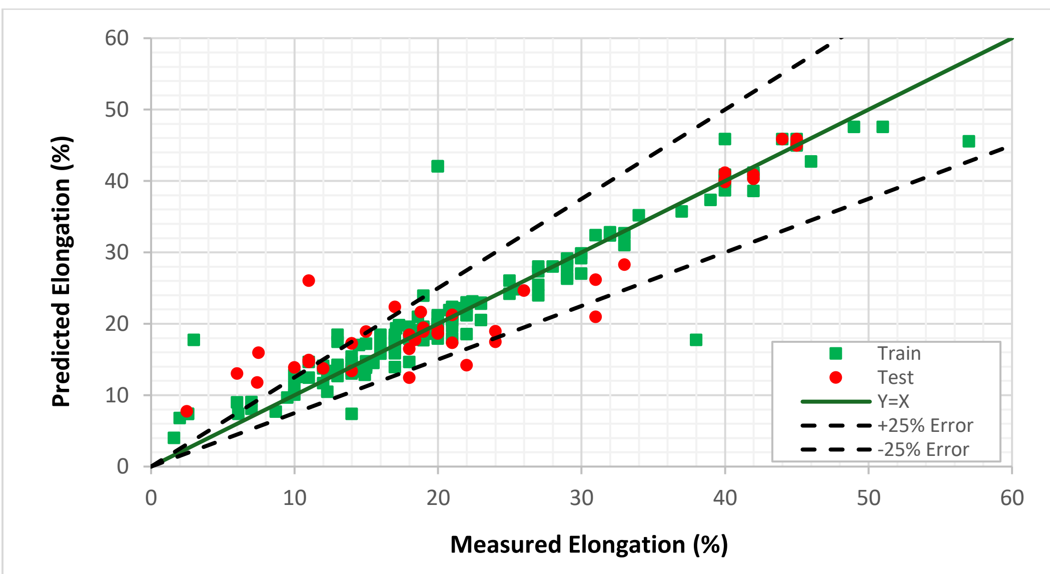

Figure 3-6 Hybrid ensemble model evaluation: measured versus predicted elongation showing training and test set performance within +/-25% error bounds *[60]*

Figure 3-7 presents a comparative bar chart of the training R^2, test R^2, RMSE, and MAE values for KNN, Gradient Boosting, and the hybrid model, confirming the hybrid model's consistent improvements across all four metrics.

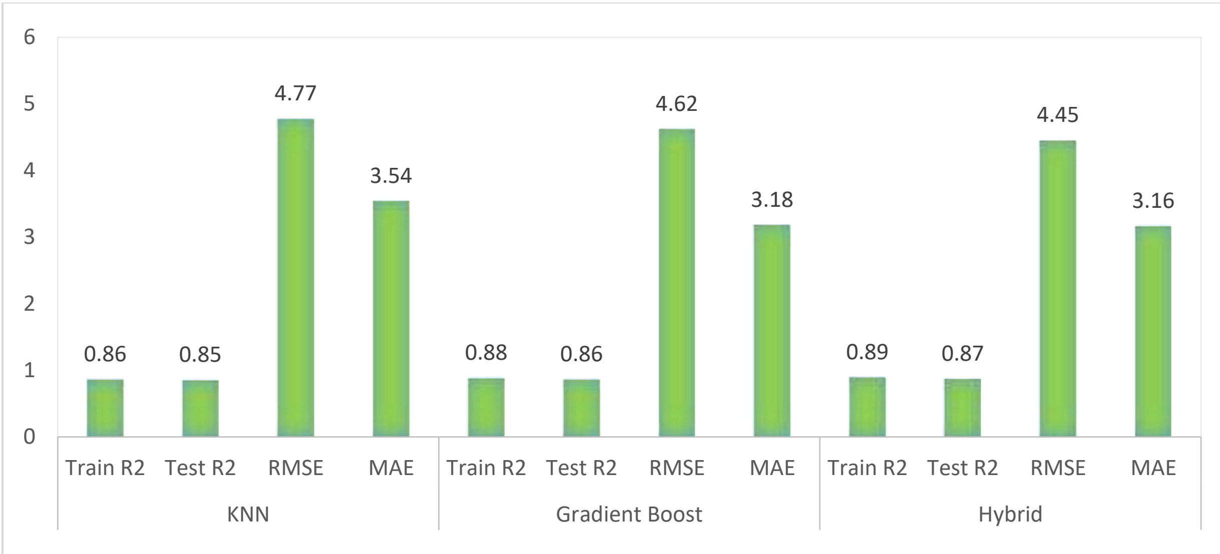

Figure 3-7 Comparison of evaluation metrics (training R^2, test R^2, RMSE, and MAE) for the KNN, Gradient Boosting, and hybrid ensemble models *[60]*

3.5.7 Feature Importance and Sensitivity Analysis

Feature importance analysis of the hybrid ensemble model revealed that hydrogen partial pressure was the dominant predictor, contributing 29.5% of the total predictive influence, followed by yield strength (13.3%), iron content (11.4%), and carbon content (10.5%). The remaining predictive weight was distributed across the alloying elements manganese, phosphorus, aluminum, silicon, sulfur, nickel, molybdenum, and chromium, in descending order of importance. These rankings are physically consistent with established hydrogen embrittlement mechanisms: pressure governs hydrogen solubility and surface adsorption, yield strength determines a material's resistance to hydrogen-assisted cracking, and the carbon and iron contents control the microstructural features that regulate hydrogen trapping and diffusion. The alignment between the model's feature rankings and the broader HE literature confirms the physical interpretability of the hybrid ensemble architecture. Sensitivity analysis further validated these findings by systematically varying the top four features across three representative steel types, namely soft (X42), medium-strength (AISI 1020), and hard (HY-130) steels, while holding all other parameters constant. The results showed that predicted elongation decreased consistently with increasing hydrogen pressure, yield strength, and carbon content across all material classes, with hard steel exhibiting the most pronounced pressure-driven ductility reduction. Iron content produced a smaller but directionally consistent effect. These trends reproduce the physically expected behavior of low-carbon steels under hydrogen exposure and confirm that the model generalizes reliably across the range of material and environmental conditions represented in the training database.

3.6 Selection of Machine-learning Models for Framework Integration

Four machine-learning models were developed and presented in this chapter, each targeting a distinct mechanical response to hydrogen exposure: RA, FT, fatigue crack growth rate, and elongation. However, not all four were carried forward into the integrated OU HEAT framework. Following a systematic review of the predictive outputs, their roles within pipeline integrity assessment, and their alignment with established evaluation criteria in hydrogen service standards, three models were selected for integration: the RA model, the FT model, and the fatigue crack growth model.

The elongation model, while statistically sound and representing a genuine methodological contribution to the hydrogen embrittlement literature, was ultimately excluded from the integrated framework on the basis of functional redundancy and limited additional value for integrity-based decision-making. In the context of pipeline integrity assessment, RA is the more operationally significant ductility indicator because it directly quantifies the localized plastic deformation that precedes fracture at the failure cross-section, which is the physically relevant failure condition in pressurized pipeline systems [45], [107]. Elongation, by contrast, reflects the total accumulated plastic strain along the gauge length and is more sensitive to specimen geometry, gauge length definition, and testing protocol variability [27], making it a less standardized and less directly actionable metric for integrity screening purposes. Furthermore, RA is the ductility parameter explicitly referenced in hydrogen embrittlement index formulations used in industry standards such as ASME B31.12 [58], where the embrittlement index is defined as the fractional reduction in RA under hydrogen relative to an inert reference condition [45]. Elongation does not occupy an equivalent role in these standardized assessment criteria. Additionally, within the framework itself, predicted RA already functions as a cross-model transfer variable, serving as an additional input feature in the fatigue crack growth model to account for hydrogen-induced ductility loss. Introducing elongation as a separate parallel ductility output would create metric redundancy without a defined pathway for its use in downstream fracture mechanics calculations. For these reasons, the elongation model is best understood as a complementary research contribution rather than a core component of the integrity assessment framework, and its exclusion does not diminish the comprehensiveness of the integrated tool.

The three selected models together address the principal damage mechanisms governing the structural integrity of hydrogen-carrying pipelines: static ductility loss, fracture resistance degradation, and fatigue-driven crack propagation. Table 3-9 summarizes the four models, their respective roles within the framework, and the basis for each inclusion or exclusion decision.

Table 3-9 Final Model Selection for OU HEAT Integration

Model	Response predicted	Role in framework	Final integration decision	Basis for decision
RA	Ductility loss	Primary tensile embrittlement indicator	Selected	Directly captures hydrogen-induced ductility loss; predicted RA also serves as an input feature in the FCG model
FT	FT degradation	Crack initiation resistance under hydrogen	Selected	Adds fracture-based integrity assessment capability to the framework
FCG	Fatigue crack growth rate	Cyclic crack propagation behavior	Selected	Captures fatigue-driven hydrogen damage; predictive accuracy enhanced through RA-assisted dual-model architecture
Elongation	Tensile elongation reduction	Secondary ductility descriptor	Not selected	Represents a valuable standalone contribution but overlaps functionally with RA; does not occupy a defined role in ASME B31.12 embrittlement index formulations and adds limited distinct integration value to the framework

CHAPTER 4

FRACTURE MECHANICS-BASED INTEGRITY AND LIFETIME ASSESSMENT

4.1 Overview of Integrity Assessment Framework

The machine-learning models in Chapter 3 provide data-driven predictions of key mechanical properties, including RA, FT, fatigue crack growth rate, and elongation, under hydrogen exposure. While these predictions capture the material-level response to hydrogen, translating them into actionable integrity decisions for an operating pipeline requires a physics-based structural analysis framework. This chapter develops that framework using a fracture mechanics approach grounded in the ASME B31.12 standard and the API 579-1/ASME FFS-1 fitness-for-service guidelines.

Hydrogen pipelines face operational demands that differ fundamentally from those of conventional natural gas systems. Because hydrogen has a comparatively low volumetric energy density, roughly one-third that of natural gas, higher pressures or flow rates are typically required to deliver equivalent energy throughput [108]. These elevated flow conditions produce larger pressure drops and more frequent pressure cycling, with some hydrogen pipeline concepts anticipating up to two full pressure cycles per day. The resulting cyclic loading, combined with the well-documented ability of hydrogen to accelerate fatigue crack propagation in low-alloy carbon steels, creates a scenario in which pre-existing flaws can grow to critical dimensions far more rapidly than they would in inert service [109].

Even with the availability of modern non-destructive testing (NDT) methods, the detection of flaws is constrained by resolution limits, and defects below a certain size threshold can remain undetected after inspection. In addition, manufacturing-related imperfections such as welding defects, inclusions, and surface scratches are virtually unavoidable in real pipeline construction. Under cyclic internal pressure, these imperfections serve as initiation sites for fatigue cracks, which are then exacerbated by the presence of hydrogen [5], [109]. For these reasons, fracture mechanics-based assessment methods have become the established engineering approach for evaluating the structural integrity of hydrogen pipelines and for determining their safe operational lifetimes [5].

The ASME B31.12 standard, formally titled *Hydrogen Piping and Pipelines*, is widely regarded as the benchmark code for the design, construction, and assessment of pipelines carrying pure hydrogen or hydrogen-natural gas blends above 10 percent concentration (ASME, 2019). The standard is applicable to systems operating at pressures up to 21 MPa and temperatures as low as −62°C, and it recommends steels conforming to API 5L PSL 2 specifications in grades ranging from X42 to X120. A central element of the code is its adapted Barlow's formula for determining the pipeline design pressure:

$$P_{design} = \frac{2\sigma YSt}{Do} FETH_f \tag{4-1}$$

where S is the specified minimum yield strength (SMYS), t is the wall thickness, D is the outer diameter, F is the design factor, E is the longitudinal joint factor, T is the temperature derating factor (applied for service above 121°C), and H_f is the material performance factor. The H_f is unique to hydrogen service and accounts for the degradation of steel properties in the presence of gaseous hydrogen. For low-strength steels at moderate pressures, H_f takes a value of 1.0, indicating negligible hydrogen effects on design. However, for higher-strength grades or when operating pressures exceed approximately 6.9 MPa, H_f is reduced to a value as low as 0.542, reflecting the increased susceptibility to hydrogen-induced damage [13], [58].

The standard provides two design options for pipelines in hydrogen service. Option A is a prescriptive approach that applies a maximum design factor of 0.5, yielding a conservative design without requiring detailed material testing. Option B permits a higher design factor of up to 0.72 but imposes additional requirements, including fracture mechanics evaluation, enhanced material testing, and compliance with supplementary quality standards. Critically, for any pipeline in which the operating hoop stress exceeds 40 percent of the SMYS, ASME B31.12 mandates a fracture mechanics-based assessment regardless of the design option selected. This assessment draws on the procedures described in Article KD-10 of ASME BPVC-VIII-3, with reference to the fracture mechanics provisions in API 579-1/ASME FFS-1 [13].

The API 579-1/ASME FFS-1 standard, commonly referred to as the Fitness-for-Service (FFS) standard, provides a comprehensive, multi-disciplinary framework for evaluating the structural integrity of in-service pressure equipment containing flaws or damage [110]. Although originally developed for the refining and petrochemical industries, its scope has since expanded to include pipelines and other pressurized systems. The standard offers tiered assessment levels: Level 1 and Level 2 assessments use simplified analytical procedures suitable for routine evaluations, while Level 3 assessments employ advanced methods such as finite element analysis and detailed fracture mechanics modeling. For hydrogen pipeline applications, the stress intensity factor solutions and failure assessment diagram (FAD) procedures from Part 9 of API 579-1 are particularly relevant, as they provide the analytical basis for evaluating crack-like flaws under the combined influence of pressure loading and hydrogen-assisted degradation [4].

For pipelines with diameters exceeding 114.3 mm, ASME B31.12 further requires Charpy impact testing in accordance with API 5L Annex G, conducted at specified temperatures to confirm the material's resistance to brittle fracture under hydrogen-affected conditions. Table 4.1 summarizes the key testing requirements and material property specifications mandated by the standard.

Table 4-1 Testing Requirements and Material Property Specifications according to [111]

Material property	ASME B31.12
Threshold Stress Intensity for Hydrogen Assisted Cracking (K_{IH})	- Article: KD-1040. - Standards: ASTM E1681. - Tests: 3 tests each on base material, weld material, and HAZ (total of 9). Tests conducted in TL (LT) direction as per ASTM E399. - Additional Requirements: Minimum value from 3 transverse tensile tests used for assessment (in accordance with SA-370). Yield strength used for constraint check in KD-1045(d). - Condition: $p = p_{design}$ - Required Value: $K_{IH} > 55$ MPa$\sqrt{m}$ - Applicable Literature Data: Not allowed.
Plane Strain Fracture Toughness (K_{IC})	- Articles: KD-1021, referencing KM-250 and KD-4. -Standards: ASTM E399 and E1820. -Tests: Minimum values and number of tests are specified by the designer.
Fatigue Crack Growth Curves (da/dN)	- Article: KD-1050. - Standard: ASTM E647. - Tests: 3 tests each on base material, weld material, and HAZ in the TL (LT) direction as per ASTM E399. Upper bound data used for assessment. - Conditions: $p = p_{design}$; $R = R_{design}$; $f \leq 0.1$ Hz

The fracture mechanics-based integrity assessment developed in this chapter follows the general workflow prescribed by ASME B31.12 and API 579-1/ASME FFS-1. The process begins in

Section 4.2 by defining the crack geometry and loading conditions, then calculates stress intensity factors using solutions appropriate for cylindrical geometries in Section 4.3. The fatigue crack growth formulation, including the standard's hydrogen-specific three-region crack growth law, is established in Section 4.4. Failure and termination criteria are defined in Section 4.5 based on both the critical crack size and the hydrogen-assisted cracking thresholds. Finally, these components are integrated into a cycle-by-cycle lifetime prediction procedure in Section 4.6 that simulates crack propagation from an initial flaw to failure, yielding the predicted number of allowable loading cycles for a given pipeline configuration.

4.2 Crack Geometry and Loading Conditions

The fracture mechanics assessment of a hydrogen pipeline begins with a clear definition of the assumed flaw geometry and the loading conditions to which it is subjected. These two inputs determine how the stress field interacts with a pre-existing defect and ultimately govern the rate at which that defect propagates under service conditions. ASME B31.12, in conjunction with API 579-1/ASME FFS-1, prescribes specific assumptions for both the crack geometry and the loading scenario, and these assumptions form the foundation of the analytical framework developed in this chapter.

4.2.1 Assumed Crack Geometry

ASME B31.12 adopts a conservative reference geometry for fracture mechanics evaluation, in which a single crack is assumed to exist on the inner wall of the pipe, oriented along the pipe's longitudinal (axial) direction, and shaped as a semi-elliptical surface flaw. This configuration is selected because an axially oriented crack on the inner surface represents the most damaging orientation for a thin-walled cylindrical pressure vessel under internal pressure, as the hoop stress acts perpendicular to the crack plane and provides the maximum driving force for crack opening [13], [112]. The inner-surface location is also conservative because it places the crack in direct contact with the hydrogen-bearing gas stream, ensuring that hydrogen can readily diffuse into the highly stressed region surrounding the crack tip.

The pipe is characterized by two principal dimensions: the inner radius, ri, and the wall thickness, t. The crack is described by two additional parameters: the crack depth, a, measured radially inward from the inner pipe surface, and the surface crack length, 2c, measured along the pipe's longitudinal direction. The ratio a/c, known as the aspect ratio, defines the shape of the semi-elliptical flaw, while the ratio a/t indicates how deeply the crack penetrates the pipe wall relative to its total thickness. Figure 4.1 illustrates this assumed crack configuration, as adopted in ASME B31.12 and API 579-1/ASME FFS-1.

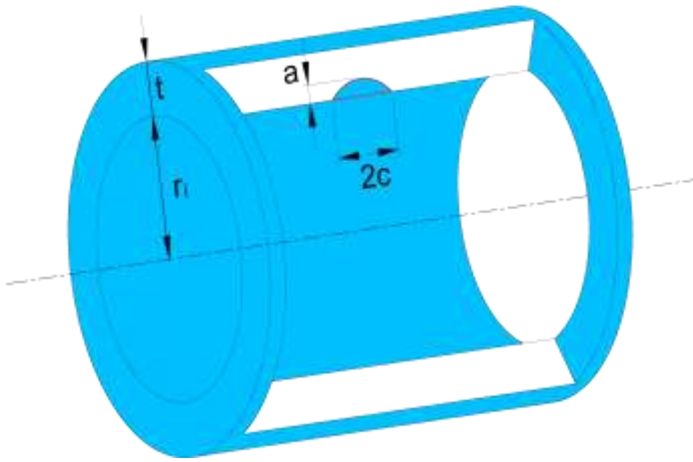

Figure 4-1 Assumed Crack Geometry in ASME B31.12, Showing an Axially Oriented, Semi-Elliptical Surface Crack Located on the Inner Wall of the Pipe (Adapted from [13])

For an accurate fracture mechanics assessment, several secondary effects associated with this geometry must also be considered. Internal pressure acts not only on the pipe bore but also on the exposed faces of the crack, generating an additional opening force known as crack-face pressure loading. In addition, the curvature of the pipe wall and the local compliance of the cracked region can produce a slight outward bulge near the flaw, thereby modifying the local stress distribution. Both effects are accounted for in the stress intensity factor solutions presented in Section 4.3.

4.2.2 Initial Crack Size

ASME B31.12 does not prescribe a specific value for the initial crack depth, a_0. Instead, the standard requires that the size of the starting flaw be established through suitable non-destructive testing (NDT) methods such as ultrasonic, radiographic, or magnetic flux leakage inspection. This approach allows the assessment to be tailored to the actual condition of the pipeline being evaluated, but it also means that the result of the integrity calculation is highly sensitive to the resolution and reliability of the inspection technique used. In practice, the smallest flaw reliably detected by current inline inspection tools is typically on the order of a few percent of the wall thickness, and any defect smaller than this threshold must be assumed to go undetected [5], [13]. Although the absolute initial crack depth is not specified, ASME B31.12 specifies the initial aspect ratio of the assumed flaw as $a_0/c_0 = 2/3$. Once the crack depth a_0 has been determined from inspection data, the initial surface crack length is therefore obtained as:

$$C_0 = \frac{3}{2} \ x \ a_0 \tag{4-2}$$

This fixed aspect ratio simplifies assessment by reducing the initial flaw description to a single parameter while preserving a realistic, semi-elliptical shape consistent with the types of flaws typically observed in service. As the crack grows under cyclic loading, both a and c increase, and the aspect ratio evolves over the pipeline's lifetime.

4.2.3 Loading Conditions

The loading scenario considered in ASME B31.12 for hydrogen pipelines is dominated by cyclic internal pressure variations. During normal operation, the pressure inside a hydrogen pipeline fluctuates between a minimum, P_{min}, and a maximum, P_{max}, in response to changes in supply and demand at consumption nodes along the network. As noted in Section 4.1, hydrogen pipelines may experience up to two full pressure cycles per day, which is considerably more frequent than the loading typically experienced by natural gas transmission lines [108]. Each pressure cycle imposes a corresponding mechanical stress cycle on the pipe wall and any pre-existing defect, driving incremental fatigue crack growth. For a thin-walled cylindrical pressure vessel under internal pressure, the dominant stress component is the circumferential, or hoop, stress, σ_h, given by the standard relation:

$$\sigma_h = \frac{P \ X \ D}{2t} \tag{4-3}$$

where P is the internal pressure, D is the outer diameter of the pipe, and t is the wall thickness. The hoop stress acts in the circumferential direction, perpendicular to the plane of an axially oriented crack, and is therefore the principal driving force for the propagation of the assumed flaw. As the pressure cycles between P_{min} and P_{max}, the hoop stress likewise cycles between $\sigma_{h,min}$ and $\sigma_{h,max,}$ producing the fluctuating stress field that controls fatigue crack advance. A useful descriptor of the load severity is the ratio (also known as stress ratio), defined as:

$$R\sigma = \frac{\sigma min}{\sigma max} = \frac{Pmin}{Pmax} \tag{4-4}$$

The load ratio quantifies the relative magnitudes of the minimum and maximum stresses within each cycle and strongly influences the fatigue crack growth rate. A higher $R\sigma$ corresponds to a smaller stress range for a given maximum stress, resulting in a slower crack propagation rate, whereas a lower value indicates more severe cycling. ASME B31.12 limits the applicability of its conservative fatigue crack growth law (discussed in section 4.4) to load ratios of $R\sigma \leq 0.5$, which encompasses the operational range expected for most hydrogen transmission systems [13].

In the lifetime model developed in this chapter, secondary loading sources such as residual stresses from welding, bending stresses from soil settlement, and thermal stresses are assumed to be negligible relative to the cyclic pressure-induced hoop stress. This assumption is consistent with the approach adopted by ASME B31.12 for design-stage assessments and is justified for buried straight-run pipelines operating under steady environmental conditions. For pipelines subject to significant secondary loading, such as those in seismically active regions or those with substantial geometric discontinuities, these additional stress components would need to be incorporated into the stress intensity factor calculations described in the next section.

4.3 Stress Intensity Factor Models

The stress intensity factor (SIF) is the central parameter of linear elastic fracture mechanics (LEFM) and provides the quantitative link between the remote loading applied to a cracked component and the local stress field that develops at the crack tip. Originally formulated by Irwin in the 1950s, the SIF characterizes the strength of the crack-tip singularity for a body that remains predominantly elastic, and its magnitude alone is sufficient to predict whether a crack of a given size will propagate under a given load [112]. For the operating conditions and crack sizes of interest in hydrogen pipeline integrity assessment, the cracked region remains within the small-scale yielding regime, and the LEFM-based SIF approach is therefore the appropriate analytical framework. It is also the framework explicitly mandated by both ASME B31.12 and API 579-1/ASME FFS-1 for hydrogen pipeline evaluations [110], [111].

For the assumed flaw geometry described in Section 4.2, the dominant fracture mode is Mode I, in which the crack faces are pulled directly apart by the hoop stress acting normal to the crack plane. The corresponding stress intensity factor is denoted KI, and for compactness it is referred to simply as K throughout the remainder of this chapter. Because the loading in service is cyclic rather than monotonic, both the maximum value of the stress intensity factor during a load cycle, K_{max}, and its minimum value, K_{min}, must be evaluated. The difference between these two quantities defines the stress intensity factor range:

$$\Delta K = K_{max} - K_{min} \tag{4-5}$$

Which is the principal driving force in fatigue crack growth analysis and serves as the input to the crack growth law developed in Section 4.4 [113]. For a semi-elliptical surface flaw of the type assumed in this work, the magnitude of ΔK varies along the crack front, and the assessment must therefore evaluate the SIF at two characteristic locations: the deepest point of the crack, corresponding to the parametric angle $\varphi = 90°$, and the surface points where the crack intersects the inner pipe wall, corresponding to $\varphi = 0°$. The crack depth direction generally controls the radial growth of the flaw, while the surface direction governs its longitudinal extension; tracking both is necessary to capture the evolution of the aspect ratio over the pipeline's lifetime [114].

4.3.1 Choice of Stress Intensity Factor Solution

API 579-1/ASME FFS-1 provides a catalog of validated SIF solutions in Annex 9B, each tailored to a specific combination of component geometry, crack shape, crack orientation, and loading mode (API, 2016). For a cylindrical pressure vessel containing an axial flaw on the inner surface, several candidate solutions are available, including those for surface-cracked plates with semi-elliptical flaws (commonly designated KPSE-type solutions) and those for cylinders containing through-wall cracks oriented along the longitudinal axis (designated KCTCL solutions). Plate-based solutions are mathematically simpler and are sometimes invoked when the pipe-to-thickness ratio is large enough that wall curvature is assumed negligible. However, they implicitly ignore the bulging amplification that arises when a crack in a curved shell is subjected to internal pressure. By contrast, cylinder-based solutions retain the influence of pipe curvature explicitly through a Folias-type bulging correction and therefore yield SIF values that more faithfully represent the actual stress field around an axial flaw in a thin-walled pipe [113], [115], [116].

In the lifetime model developed in this work, the cylinder through-wall crack solution for the longitudinal direction (KCTCL) from Annex 9B of API 579-1/ASME FFS-1 was adopted. This selection departs from the approach taken by Oesterlin et al. [13], who applied the surface-cracked plate solution with a semi-elliptical flaw (KPSE1) from the same annex in their hydrogen pipeline assessment under ASME B31.12. The KPSE1 solution treats the cracked region as a flat plate under through-wall membrane and bending stress and is mathematically convenient, but it does not retain the curvature of the pipe wall within the SIF calculation itself. The KCTCL solution, by contrast, captures the curvature-induced bulging of the cracked cylinder directly through its influence coefficients, and is therefore expected to provide a more representative description of the stress field around an axial flaw in a thin-walled pressurized pipe.

The implications of this choice for the predicted lifetime, including a direct numerical comparison with the KPSE1-based result reported by Oesterlin et al. [13], are examined in Chapter 5. The KCTCL solution accounts for through-wall membrane stress, through-wall bending stress, and the additional contribution from internal pressure acting on the exposed crack faces, all of which are relevant to a pipe under cyclic pressurization. The component geometry and the orientation of the through-wall crack assumed by this solution are illustrated in Figure 4.2 for the longitudinal direction. For completeness, the corresponding circumferential direction solution, which is provided in Annex 9B as a companion solution, is shown in Figure 4.3. Although the present work uses only the longitudinal solution, both geometries are presented here because the longitudinal and circumferential SIF formulations share the same general structure and the same family of influence coefficients, and the comparison clarifies the orientation conventions adopted by the standard.

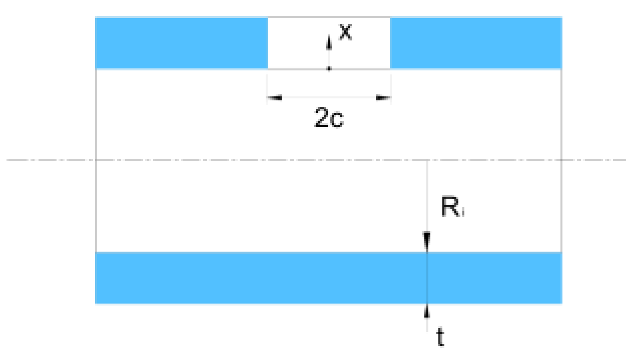

Figure 4-2 Through-Wall Crack of a Cylinder, Longitudinal Direction, as Adopted in Annex 9B of API 579-1/ASME FFS-1 (Adapted from [13])

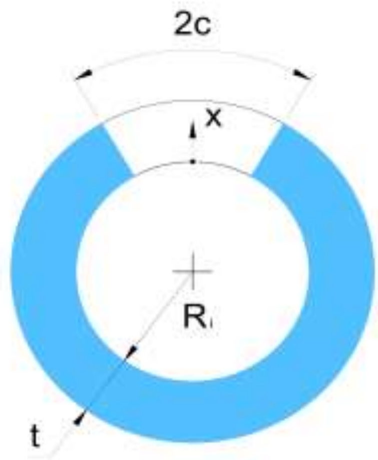

Figure 4-3 Through-Wall Crack of a Cylinder, Circumferential Direction, as Provided in Annex 9B of API 579-1/ASME FFS-1 (Adapted from [13])

4.3.2 Stress Intensity Factor for Internal Pressure with Crack Face Loading

For an internally pressurized cylinder containing a longitudinal through-wall crack, with crack face pressure loading included, the Mode I stress intensity factor is expressed in the form:

$$KI = \frac{PR_0}{t} G_p \sqrt{\pi c} \tag{4-6}$$

Where P is the internal pressure, Ro is the outer radius of the pipe, t is the wall thickness, c is the half-length of the surface crack, and G_p is a dimensionless influence coefficient that depends on the pipe geometry and on the location along the crack front being evaluated. The prefactor ($\frac{PRo}{t}$) is recognizable as the thin-wall hoop stress acting on the pipe wall, and Equation (4.6) can therefore be read as the conventional $\sqrt{(\pi c)}$ crack-driving expression scaled by the geometry-dependent factor G_p. In this formulation, the entire influence of the cracked-cylinder geometry, including bulging, finite wall thickness, and the contribution of internal pressure acting on the exposed crack faces, is absorbed into the single coefficient G_p. The companion coefficients G_0 and G_1 reported in Annex 9B correspond to remote membrane and bending stress contributions and are retained in the implementation for generality, but for the pure-internal-pressure case considered here the G_p term is the controlling contribution.

The influence coefficients G_0, G_1, and G_p are functions of the pipe geometry and are computed from a rational polynomial expression of the form:

$$G_{0,1,p} = \frac{A_0 + A_1\lambda + A_2\lambda^2 + A_3\lambda^3}{1 + A_4\lambda + A_5\lambda^2 + A_6\lambda^3} \tag{4-7}$$

Where the constants A_0 through A_6 are tabulated in Tables 9B.6 and 9B.7 of API 579-1/ASME FFS-1 (API, 2016). Two distinct sets of constants are provided in these tables: one for evaluation on the inside surface of the cylinder and a second for evaluation on the outside surface, allowing K to be computed at either location. In this work the SIF is evaluated on the inside surface, consistent with the assumption from Section 4.2.1 that the reference flaw originates on the bore of the pipe in direct contact with the hydrogen-bearing gas stream.

The dimensionless parameter λ that appears in Equation (4.7) encodes the geometry of the cracked cylinder and is defined by:

$$\lambda = \frac{1.818c}{\sqrt{R_i t}} \tag{4-8}$$

where R_i is the inner radius of the pipe, t is the wall thickness, and c is again the half-length of the surface crack. The form of Equation (4.8) reflects the Folias bulging factor that arises in shell theory for axial cracks in pressurized cylinders, in which the quantity $\sqrt{(R_i t)}$ sets the characteristic length scale over which curvature effects become significant relative to the in-plane crack size [115]. As λ increases, the bulging amplification grows, the influence coefficients depart progressively from their flat-plate limits, and the cylinder-based solution diverges from any equivalent plate-based estimate. This is the central reason that the KCTCL solution was preferred over the surface-cracked plate alternatives for the present hydrogen pipeline application.

4.3.3 Net Section Membrane Stress Including Axial Force

API 579-1/ASME FFS-1 also provides a stress definition that allows the net section membrane stress acting across the cracked plane to be computed when both internal pressure and an externally applied axial force are present. For a thick-walled cylinder of inner radius R_i and outer radius R_o subjected to an internal pressure p and a net axial force F, the membrane stress is expressed as:

$$\sigma_m = \frac{pR_i^2}{R_o^2 - R_i^2} + \frac{F}{\pi\left(R_o^2 - R_i^2\right)} \tag{4-9}$$

The first term on the right-hand side of Equation (4.9) corresponds to the longitudinal stress generated by the internal pressure acting on the closed ends of the cylindrical pressure vessel, while the second term is the direct membrane contribution of any external axial force redistributed over the net cross-sectional area of the pipe wall. For the buried straight-run pipelines considered in this study, the axial force F is taken as zero, and Equation (4.9) reduces to the pressure-only end-cap stress. The expression is retained here in its full form to preserve fidelity with the API 579-1/ASME FFS-1 procedure and to keep the model extensible to configurations in which axial loading becomes significant, such as pipelines crossing geologically active terrain or those subject to large thermal end-restraint forces.

4.4 Fatigue Crack Growth Formulation

The stress intensity factor range, ΔK, defined in Section 4.3 quantifies the cyclic driving force acting on the crack tip during each load cycle, but it does not by itself determine how much the crack actually advances. The link between the driving force and the physical increment of crack growth is provided by an empirical fatigue crack growth law of the general form $da/dN = f(\Delta K)$, where a is the crack depth and N is the cumulative number of applied load cycles. Together with the FT, the fatigue crack growth relation forms the experimental backbone of any fracture-mechanics-based lifetime assessment, because it is the relation through which ΔK is translated into an incremental crack advance during the cycle-by-cycle simulation [111], [113].

ASME B31.12 requires that fatigue crack growth curves be determined experimentally in accordance with ASME BPVC-III-3 Article KD-10 for each combination of material and material state of interest. When experimental data are not available, the standard provides a conservative default curve for hydrogen service in the form of a three-region power-law expression fitted to published fatigue data on API 5L X52, X70, and comparable grades [46], [117], [118], [119]. This default curve is constructed to bound the experimental scatter across the regimes in which hydrogen-assisted acceleration is pronounced, and its use in a lifetime assessment is nevertheless subject to several explicit restrictions imposed by ASME B31.12. The hydrogen gas pressure must not exceed 20 MPa, the load ratio must satisfy $R \leq 0.5$, the phosphorus content of the pipeline material must remain below 0.015 weight percent, the ultimate tensile strength of both the base metal and the weld metal must not exceed 758 MPa, and the specified minimum yield strength must be below 550 MPa. Outside of these bounds the underlying experimental basis no longer supports the extrapolation and the default curve cannot legitimately be invoked. These restrictions are themselves a significant motivation for pursuing a broader, data-driven alternative to the standard curve.

This study utilizes the fatigue crack growth law applied inside the lifetime simulation is the ML fatigue crack growth model discussed in section 3.4. The developed model returns da/dN for a given set of inputs that include ΔK together with the material and loading descriptors identified during its training. Within the framework of this chapter, the model is treated as the source of da/dN for each cycle: once ΔK has been computed from the stress intensity factor formulation of Section 4.3, the corresponding crack advance is obtained from the Section 3.4 model and used to update the flaw dimensions in the next iteration.

4.5 Failure and Termination Criteria

The cycle-by-cycle simulation developed for the lifetime assessment advances the flaw incrementally under the driving force computed from Section 4.3 and the crack growth response supplied by the machine-learning model of Section 3.4. For the simulation to yield a meaningful lifetime estimate, however, it must also be provided with a well-defined set of conditions under which the crack is considered to have reached an unacceptable state and the iteration is terminated. ASME B31.12, in conjunction with API 579-1/ASME FFS-1 and ASME BPVC-VIII-3, defines three such conditions that together constitute the failure and termination framework of the assessment: a limit on the physical size of the flaw, a specified mechanical property of the pipeline steel that serves as a reference for stress-based checks, and a threshold value of the stress intensity factor below which hydrogen-assisted cracking is considered inactive. The present section develops each of these conditions in turn and explains how they are implemented in the lifetime simulation.

4.5.1 Critical Crack Size

The critical crack size defines the flaw dimensions at which continued operation of the pipeline can no longer be justified on fracture-mechanics grounds and therefore marks one of the natural termination points of the cycle-by-cycle simulation. ASME B31.12 offers two alternative routes for establishing this limit. The first is a simple geometric rule in which the critical crack depth is taken as a fixed fraction of the wall thickness, and the second is a more elaborate procedure based on the failure assessment diagram (FAD) provided in API 579-1/ASME FFS-1. Under the geometric rule, the critical crack depth, a_{crit}, and the corresponding critical surface length, $l_{crit,}$ are defined directly in terms of the pipe wall thickness, t:

$$a_{crit} = 0.25t \tag{4-10}$$

$$l_{crit} = 2c_{crit} \tag{4-11}$$

This prescription places the critical crack at a quarter of the wall thickness and fixes the surface length at one and a half times the thickness, consistent with the initial aspect ratio assumption a/c = 2/3 adopted in Section 4.2.2. The rule is intentionally conservative and has the advantage of requiring no additional material-specific inputs, which is why it is the form most often invoked for routine design-stage assessments [13], [110].

As an alternative, Article KD-10 of ASME BPVC-VIII-3, through its reference to Article KD-401(c), permits the critical crack size to be determined from a Level 2 or Level 3 failure assessment diagram in accordance with Part 9 of API 579-1/ASME FFS-1 [110]. Under this approach, the critical state is identified as the point at which the combined fracture and plastic-collapse loadings on a cracked component lie on the FAD limiting curve, yielding a material-specific critical size that accounts simultaneously for brittle fracture and net-section yielding [113]. The FAD-based route is more precise but also more demanding, requiring accurate values of the FT and the material's yield stress, as well as the appropriate reference stress solution for the geometry under assessment. In this study, the simpler geometric rule of Equations (4.10) and (4.11) is adopted for the baseline lifetime calculations. This choice keeps the assessment framework self-contained within the parameters already defined in Sections 4.2 and 4.3, and it matches the convention used by [13] in the ASME B31.12 assessment against which this work's results are later compared. The FAD-based route is retained as a documented alternative that can be activated in future model extensions for cases where a tighter, material-specific critical size estimate is required.

4.5.2 Yield Strength

The yield strength of the pipeline steel is incorporated into the assessment framework in several ways. It defines the specified minimum yield strength (SMYS) used in the hoop stress limit of 40 percent SMYS that triggers the fracture mechanics evaluation under ASME B31.12, it sets the reference for the constraint check in Article KD-1045(d) that accompanies the threshold stress intensity measurement discussed in Section 4.5.3, and it provides the flow stress baseline for any future FAD-based critical crack size evaluation of the type referenced in the previous subsection. For all of these purposes, ASME B31.12 prescribes that the yield strength value used in the assessment be the undegraded yield strength of the steel, determined from conventional tensile testing in air and without any adjustment for hydrogen exposure [13], [110].

The rationale for this convention rests on the observation that hydrogen exerts its damaging influence on pipeline steels primarily through degradation of FT and acceleration of fatigue crack growth, rather than through a direct reduction of the macroscopic yield strength. Dedicated experimental studies of hydrogen-charged and hydrogen-exposed carbon steels have consistently reported that yield strength is only weakly affected by hydrogen at the pressures and compositions of interest to transmission service, even as ductility, reduction of area, and fracture-related properties decline substantially [13], [27]. Within the overall assessment framework, the effects of hydrogen are therefore carried by the fatigue crack growth model of Section 3.4 and by the strength intensity threshold discussed in the next subsection, rather than by a modified yield strength. Any additional conservatism required in the assessment is applied through the safety factors and the allowable-cycle rules of Section 4.6 rather than by artificially reducing the yield strength input. In the lifetime simulation developed, the yield strength of the modeled API pipeline steel materials is therefore taken directly from air tested tensile measurements on the base material.

4.5.3 Threshold Stress Intensity for Hydrogen-Assisted Cracking

The threshold stress intensity factor for hydrogen-assisted cracking, denoted KIH, is the value of the Mode I stress intensity factor below which a pre-existing crack in a hydrogen-exposed steel is considered to remain arrested and above which it is susceptible to sustained hydrogen-assisted propagation. In the assessment framework of ASME B31.12, KIH plays two distinct but complementary roles, and both are exploited in the lifetime simulation developed.

The first role is as a material qualification criterion. For a steel to be eligible for use in a hydrogen pipeline evaluated under ASME B31.12, its threshold stress intensity for hydrogen-assisted cracking must satisfy the requirement KIH $\geq$ 55 MPa$\sqrt{m}$, and this value must be verified through dedicated testing in accordance with ASME BPVC-VIII-3 Article KD-10 and ASTM E1681. The required test program is described in Table 4-1: three tests each on the base material, the weld material, and the heat-affected zone, giving a total of nine tests, conducted in the TL (or LT) orientation on pressure-charged specimens at the design pressure of the pipeline. The minimum value obtained across the three transverse tensile tests is taken as the qualification KIH for the assessment, in accordance with SA-370, and the yield strength constraint check of KD-1045(d) must also be satisfied [13], [111].

The second role of KIH is as an upper bound on the stress intensity factor permitted during operation, and hence as one of the termination conditions of the cycle-by-cycle simulation. As the crack grows under repeated pressure cycling, the maximum stress intensity factor K_{max}, computed from Equation (4.6) at the peak of each cycle increases monotonically with the crack dimensions. Once K_{max} reaches the qualification value K_{IH}, the operating condition of the pipeline is considered to have entered the regime of active hydrogen-assisted cracking, and continued cyclic loading under that condition is no longer defensible. The simulation therefore terminates when either the crack depth a exceeds the critical crack size a_{crit} defined in Section 4.5.1, or the computed K_{max} reaches or exceeds K_{IH}, whichever occurs first. In practice, the dominant termination mechanism depends on the combination of pipe geometry, operating pressure range, and initial flaw size considered in a given run of the model, and both termination conditions must be checked at every iteration of the simulation loop.

The K_{IH} threshold therefore acts as an explicit coupling between the material qualification stage of the assessment and the lifetime calculation itself. It establishes the eligibility of a given steel for hydrogen service, and it simultaneously caps the stress intensity history that steel may experience in operation. Together with the critical crack size of Section 4.5.1 and the yield strength of Section 4.5.2, it completes the set of failure-related inputs required by the cycle-by-cycle lifetime procedure developed in Section 4.6.

4.6 Lifetime Prediction Procedure

The preceding sections of this chapter have established the components required to assess the structural integrity of a hydrogen pipeline under cyclic loading: crack geometry and loading conditions (Section 4.2), the stress intensity factor formulation (Section 4.3), the fatigue crack growth model (Section 4.4), and the failure and termination criteria (Section 4.5). The present section integrates these components into a complete lifetime prediction procedure that simulates the progressive growth of an initial flaw under repeated pressure cycling until one of the defined termination conditions is met. The procedure follows the general methodology prescribed by ASME B31.12 and ASME BPVC-VIII-3 Article KD-10, with the machine-learning fatigue crack growth model of Section 3.4 replacing the standard empirical curve as the source of da/dN in the simulation loop.

4.6.1 Design Lifetime and Allowable Number of Loading Cycles

Before a cycle-by-cycle simulation can be used for design, the rules for translating the raw simulation output into an allowable design lifetime must be specified. ASME BPVC-VIII-3 Article KD-412 provides two options for this purpose, and the design lifetime is governed by whichever option yields the lower number of allowable loading cycles.

Option 1 defines the design lifetime N_d as one half of the number of cycles required for the crack to reach either the critical crack size a_{crit} or the threshold stress intensity K_{IH}, whichever is encountered first:

$$N_d = N_{crit} / 2 \tag{4-12}$$

where N_{crit} is the number of cycles at which the simulation terminates due to either $a \geq a_{crit}$ or $K_{max} \geq K_{IH}$. The critical crack size a_{crit} is determined as per Article KD-401(c) of ASME BPVC-VIII-3 and is validated using the failure assessment diagram procedure in API 579-1/ASME FFS-1 when the FAD-based route is selected. The factor of two provides an explicit safety margin between the predicted failure life and the permitted operating life.

Option 2 establishes the design lifetime using two alternative allowable crack-depth conditions, and the final allowable number of cycles is taken as the minimum of the two. The first condition (designated condition (a) under Article KD-412.1) limits the allowable crack depth for monobloc vessels to a maximum of 25 percent of the wall thickness:

$$a_{allow} = 0.25t \tag{4-13}$$

and N_{allow} is defined as the number of cycles at which the crack depth first reaches this value. The second condition (designated condition (b) under Article KD-412.1) defines the allowable crack depth as:

$$a_{allow} = a_0 + 0.25(a_{crit} - a_0) \tag{4-14}$$

where a_0 is the initial crack depth from Section 4.2.2, and a_{crit} is the critical crack size from Section 4.5.1. Under this condition, the crack is permitted to grow by no more than one quarter of the distance between its starting size and the critical size. The allowable number of cycles under Option 2 is then the minimum of N_{allow} from condition (a) and N_{crit} from condition (b) evaluated at the corresponding a_{allow}. The design lifetime for the pipeline is the lower of the values returned by Option 1 and Option 2. In either case, the calculation depends on first running the full cycle-by-cycle simulation to obtain N_{crit}, after which the design rules are applied as a post-processing step. The simulation procedure itself is described in the next subsection.

4.6.2 Cycle-by-Cycle Simulation Workflow

The lifetime prediction is carried out through a sequential, cycle-by-cycle simulation of crack growth under the hydrogen pipeline operating conditions defined in Section 4.2.3. The procedure follows a fixed sequence of calculations at each iteration, with the crack geometry updated incrementally after every cycle and two termination checks evaluated before the next cycle begins. The complete workflow is illustrated in Figure 4-4 and is described step by step in the paragraphs that follow.

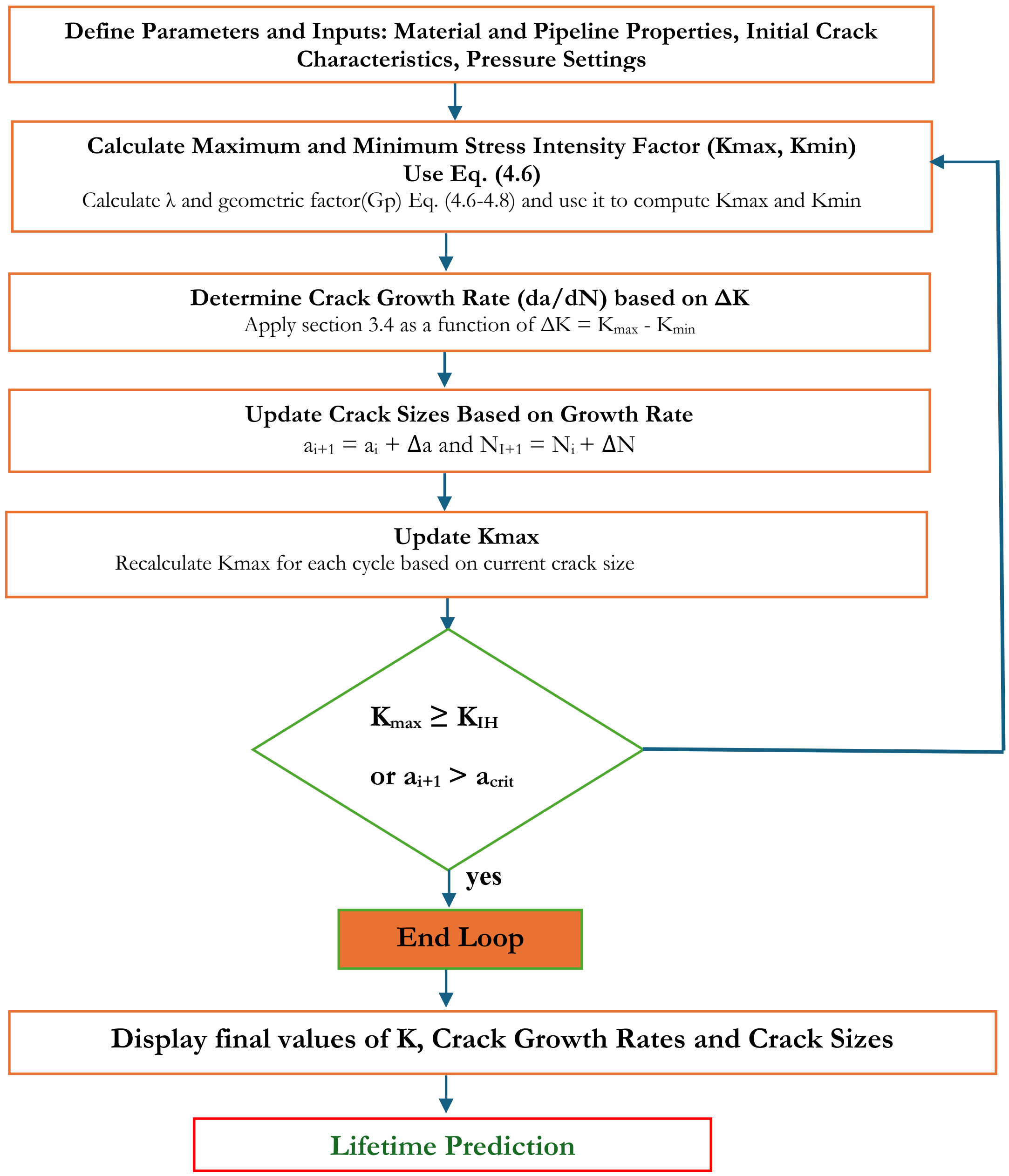

Figure 4-4 Cycle-by-Cycle Lifetime Prediction Workflow for the Fracture Mechanics-Based Integrity Assessment

The simulation begins with the definition of all required input parameters. These include the material properties of the pipeline steel (yield strength and ultimate tensile strength from air-tested measurements, and the threshold stress intensity K_{IH} from hydrogen-environment testing as described in Section 4.5), the pipeline dimensions (outer diameter D_0 and wall thickness t), the initial crack characteristics (initial depth a_0 and initial surface half-length c_0, related by the aspect ratio $a_0/c_0 = 2/3$ from Section 4.2.2), and the operating pressure settings (maximum pressure P_{max} and minimum pressure P_{min}).

With all inputs defined, the simulation enters the iterative loop. At the start of each cycle i, the geometric parameter, λ, is computed from the current crack half-length C_i and the pipe dimensions using Equation (4.8), and the corresponding influence coefficient G_p is evaluated from Equation (4.7) using the tabulated constants from API 579-1/ASME FFS-1. The maximum and minimum stress intensity factors K_{max} and K_{min} are then calculated by substituting P_{max} and P_{min}, respectively, into the stress intensity factor expression of Equation (4.6), together with the current value of G_p and the current crack half-length C_i. The stress intensity factor range for the cycle is obtained as $\Delta K = K_{max} - K_{min}$ in accordance with Equation (4.5). The computed ΔK, together with the material and loading descriptors required by the machine-learning fatigue crack growth model of Section 3.4, is then passed to that model to obtain the crack growth rate da/dN for the current cycle. With this growth rate determined, the crack dimensions are updated for the next cycle according to:

$$a_{i+1} = a_i + \Delta a \tag{4-15}$$

$$N_{i+1} = N_i + \Delta N \tag{4-16}$$

where Δa is the crack depth increment computed from da/dN and ΔN is the corresponding cycle increment. Once the crack dimensions have been updated, K_{max} is recalculated for the new crack geometry to reflect the increased severity of the stress state at the growing crack tip.

At this point the two termination conditions from Section 4.5 are evaluated. The simulation checks whether K_{max} has reached or exceeded the threshold stress intensity K_{IH}, and whether the updated crack depth a_{i+1} has exceeded the critical crack size a_{crit}. If either condition is satisfied, the loop terminates and the simulation records the final values of the stress intensity factors, the crack growth rates, and the crack dimensions at the point of termination. The total number of elapsed cycles at termination constitutes N_{crit}, which is then processed through the design lifetime rules of Section 4.6.1 to obtain the allowable number of loading cycles for the pipeline. If neither termination condition is met, the simulation returns to the start of the loop and proceeds to the next cycle.

This iterative, incremental procedure ensures that the evolving crack geometry is accounted for at every step of the simulation, so that the progressive increase in K_{max} as the flaw grows, and the corresponding acceleration of the crack growth rate, are captured in a physically consistent manner throughout the predicted lifetime of the pipeline.

4.6.3 Summary of the Fracture Mechanics Assessment Framework

Table 4-2 consolidates the principal elements of the fracture mechanics-based assessment framework developed in this chapter. Each row of the table identifies a key element of the assessment, together with its source within the governing standards and the treatment adopted in the present work. The table is intended as a single-point reference that allows the reader to trace every component of the lifetime prediction procedure back to its regulatory basis.

Table 4-2 Summary of Fracture Mechanics Assessment Parameters Adopted in this Study

Assessment Element	Standard Reference	Treatment in this Work
Crack geometry	Axially oriented, semi-elliptical crack in a cylinder	As prescribed; inner-surface flaw per Section 4.2.1
Initial aspect ratio (a_0/c_0)	2/3	As prescribed; per Section 4.2.2
Initial crack depth (a_0)	To be identified using suitable NDT methods	Input parameter; varied in parametric studies
Initial surface crack length (c_0)	Defined by the ratio a_0/c_0	Computed from a_0 per Equation (4.2)
Stress intensity factor (K) solution	API 579-1/ASME FFS-1, Annex 9B	KCTCL solution for longitudinal through-wall crack; per Section 4.3
Critical crack size (a_{crit})	a_{crit} = 0.25t and l_{crit} = 1.5t per ASME B31.12, or from Level 2 FAD of ASME FFS-1 per Article KD-10	Geometric rule adopted; per Section 4.5.1
Fatigue crack growth (da/dN)	Measured experimentally or from ASME B31.12 design curve	ML fatigue crack growth model from Section 3.4
Allowable crack size (a_{allow})	Determined per Article KD-412 of ASME BPVC-VIII-3	Per Section 4.6.1, Option 1 and Option 2
Threshold stress intensity (K_{IH})	≥ 55 MPa$\sqrt{m}$	As prescribed; per Section 4.5.3
Load collectives	Not explicitly defined or regulated in ASME B31.12	Cyclic internal pressure per Section 4.2.3

CHAPTER 5

INTEGRATED TOOL APPLICATION, RESULTS AND DISCUSSION

5.1 Overview of the Integrated Assessment Tool

This chapter presents the University of Oklahoma Hydrogen Embrittlement Assessment Tool (OU HEAT), an integrated computational platform developed to evaluate the structural integrity and remaining fatigue life of steel pipelines operating in hydrogen-blended natural gas environments. OU HEAT unifies the machine-learning property prediction models described in Chapter 3 with the fracture mechanics-based lifetime simulation framework established in Chapter 4 within a single graphical user interface. The tool is designed to serve as a practical screening and decision support resource for pipeline engineers and researchers assessing hydrogen compatibility across a range of API 5L steel grades and operating scenarios. The tool was developed in Python using the PyQt5 framework and is deployed on a dedicated university server accessible at ouheat.sooner.net.ou.edu, where authorized users can interact with the interface remotely through a standard web browser while all computations execute server-side.

The graphical interface is organized into six tabs, each dedicated to a distinct functional area. The Program Input tab, shown in Figure 5.1, serves as the main entry point, where users select a steel grade (X42, X52, X60, X70, X80, or X100), a stress intensity factor model (KCTCL or KCSCLE1), a fatigue crack growth model (CatBoost or XGBoost), and a unit system (SI or US Field). Material composition fields are automatically populated upon grade selection from representative values in the experimental literature, though users can override any value to evaluate custom compositions. Operating condition inputs include minimum and maximum pressure, hydrogen concentration, cyclic loading frequency, oxygen content, and test temperature, while geometric inputs include outer diameter, wall thickness, initial crack depth ratio, and crack aspect ratio. The tool computes derived quantities such as load ratio and average pressure automatically and validates all inputs against the training domain of the ML models before initiating a prediction. The Program Output tab displays the computed results; the Plots tab provides interactive visualization of crack growth behavior; the Sensitivity Analysis tab enables parametric studies; the Comparison tab allows cross-run evaluation of predictions; and the Help tab contains built-in documentation. The output, plotting, and analysis capabilities of these tabs are demonstrated in Sections 5.4 through 5.6.

Once all inputs are specified, the user initiates the simulation by clicking the Begin Prediction button. The tool first uses the selected ML models to predict RA and FT under the given material and environmental conditions. These predicted properties then serve as two of the eighteen input features for the fatigue crack growth model, alongside material composition, hydrogen pressure, and the stress intensity factor range computed at each cycle. The simulation proceeds iteratively: at each step, the stress intensity factor is calculated from the current crack geometry and loading using the selected SIF formulation; the ML fatigue model predicts the crack growth rate; the crack dimensions are updated; and the termination criteria are checked. The simulation terminates when the maximum stress intensity factor reaches the hydrogen-assisted threshold (KIH = 55 MPa√m) or when the crack depth reaches 25% of the wall thickness. A progress indicator is displayed during computation, and a Stop Prediction button allows users to terminate a running simulation at any stage.

The Sensitivity Analysis tab allows the user to select a parameter of interest (hydrogen concentration, initial crack depth, oxygen content, load ratio, yield strength, or temperature), after which the tool automatically constructs a baseline case and two perturbed cases at +/- 25% and executes all three in parallel. Results are overlaid on the same plot for direct visual comparison of how the parameter influences crack growth and lifetime. The Comparison tab stores the results of each completed prediction run and generates bar charts comparing selected output quantities (such as predicted lifetime, FT, or final stress intensity factor) across different steel grades or model configurations. The sections that follow describe the model integration workflow in detail (Section 5.2), define the case study (Section 5.3), present prediction results and validation (Section 5.4), report sensitivity findings (Section 5.5), examine model comparison and robustness (Section 5.6), and discuss the engineering implications (Section 5.7).

Figure 5-1 Program Input tab of the OU HEAT Interface

5.2 Model Integration and Workflow

The integrated prediction workflow in OU HEAT proceeds through three distinct modeling layers: the ML-based prediction of hydrogen-affected material properties (RA and FT), the stress intensity factor computation from applied loading and crack geometry, and the cycle-by-cycle fatigue crack growth simulation that combines the outputs of the first two layers to estimate remaining pipeline lifetime. Figure 5.2 illustrates the complete data flow from user inputs through the three modeling layers to the final assessment outputs.

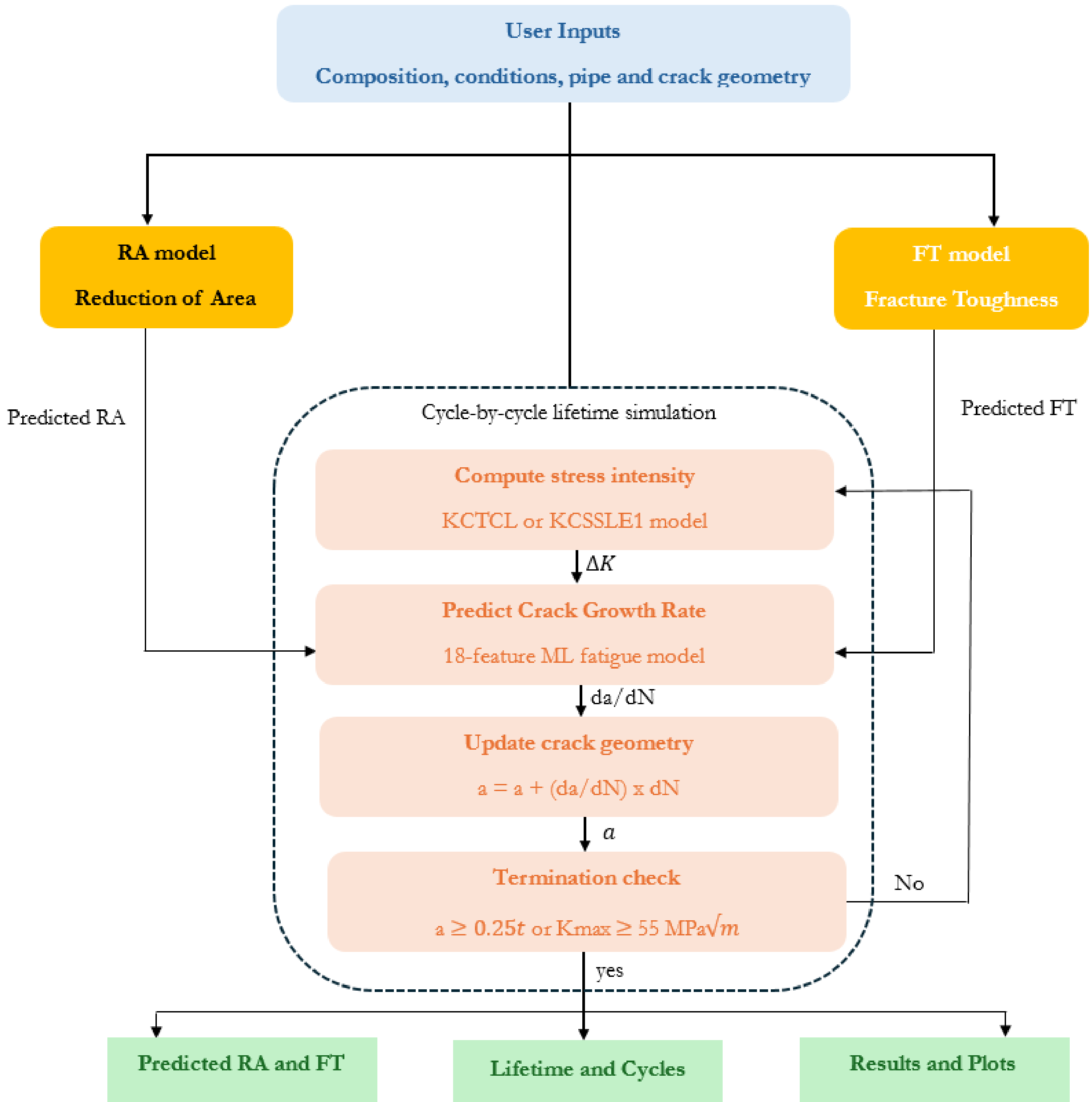

Figure 5-2 Prediction workflow of the OU HEAT tool showing the three modeling layers and cycle-by-cycle simulation loop

When the user clicks Begin Prediction, the tool first collects and converts all user-entered values into a standardized internal representation. Pressures are stored in Pascals, lengths in meters, yield strength in MPa, and temperature in degrees Fahrenheit (the unit used in the original training datasets). The hydrogen partial pressure, which serves as a key input to all three ML models, is derived from the user-specified hydrogen concentration and the average operating pressure as

$$H_2 \text{ Pressure (MPa)} = \frac{\frac{Pmin+Pmax}{2} x \frac{Hydrogen\ concentration}{100}}{1000000} \quad (5\text{-}1)$$

The load ratio R is computed as:

$$R = \frac{Pmin}{Pmax} \quad (5\text{-}2)$$

The first modeling layer executes the property prediction models. The RA model receives twelve input features: the elemental composition values (Fe, C, Mn, P, S, Si, Al, Cr), yield strength, test temperature, hydrogen partial pressure, and oxygen content. The FT model receives a similar feature set with minor differences in feature ordering and labeling, as described in Chapter 3. Depending on the fatigue model selected by the user, the RA and FT predictions are generated by the corresponding base algorithm. If a CatBoost-based fatigue model is selected, the CatBoost RA and FT models are used; if an XGBoost-based fatigue model is selected, the XGBoost RA and FT models are used. The predicted RA and FT values are computed once per prediction run and remain constant throughout the subsequent crack growth simulation, reflecting the assumption that the bulk material properties do not change as the crack propagates.

The second modeling layer is the stress intensity factor computation, which is called at each iteration of the crack growth loop. If the user selects the KCTCL model, the mode-I stress intensity factor is computed using a closed-form rational polynomial expression that depends on the applied pressure, pipe outer radius, wall thickness, inner radius, and the current half-crack length c. If the

KCSCLE1 model is selected, the computation uses a more detailed formulation involving polynomial coefficients G0 and G1 (and higher-order terms G2 through G4 derived from them), which are obtained by trilinear interpolation over a three-dimensional grid of the normalized geometric ratios t/Ri, a/c, and a/t. The coefficients for this interpolation are loaded from a tabulated CSV file at application startup and stored as RegularGridInterpolator objects for computational efficiency. Both SIF models compute Kmax and Kmin from the maximum and minimum pressures, respectively, and the stress intensity factor range is obtained as $\Delta K = (Kmax - Kmin) / 10^6$ to convert from Pa√m to MPa√m.

The third modeling layer is the fatigue crack growth simulation, which runs as a cycle-by-cycle iterative loop. At each iteration, the tool assembles an eighteen-feature input vector for the fatigue model, consisting of the material composition (Fe, C, Mn, P, S, Si, Ni, Cr, Mo, Al), hydrogen partial pressure, oxygen content, loading frequency, load ratio, the current stress intensity factor range ΔK, yield strength, and the previously predicted RA and FT values. The selected ML fatigue model predicts the logarithm of the crack growth rate, which is then converted to da/dN in meters per cycle using $da/dN = 10(\log_{10} da/dN) / 1000$. The crack depth increment is computed as $da = (da/dN) \times dN$, where dN is the current cycle step size. The crack depth and half-length are updated accordingly while maintaining the user-specified aspect ratio throughout the simulation. An adaptive stepping scheme accelerates computation during the early stages of crack growth, when the rate of change is small: if the ratio of the new crack depth to the previous crack depth is less than 1.01 after an iteration, the cycle step size is increased by a factor of ten. The loop checks two termination criteria at each step. The simulation stops if the maximum stress intensity factor Kmax reaches or exceeds the hydrogen-assisted cracking threshold KIH, set at 55 MPa√m, or if the crack depth reaches the critical depth defined as 25% of the pipe wall thickness.

The prediction is executed in two passes. The first pass runs the full simulation with adaptive stepping to quickly determine the total number of cycles to failure. The second pass re-executes the simulation with a fixed cycle increment to produce approximately 10,000 evenly spaced data points across the total life, generating the detailed results table used for output display, plotting, and export. Both passes run in a background thread to maintain GUI responsiveness, with progress reported to the interface via a signal-based callback. Upon completion, the tool returns a results dictionary containing the predicted RA and FT, the total cycle count, lifetime in hours and years, final Kmax and ΔK values, the critical crack depth at termination, the termination condition, and the full results table as a data frame.

5.3 Case Study Description

This case study demonstrates the application of the OU HEAT to screen the hydrogen compatibility of existing natural gas transmission pipelines. The study quantifies how predicted ductility degradation, fracture resistance, and remaining fatigue life vary with hydrogen blending level. Although the tool can be applied to a broader range of API 5L steel grades, the results presented here focus on three commonly used grades, X52, X60, and X70, to provide a clear and consistent basis for comparison. To ensure that grade-to-grade differences reflect material response rather than changes in assumed operating conditions or defect size, the pipeline geometry, loading conditions, and initial flaw definition were held constant across all runs, while hydrogen concentration was varied according to the study matrix summarized in Table 5.1.

Table 5-1 Case Study Inputs and Study Matrix for OU HEAT Runs

Category	**Case study setting (applied across runs unless noted)**
Steel grades evaluated	API 5L: X52, X60, X70
Hydrogen concentration sweep	0% to 100% H_2 in natural gas
Pressure cycle	P_{min} = 2 Mpa P_{max} = 5 MPa average pressure = 3.5 MPa
Load Ratio	R = $\frac{Pmin}{Pmax} = 0.4$
Frequency	1 Hz
Oxygen content	0 ppm
Temperature	25℃
Pipe geometry	Outer diameter, D_o = 762 mm; wall thickness t = 11.2 mm
Initial flaw geometry	Semi-elliptical axial inner-surface crack; aspect ratio a/c = 0.6667
Initial crack size	Fixed across grades: a_0/t = 5%; a0 = 0.56 mm
Stress Intensity factor model	KCTCL
Fatigue crack growth model	CatBoost fatigue model
Termination criteria	Simulation terminates when the maximum stress intensity factor reaches the hydrogen-assisted cracking threshold used in OU HEAT or when crack depth reaches the critical depth criterion implemented in the tool.
Outputs reported	Predicted RA, predicted FT, Stress intensity response (ΔK), crack growth history, cycles to termination, predicted lifetime (hours and years), and termination mode.

For a fair comparison across steel grades, the initial flaw size was held constant by specifying a fixed initial crack depth to thickness ratio of $a_0/t = 5\%$ for the same wall thickness, corresponding to an initial crack depth of 0.56 mm. This isolates the influence of grade-dependent material properties from differences in assumed defect populations or inspection resolution.

Hydrogen concentration was treated as the primary study variable and was varied from 0% to 100% to generate trends in predicted RA and FT, and to connect those trends to fatigue crack growth behavior and remaining life outcomes. All simulations used the same pressure cycle, frequency, temperature, oxygen content, pipe geometry, initial flaw definition, and model selections listed in Table 5.1, so that differences in predicted outcomes can be interpreted directly in terms of steel grade and hydrogen blending level.

5.4 Tool Predictions and Validation

Using the baseline case study setup in Section 5.3, OU HEAT was run for X52, X60, and X70 while hydrogen concentration was varied from 0% to 100%. All other inputs, including pipe geometry, pressure cycling conditions, and initial flaw definition, were held constant to isolate the effect of hydrogen blending and steel grade. The results are presented in three parts: predicted RA, predicted FT, and the predicted remaining fatigue life from the integrated crack growth simulation.

5.4.1 Predicted Reduction of Area Response

Figure 5.3 presents the predicted RA as a function of hydrogen concentration for X52, X60, and X70 pipeline steels. At 0% hydrogen, the predicted RA values reflect the baseline ductility ranking of the three grades: X52 exhibits the highest RA at 73.09%, followed by X60 at 64.55%, and X70 at 43.40%. This ordering is consistent with the strength–ductility tradeoff commonly observed in carbon-manganese pipeline steels, where higher-strength microstructures tend to exhibit reduced capacity for plastic deformation. [45] also emphasize that, for pipeline steels exposed to gaseous hydrogen, degradation is most strongly expressed in ductility-related measures such as RA and elongation, while yield and ultimate tensile strength are often comparatively less affected.

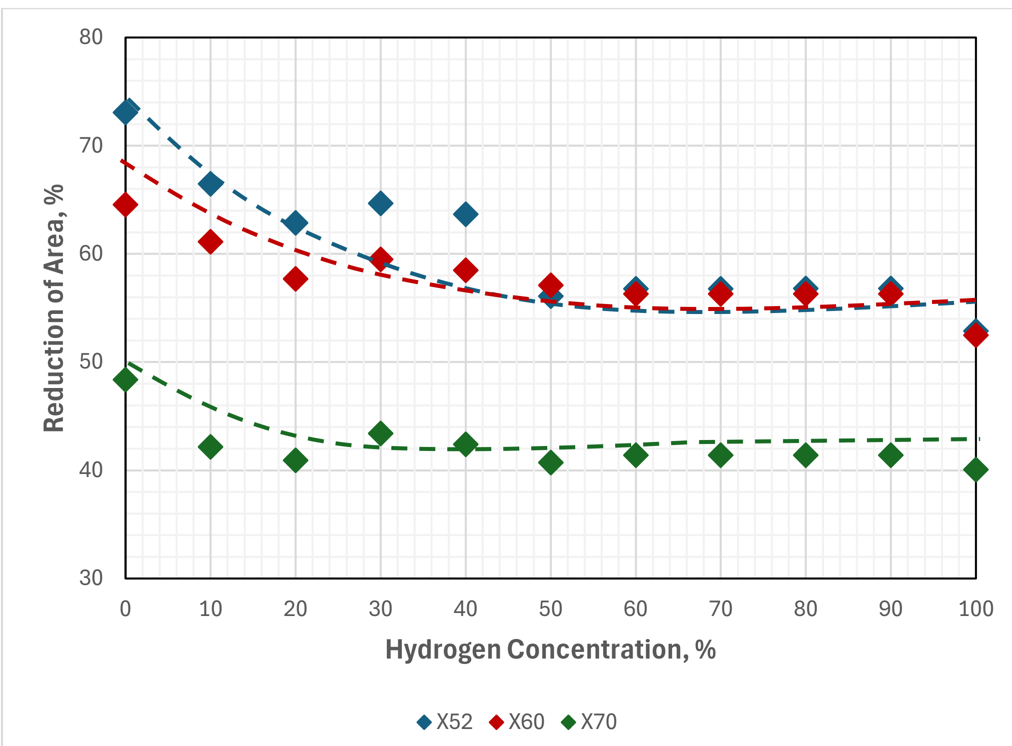

Figure 5-3 Predicted RA as a function of hydrogen concentration for API 5L X52, X60, and X70 steels

As hydrogen concentration increases from 0% to approximately 50%, the predicted RA decreases for all three grades, although the magnitude of degradation varies. X52 shows the largest absolute decline, decreasing from 73.09% to 56.11% over this range, while X60 decreases from 64.55% to 57.12%. These trends are consistent with experimental evidence that gaseous hydrogen exposure significantly reduces RA and elongation-to-failure in API pipeline steels relative to air, as reported by [27]. Blend-specific testing on API 5L X60 also indicates measurable embrittlement under hydrogen–natural gas mixtures, including a 20% blend, supporting the plausibility of ductility loss under blended-gas conditions rather than only under pure hydrogen, as demonstrated by [29].

X70 prediction shows a consistently lower reduction of area compared with X52 and X60 across the hydrogen concentration range. While X52 and X60 remain in the higher RA range and tend to converge at higher hydrogen concentrations, X70 stays around the lower RA band, generally near 40–43% after the initial drop. This indicates that X70 exhibits a lower predicted ductility reserve under hydrogen exposure. Rhythm *et al.,* 2025 [115] similarly reported hydrogen-related ductility reduction in X52, X60, and X70 steels, with grade-dependent differences in severity.

Beyond approximately 50% hydrogen, the predicted RA response approaches a plateau for all three grades, indicating diminishing additional change with further increases in hydrogen concentration under the case study conditions. X52 and X60 converge toward similar high-hydrogen RA values, reaching 52.88% and 52.50% at 100% hydrogen, respectively, despite their different baseline ductility at 0% hydrogen. This convergence suggests that while baseline ductility differs meaningfully across grades, the hydrogen-degraded ductility state can become more comparable at high hydrogen content once the embrittlement effect saturates under the modeled conditions.

5.4.2 Predicted Fracture Toughness Response

Figure 5.4 presents the predicted FT as a function of hydrogen concentration for X52, X60, and X70 steel grades. The grade ranking for FT is reversed relative to that observed for RA: X70 exhibits the highest baseline FT at 187.76 MPa$\sqrt{m}$, followed by X60 at 160.87 MPa$\sqrt{m}$, and X52 at 147.37 MPa$\sqrt{m}$. This ordering reflects that modern higher-strength pipeline steels, particularly X70 produced through thermomechanically controlled processing (TMCP), benefit from refined grain structures and optimized microalloying, which enhance crack-tip resistance despite their higher yield strength. While higher strength generally reduces ductility (as seen in the RA results), it does not necessarily reduce FT in this class of steels, where microstructural refinement can offset the strength-toughness tradeoff [45].

As hydrogen concentration increases, all three grades exhibit a progressive decline in predicted FT. X70 shows the largest absolute reduction, diminishing from 187.76 MPa$\sqrt{m}$ at 0% hydrogen to 152.96 MPa$\sqrt{m}$ at 100% hydrogen, a loss of approximately 34.8 MPa$\sqrt{m}$. X60 declines from 160.87 to 144.75 MPa$\sqrt{m}$, a loss of approximately 16.1 MPa$\sqrt{m}$, and X52 from 147.37 to 134.88 MPa$\sqrt{m}$, a loss of approximately 12.5 MPa$\sqrt{m}$. The general trend of decreasing FT with increasing hydrogen exposure is consistent with the experimental findings of Gyaabeng et al. (2025), who performed FT tests on X52, X60, and X70 compact tension specimens under hydrogen partial pressures ranging from 0 to 6.9 MPa and reported that increasing hydrogen partial pressure significantly reduced FT across all three grades. Despite the larger absolute decline in X70, this grade retains the highest FT across the entire hydrogen concentration range, maintaining a consistent advantage over X60 and X52 at every blending level.

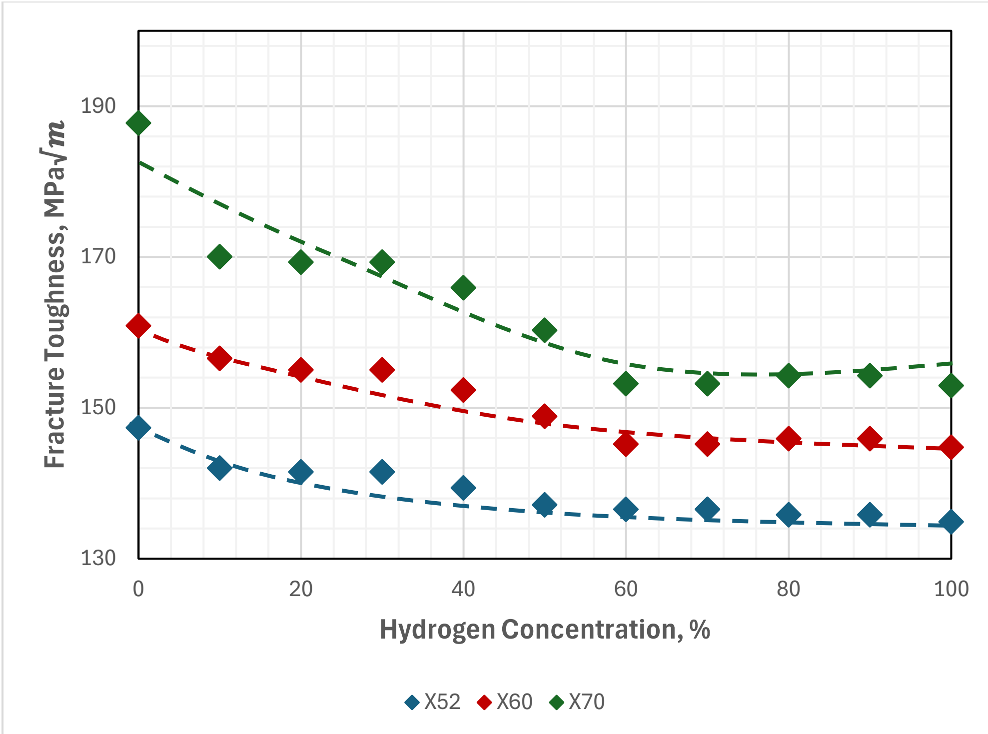

Figure 5-4 Predicted FT as a function of hydrogen concentration for API 5L X52, X60, and X70 steels

Similar to the RA results in figure 5.3, all three grades exhibit a saturation effect in FT degradation. The decline is steepest between 0% and approximately 50 to 60% hydrogen, after which the curves flatten and the predicted values remain relatively stable through 100%. X52 stabilizes near 135 to 136 MPa$\sqrt{m}$ beyond 60% hydrogen, X60 near 145 MPa$\sqrt{m}$, and X70 near 153 to 154 MPa$\sqrt{m}$. This parallel saturation behavior between RA and FT is physically reasonable, as both properties are governed by the same underlying hydrogen damage mechanisms, namely hydrogen-enhanced localized plasticity (HELP) and hydrogen-enhanced decohesion (HEDE), which reach a limiting effect once the local hydrogen concentration at microstructural trapping sites approaches saturation [121].

5.4.3 Predicted Remaining Fatigue Life Response

Figure 5.5 presents the predicted fatigue lifetime in hours as a function of hydrogen concentration for the three steel grades. The lifetime results reflect the combined influence of the predicted material properties (RA and FT) and the grade-specific composition on the fatigue crack growth simulation, and the resulting ranking differs from that observed for either property alone.

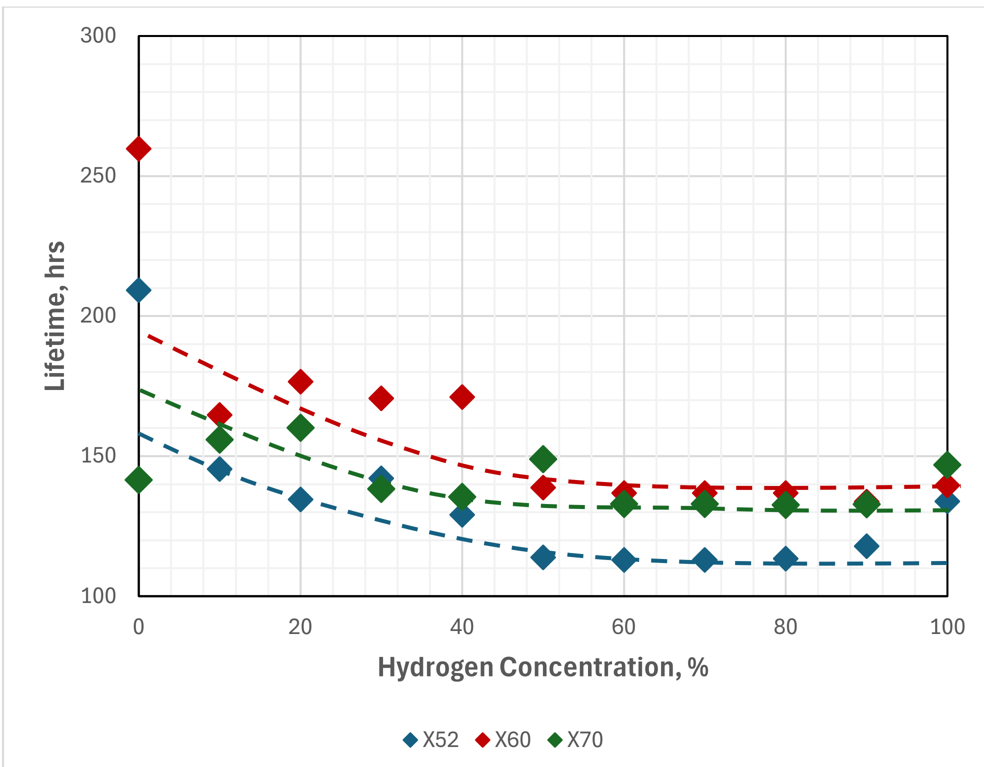

Figure 5-5 Predicted lifetime as a function of hydrogen concentration for API 5L X52, X60, and X70 steels

At 0% hydrogen, X60 exhibits the longest predicted lifetime at 259.82 hours, followed by X52 at 209.24 hours, and X70 at 141.58 hours. This ordering does not follow the RA ranking (where X52 was highest) or the FT ranking (where X70 was highest), indicating that lifetime is governed by a more complex interplay among the eighteen input features that drive the fatigue crack growth model. The favorable performance of X60 at baseline conditions suggests that this grade occupies an advantageous intermediate position, combining sufficient ductility (RA = 64.55%) and fracture resistance (FT = 160.87 MPa$\sqrt{m}$) to produce lower predicted crack growth rates under the specified loading and geometry. X70, despite its superior FT, is penalized by its lower ductility, which the ML fatigue model has learned to associate with accelerated crack growth rates. X52 falls between the two, benefiting from its high ductility but limited by its lower FT relative to X60.

As hydrogen concentration increases from 0% to approximately 50 to 60%, all three grades exhibit substantial reductions in predicted lifetime. X60 shows the largest absolute decline, dropping from 259.82 hours at 0% hydrogen to 136.88 hours at 60%, a reduction of approximately 47%. X52 declines from 209.24 hours to 112.97 hours over the same range, a reduction of approximately 46%. X70 shows a comparatively smaller absolute decline, from 141.58 hours to 132.92 hours at 60%, a reduction of approximately 6%. The relatively muted response of X70 is consistent with the RA and FT trends observed earlier, where X70 exhibited the least hydrogen-induced property degradation, leaving its crack growth behavior less affected by increasing hydrogen levels.

Beyond approximately 60% hydrogen, the lifetime predictions for all three grades plateau and the differences between grades narrow considerably. In the 60 to 80% hydrogen range, X52 stabilizes near 112 to 113 hours, X60 near 136 to 137 hours, and X70 near 132 to 133 hours. This convergence is consistent with the experimental findings of [118], who conducted fatigue crack growth tests on X52 and X70 steels in hydrogen gas pressurized to 5.5 MPa and 34 MPa and reported that there was very little difference between the FCG rates of the base metal among the steels at a given hydrogen pressure. Similarly, [117] tested four pipeline steels (two X52 and two X70 alloys) and found that at high hydrogen pressures and high values of the stress intensity factor range, there was no difference in fatigue crack growth rates regardless of strength or microstructure. These experimental observations provide independent support for the convergence in predicted lifetimes observed in this study at elevated hydrogen concentrations.

A slight increase in predicted lifetime is observed at 100% hydrogen for all three grades relative to their minimum values (X52 rises from 112.97 to 133.92 hours, X60 from 133.81 to 139.59 hours, and X70 from 132.83 to 146.94 hours). These minor fluctuations are within the inherent prediction variability of the ML fatigue model and do not alter the dominant trend of declining lifetime with increasing hydrogen concentration. The overall reduction in predicted lifetime from 0% to 100% hydrogen remains substantial for all three grades, and the convergence in fatigue performance across grades at elevated hydrogen levels is consistent with the experimental observations of [117], [118].

5.5 Sensitivity Analysis

To evaluate how uncertainty in hydrogen concentration influences the predicted fatigue response, a sensitivity analysis was performed using the built-in parametric study capability of OU HEAT. The analysis was conducted on X60 steel for three reasons. First, X60 exhibited the longest predicted baseline lifetime among the three grades evaluated in the case study, making it a practical reference case for assessing robustness of the predicted outcome under hydrogen blending. Second, X60 is widely deployed in existing natural gas transmission infrastructure [15], so its sensitivity response is directly relevant to pipeline repurposing and compatibility screening decisions. Third, X60 occupies an intermediate position between X52 and X70 in strength and ductility, which makes it a reasonable representative grade for illustrating how hydrogen concentration perturbations propagate through the integrated crack growth simulation.

Hydrogen concentration was perturbed about a baseline value of 19% using the tool's +/-25% variation rule, generating three cases: 14.25% (−25%), 19% (baseline), and 23.75% (+25%), while all other inputs were held constant at the case study values. The sensitivity response is presented using three complementary plots: crack growth rate versus stress intensity factor range (da/dN vs ΔK), crack growth rate versus time (da/dN vs t), and crack depth versus time (a vs t). Together, these plots show how changes in hydrogen concentration affect both the crack growth kinetics and the time evolution of crack depth toward the termination criterion under the baseline operating scenario.

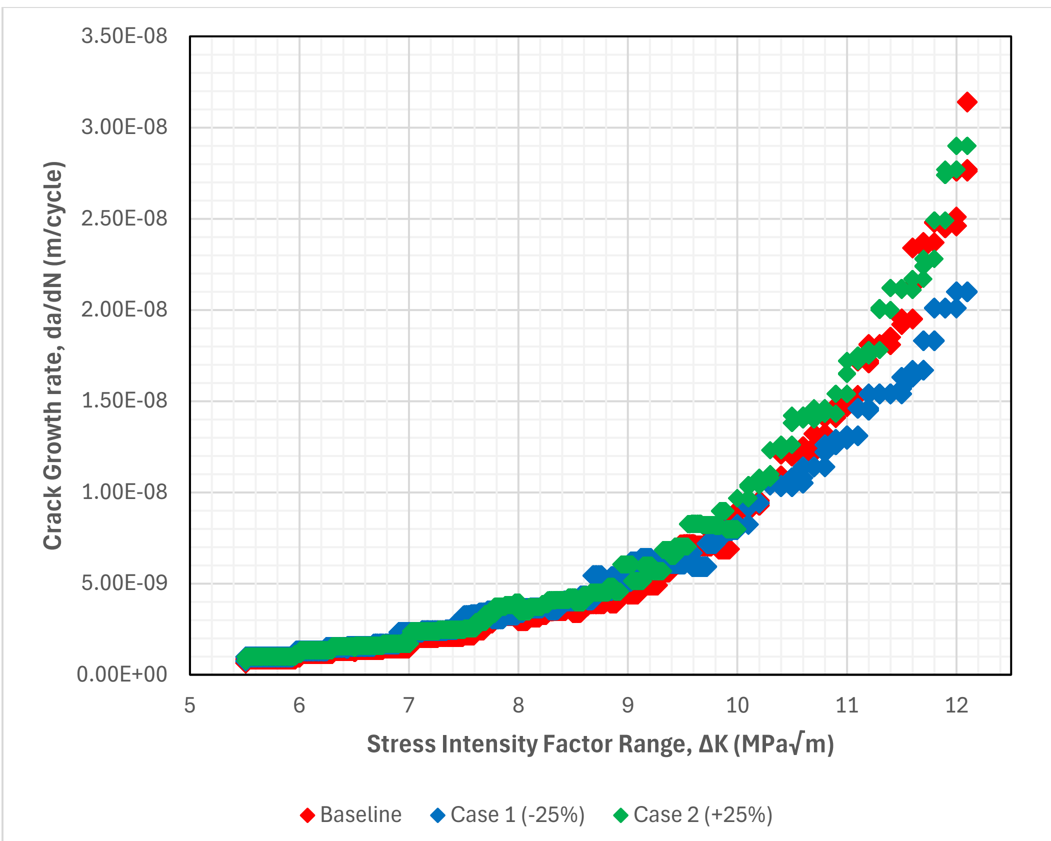

Figure 5-6 Sensitivity analysis on hydrogen concentration for X60: crack growth rate (da/dN) versus stress intensity factor range

Figure 5.6 presents the predicted crack growth rate as a function of the stress intensity factor range for the three hydrogen concentration cases. At low values of ΔK, the three cases are tightly clustered with minimal separation, indicating that the influence of a +/- 25% variation in hydrogen concentration on the crack growth kinetics is negligible in the early stages of crack propagation when the driving force is small. As ΔK increases beyond approximately 8 to 9 MPa$\sqrt{m}$, the curves begin to diverge, with the higher hydrogen concentration case (+25%) producing progressively higher crack growth rates than the baseline, and the lower concentration case (-25%) producing the lowest rates. This separation continues to widen as ΔK approaches the termination threshold.

This behavior is consistent with the understanding that hydrogen-assisted fatigue crack growth is most pronounced at higher stress intensity levels, where the larger crack-tip plastic zone facilitates greater hydrogen accumulation and more extensive hydrogen-microstructure interaction [121]. At low ΔK values, the crack-tip hydrogen concentration remains insufficient to meaningfully alter the local damage mechanism, and all three cases follow a similar growth trajectory. The increasing separation at higher ΔK demonstrates that hydrogen concentration becomes a more influential parameter as the crack approaches critical conditions, which has direct implications for inspection scheduling and remaining life estimates in pipelines operating at higher hydrogen blend ratios.

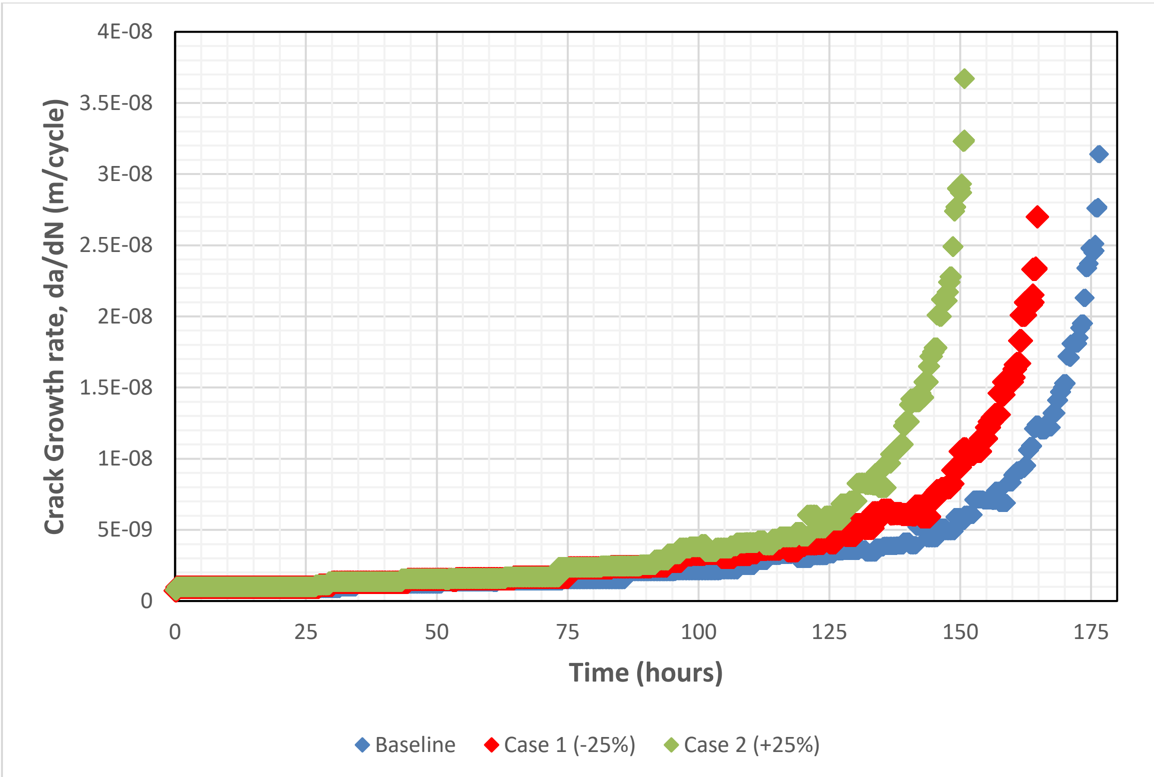

Figure 5-7 Sensitivity analysis on hydrogen concentration for X60: crack growth rate (da/dN) versus time

Figure 5.7 shows the predicted crack growth rate as a function of time for the three hydrogen concentration cases. All three cases exhibit a characteristic two-phase response: a prolonged initial period during which the crack growth rate remains low and relatively stable, followed by a sharp, exponential acceleration in the final stage of the simulation as the crack approaches the termination criterion. This acceleration reflects the self-reinforcing nature of fatigue crack growth, in which increasing crack depth produces a larger stress intensity factor, which in turn drives a higher growth rate, further accelerating crack extension. A similar two-phase crack evolution pattern was reported by [6], who modeled fatigue crack growth and remaining life in API 5L X52 pipelines under cyclic hydrogen pressure loading and observed that hydrogen exposure reduced the remaining service life by accelerating the progression from stable to unstable crack growth.

The +25% case (23.75% hydrogen) enters the rapid acceleration phase earliest and terminates first, yielding the shortest predicted lifetime among the three cases. The baseline case (19% hydrogen) sustains the low-growth-rate phase the longest and terminates last, yielding the longest lifetime. The -25% case (14.25% hydrogen) falls between the two and terminates before the baseline. Although early-stage crack growth behavior is nearly indistinguishable across the three cases, the onset of rapid acceleration is notably sensitive to hydrogen level. This observation aligns with the finding of [41], who reported that hydrogen promoted the premature onset of accelerated (Stage III) crack growth in pipeline steel. The horizontal separation among the three termination points shows that even moderate changes in hydrogen blend ratio can meaningfully shift the time at which the crack transitions from stable to unstable growth, with direct implications for inspection scheduling and remaining life estimates in pipelines operating at higher hydrogen blend ratios.

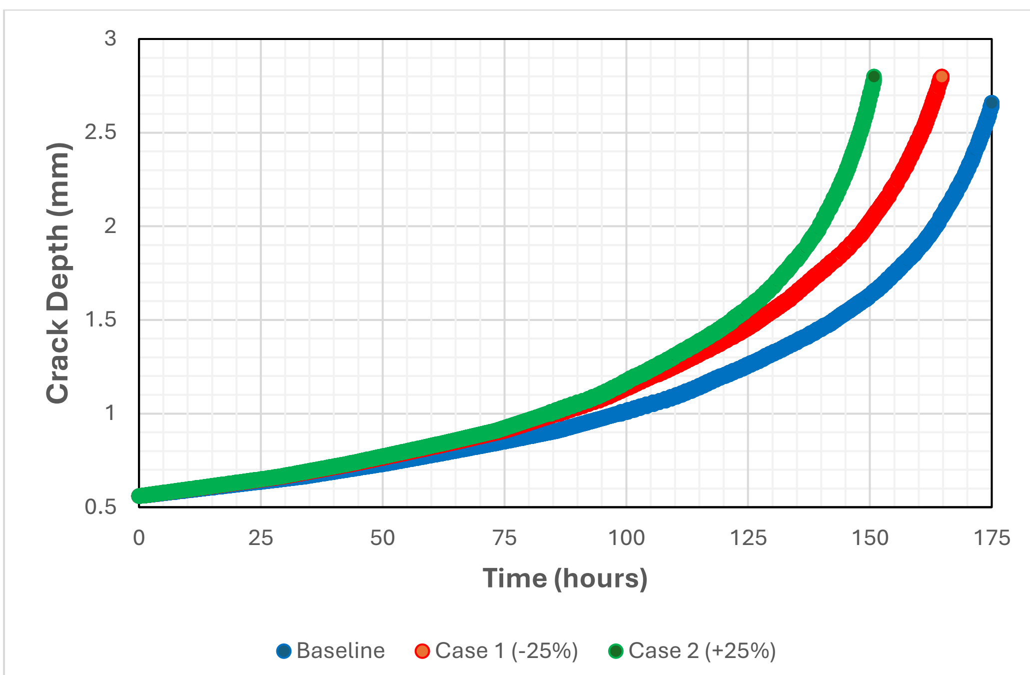

Figure 5-8 Sensitivity analysis on hydrogen concentration for X60: crack depth (a) versus time

Figure 5.8 presents the predicted crack depth as a function of time for the three hydrogen concentration cases. All three cases originate from the same initial crack depth and terminate at the same critical depth (25% of wall thickness), but the time required to traverse that distance differs across cases. The crack growth trajectory follows the same two-phase pattern observed in the da/dN versus time plot (Figure 5.7): a prolonged period of gradual, nearly linear crack extension followed by a sharp upward inflection as the crack accelerates toward the termination criterion.

The three curves are closely grouped during the early phase of growth, confirming that a ±25% variation in hydrogen concentration has limited influence on crack propagation while the crack remains small and the stress intensity factor is low. The curves begin to separate as the crack deepens and the growth rate accelerates, with the +25% case (23.75% hydrogen) reaching the critical depth first and the baseline case (19% hydrogen) last. The -25% case (14.25% hydrogen) terminates between the two. The horizontal spread between the termination points of the three curves represents the practical window of lifetime variation attributable to a ±25 % change in the hydrogen blend ratio under otherwise identical operational conditions.

From an engineering perspective, this plot illustrates a key characteristic of hydrogen-assisted fatigue in pipelines: the majority of the service life is consumed during the slow-growth phase, while the transition from a seemingly stable crack to one that rapidly approaches the failure criterion occurs over a comparatively short time window. This has important implications for inspection planning, as a crack that appears stable during routine assessment could accelerate to critical depth between inspection intervals if the hydrogen concentration increases. The sensitivity of this transition point to hydrogen blend ratio reinforces the need for conservative inspection scheduling in pipelines carrying hydrogen-blended natural gas.

5.6 Model Comparison and Validation

A critical requirement for any predictive tool intended for structural integrity assessment is demonstrating that its outputs are consistent with established approaches under comparable conditions. To validate the lifetime predictions of OU HEAT, the allowable number of loading cycles predicted by the integrated ML-fracture mechanics framework was compared against results obtained from two independent fracture mechanics-based lifetime models reported in the literature, as well as the conventional fatigue curve model upon which OU HEAT's lifetime framework was originally developed. The comparison was performed for X52 pipeline steel, which has been extensively characterized in hydrogen environments and serves as the reference material in several published validation studies.

The first reference model is the fracture mechanics-based lifetime approach reported by [13], who evaluated lifetime predictions for hydrogen pipelines using the KCSCLE1 stress intensity factor formulation and ASME B31.12 fracture mechanics procedures. The second reference is the model reported by [119], who examined codes and standards for the fatigue-based design of hydrogen infrastructure components. The third comparison case is the conventional fatigue curve model that uses the same KCTCL stress intensity factor formulation and crack geometry assumptions as OU HEAT but employs a standard Paris law formulation for crack growth rates rather than the ML-predicted values. This comparison isolates the specific contribution of the machine-learning components by holding all other aspects of the lifetime calculation constant. All three models were evaluated under identical material properties, pipe geometry, initial crack dimensions, and loading conditions to provide a consistent basis for comparison. The pipe geometry corresponds to an outer diameter of 323.9 mm and a wall thickness of 16 mm, with an initial semi-elliptical surface crack defined in accordance with ASME B31.12 assumptions. The allowable number of cycles prior to reaching the critical crack depth or stress intensity threshold was used as the primary validation metric.

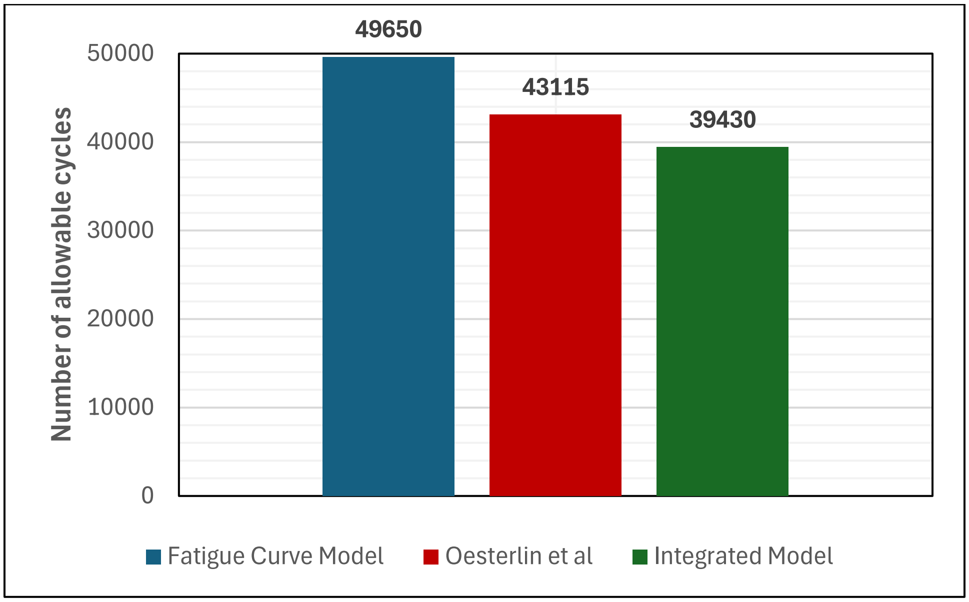

Figure 5-9 Comparison of allowable cycles predicted by different lifetime models for X52 pipeline steel (Pmin = 5 MPa, Pmax = 20 MPa)

Figure 5.9 presents the predicted allowable number of loading cycles from the integrated ML-fracture mechanics framework alongside the literature-based model of Oesterlin et al. [13] and the conventional fatigue curve model developed in this work. The integrated framework produces a prediction that lies within the range bounded by these two reference approaches. The closest agreement is observed with the fatigue curve model, a result that is expected given that both share the same KCTCL stress intensity factor formulation and identical crack geometry assumptions. The distinguishing factor between the two is the incorporation of machine-learning predictions of hydrogen-dependent material degradation within the integrated framework. The minor numerical differences between these two predictions arise from the use of ML-based estimates of FT and fatigue crack growth rate, which introduce small deviations compared to purely analytical formulations but remain physically consistent with well-documented hydrogen embrittlement behavior.

The deviation from the Oesterlin et al. [13] model is larger, and this is attributed primarily to differences in the stress intensity factor solution and hydrogen exposure conditions. Oesterlin et al. [13] employ the KCSCLE1 stress intensity formulation, whereas the OU HEAT framework uses KCTCL in accordance with ASME FFS-1. Furthermore, the hydrogen concentration corresponding to the results reported by Oesterlin et al. [13] is not explicitly stated in their publication. For the purpose of demonstration and maintaining consistency within this study, a hydrogen concentration of 20% was assumed when running the integrated framework. Despite these methodological differences, the integrated model maintains reasonable agreement with the literature, confirming that the proposed framework is capable of reproducing established lifetime predictions while offering the added functionality of explicitly capturing hydrogen-dependent material degradation through machine learning.

To examine the robustness of this agreement across different loading conditions, the comparison was repeated under a reduced-pressure regime with a maximum pressure of 10 MPa and a minimum of 1 MPa. Figure 5.10 presents the results for this second case.

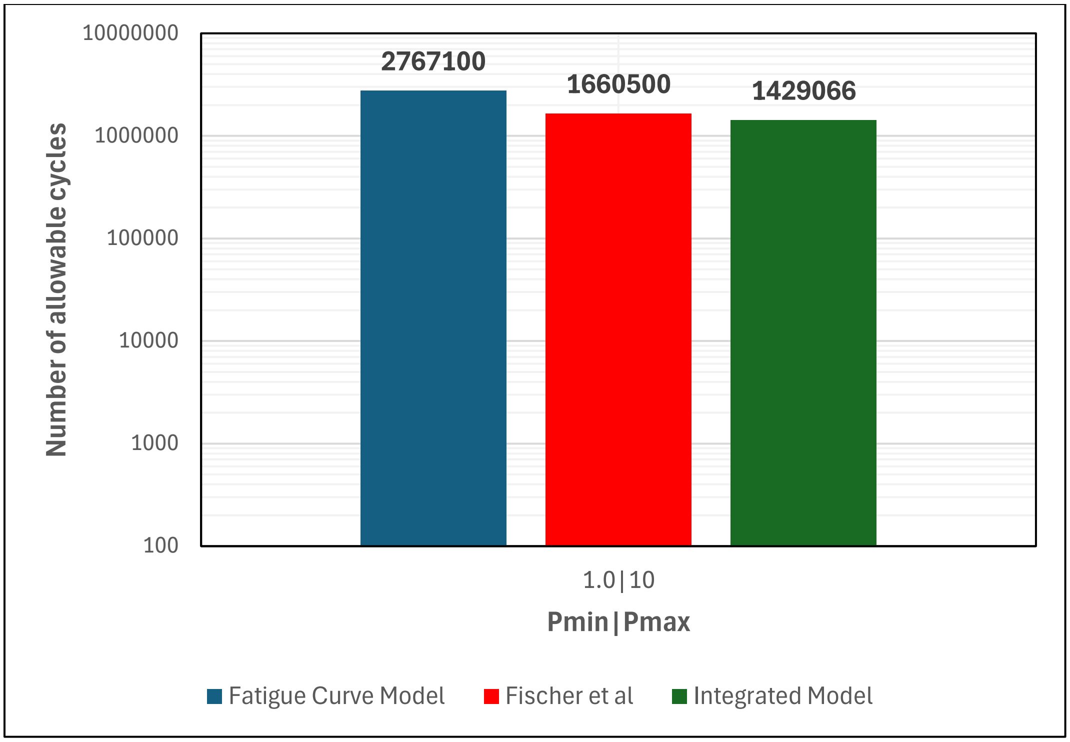

Figure 5-10 Comparison of predicted allowable cycles for X52 pipeline steel under cyclic internal pressure loading (Do = 323.9 mm, t = 16 mm, Pmin = 1 MPa, Pmax = 10 MPa)

Figure 5.10 compares the allowable cycles predicted by the integrated ML-fracture mechanics framework, the model of [119], and the conventional fatigue curve model for X52 steel under cyclic internal pressures from 1 to 10 MPa. As in the first validation case, all models were evaluated using the same material properties, pipe geometry, and initial crack dimensions to ensure a fair and direct comparison. The integrated framework again produces lifetime predictions that fall within the range established by the literature-based and fatigue curve models, demonstrating that the tool maintains consistent behavior across different pressure amplitudes.

As observed in the higher-pressure case, the integrated model shows closer agreement with the fatigue curve model, which is a direct consequence of both approaches sharing the same KCTCL stress intensity factor formulation and crack geometry assumptions. The deviations relative to the [119] predictions are attributable to differences in the stress-intensity formulations and hydrogen-exposure assumptions employed in that study, as well as to the use of ML-based predictions of hydrogen-dependent material degradation in the integrated framework. Notwithstanding these differences, the degree of agreement observed across all three models under both high-pressure and moderate-pressure loading regimes confirms that the proposed framework delivers stable and physically consistent lifetime predictions regardless of the cyclic pressure severity. This consistency across multiple loading conditions further supports the validity and applicability of the integrated framework for hydrogen pipeline integrity assessment.

CHAPTER 6

CONCLUSIONS AND RECOMMENDATIONS

6.1 Conclusions

This study developed a compatibility assessment model for existing pipelines intended to transport hydrogen-containing natural gas by integrating machine-learning predictions of hydrogen-sensitive material degradation with fracture-mechanics-based crack-growth simulation. The resulting framework was implemented as the University of Oklahoma Hydrogen Embrittlement Assessment Tool (OU HEAT), which consolidates property prediction, stress-intensity-factor computation, and cycle-by-cycle fatigue-crack-growth simulation into a single workflow to produce integrity-relevant outputs, including predicted RA, FT, crack-growth history, cycles to termination, and remaining life. The following conclusions are drawn from the tool's application, case-study evaluation, sensitivity analysis, and validation comparisons:

i. **OU HEAT provides a unified screening workflow that links hydrogen-dependent material degradation to crack-driven integrity outcomes:** The tool architecture combines ML-based predictions of RA and FT with an 18-feature ML fatigue crack growth model and a stress intensity factor formulation, enabling direct propagation of hydrogen effects into crack growth evolution and predicted lifetime.

ii. **Predicted ductility loss trends show meaningful degradation with increasing hydrogen concentration and a saturation-type response at higher blend levels:** In the case study, the RA decreased with increasing hydrogen concentration for X52 and X60 and remained comparatively low for X70. Across the grades, the predicted RA trends approach a plateau beyond mid-range hydrogen concentrations, indicating diminishing incremental change at high blend levels under the modeled conditions.

iii. **Predicted FT decreases with hydrogen concentration for all grades, with trends that also flatten at higher hydrogen levels:** The FT predictions show progressive decline as hydrogen concentration increases, with the steepest reductions occurring from low to mid-range hydrogen levels and more stable values beyond approximately the mid-range region. The results also show that grade ranking in toughness does not necessarily mirror ductility ranking, reinforcing that integrity decisions should not rely on a single property metric.

iv. **Predicted remaining fatigue life decreases significantly with hydrogen concentration and tends to converge across grades at elevated hydrogen levels:** Under the fixed geometry and loading scenario used in the case study, the predicted lifetime decreases strongly from 0% hydrogen to the mid-range concentrations for all grades, with X60 showing the longest baseline lifetime and a large absolute reduction as hydrogen increases. Beyond approximately the mid-range region, lifetime trends show a plateau and narrower separation among the three grades.

v. **Hydrogen concentration sensitivity becomes more pronounced at higher crack-driving conditions, particularly as the crack approaches termination:** The hydrogen concentration sensitivity study performed on X60 (baseline 19% with +/-25% pertubations) indicates that differences among cases are small at low driving force and become clearer at higher stress intensity factor range and in the later stage of the crack growth. This provides a practical interpretation: uncertainty in hydrogen concentration has limited influence early in the life calculation but can shift the timing of the final acceleration stage and termination.

vi. **Comparative validation indicates that OU HEAT produces lifetime predictions that are consistent with established fracture mechanics-based approaches under comparable conditions:** The validation strategy compares the number of allowable cycles predicted by the integrated framework with literature-based lifetime models and an in-house fatigue curve baseline under the same geometry and loading. The integrated model behavior was shown to fall within the range of comparison approaches, supporting that the framework is capable of reproducing conventional lifetime prediction behavior while incorporating hydrogen-dependent degradation through ML.

6.2 Recommendations

6.2.1 Recommendations for practical use of OU HEAT

i. **Use OU HEAT as a screening and prioritization tool, not as a stand-alone acceptance decision:** The most appropriate use is early-stage evaluation of hydrogen blending scenarios to identify high-risk combinations of material grade, blend level, and defect size that warrant higher-fidelity assessment or targeted testing.

ii. **Treat hydrogen concentration as a high-impact operational variable when planning integrity management actions:** Sensitivity trends indicate that changes in hydrogen concentration can meaningfully shift crack growth behavior in the later stages of propagation under the modeled conditions. Operators should reflect this in conservative inspection interval planning when blend ratios are expected to fluctuate.

iii. **Prioritize realistic flaw characterization when applying the tool to in-service assets:** Because lifetime results depend on assumed defect geometry and size, the most defensible use of OU HEAT for asset screening is when the initial flaw assumptions are tied to inspection capability and measurement confidence rather than generic defaults.

iv. **Use the model comparison capability when decisions are sensitive to SIF formulation or fatigue model choice:** Where results are used to support a repurposing decision, running key scenarios under multiple SIF and fatigue model options and comparing results supports robustness checks and highlights model-form uncertainty.

6.2.2 Recommendations for tool enhancement and future deployment

While the integrated framework developed in this study provides a functional and validated tool for hydrogen pipeline compatibility screening, several areas warrant further investigation to enhance its applicability and predictive confidence:

i. The current ML models were trained on literature-compiled databases that, while broad in coverage, are subject to inter-laboratory variability and gaps in certain regions of the input space. Expanding the training datasets with additional experimental measurements, particularly for weld metal, and heat-affected zone specimens, would improve model reliability in these domains.

ii. The sensitivity analysis was limited to a single parameter (hydrogen concentration) perturbed about one baseline condition. A broader parametric study examining multiple parameters simultaneously, including initial crack depth, load ratio, oxygen content, yield strength, and temperature, would provide a more complete characterization of the tool's sensitivity landscape and support the development of uncertainty-informed integrity assessments.

iii. Validation of OU HEAT was performed against code-based and literature-based fracture mechanics models. Future work should pursue validation against full-scale or component-level hydrogen fatigue test data, where available, to further establish confidence in the tool's predictions under conditions that more closely replicate field service.

iv. Finally, the current tool operates as a deterministic screening tool. Future work should consider the development of physics-informed machine learning models that integrate data-driven prediction with established fracture mechanics principles and hydrogen embrittlement behavior. Incorporating physical constraints, such as monotonic degradation with increasing hydrogen exposure and crack growth dependence on stress intensity factor, would help improve model consistency and reduce non-physical prediction trends. This would strengthen the reliability of the framework and provide a more robust basis for risk-informed pipeline integrity management decisions.

NOMENCLATURE

Symbols

Geometry and crack description

a = crack depth (m or mm)

a_0 = initial crack depth (m or mm)

a_{crit} = critical crack depth (m or mm)

a_{allow} = allowable crack depth (m or mm)

c = crack half-length parameter used in stress intensity solution (m or mm)

c_0 = initial crack half-length (m or mm)

$2c$ = surface crack length (m or mm)

a/c = crack aspect ratio (dimensionless)

a/t = normalized crack depth (dimensionless)

t = pipe wall thickness (m or mm)

D_o = pipe outer diameter (m or mm)

R_i = pipe inner radius (m or mm)

R_o = pipe outer radius (m or mm)

φ = crack-front location angle used for evaluation (degrees or radians)

Loading and operating conditions

P = internal pressure (Pa or MPa)

P_{min} = minimum internal pressure in a cycle (Pa or MPa)

P_{max} = maximum internal pressure in a cycle (Pa or MPa)

R = load ratio (dimensionless), typically $R = P_{min} / P_{max}$ for pressure cycling

f = loading frequency (Hz)

T = temperature (℃ or K, as specified)

Fracture Mechanics and crack growth

KI (K) = Mode I stress intensity factor (Pa$\sqrt{m}$ or MPa$\sqrt{m}$)

K_{max} = maximum stress intensity factor in a loading cycle (Pa$\sqrt{m}$ or MPa$\sqrt{m}$)

K_{min} = minimum stress intensity factor in a loading cycle (Pa$\sqrt{m}$ or MPa$\sqrt{m}$)

ΔK = stress intensity factor range, ΔK = K_max − K_min (Pa$\sqrt{m}$ or MPa$\sqrt{m}$)

K_{IH} = threshold stress intensity factor for hydrogen-assisted cracking (MPa$\sqrt{m}$)

K_{IC} = plane-strain fracture toughness (MPa$\sqrt{m}$)

N = number of cycles (cycles)

ΔN (dN) = cycle increment per iteration (cycles)

da/dN = fatigue crack growth rate (m/cycle or mm/cycle) log(da/dN) = logarithm of fatigue crack growth rate predicted by the ML fatigue model (dimensionless)

Δa = crack depth increment per step, $\Delta a = (da/dN)\,\Delta N$ (m or mm)

N_{crit} = total cycles at termination (cycles)

KCTCL model coefficients and geometry parameters

G_0 = influence coefficient for membrane stress contribution (dimensionless)

G_1 = influence coefficient for bending stress contribution (dimensionless)

G_p = influence coefficient for internal pressure with crack-face loading (dimensionless)

λ = cracked-cylinder geometry parameter used in influence-coefficient evaluation (dimensionless)

Hydrogen and environment descriptors

xH2 = hydrogen concentration in the gas blend (fraction or %)

P_{H2} = hydrogen partial pressure (MPa)

O_2 (ppm) = oxygen content in the gas stream (ppm)

Material properties

SMYS = specified minimum yield strength (MPa)

S_y (YS) = yield strength (MPa)

UTS = ultimate tensile strength (MPa)

RA = reduction of area (%)

FT = fracture toughness (MPa$\sqrt{m}$)

Time and life outputs

t_{life} = predicted lifetime (hours or years), computed from cycles and frequency

Abbreviations

API = American Petroleum Institute

ASME = American Society of Mechanical Engineers

ASME B31.12 = Hydrogen Piping and Pipelines standard

FFS = fitness-for-service

GUI = graphical user interface

HE = hydrogen embrittlement

HEE = hydrogen environment embrittlement

IHE = internal hydrogen embrittlement

LEFM = linear elastic fracture mechanics

ML = machine learning

NDT = nondestructive testing

OU HEAT = University of Oklahoma Hydrogen Embrittlement Assessment Tool

SIF = stress intensity factor

TMCP = thermomechanically controlled processing

REFERENCES

[1] T. T. Nguyen, N. Tak, J. Park, S. H. Nahm, and U. B. Beak, "Hydrogen embrittlement susceptibility of X70 pipeline steel weld under a low partial hydrogen environment," *International Journal of Hydrogen Energy*, vol. 45, no. 43, pp. 23739–23753, Sep. 2020, doi: 10.1016/j.ijhydene.2020.06.199.

[2] J. Wijnen, J. Parker, M. Gagliano, and E. Martínez-Pañeda, "Virtual failure assessment diagrams for hydrogen transmission pipelines," *International Journal of Hydrogen Energy*, vol. 149, p. 149984, Jul. 2025, doi: 10.1016/j.ijhydene.2025.06.174.

[3] K. Topolski *et al.*, "Hydrogen blending into natural gas pipeline infrastructure: Review of the state of technology," 2022.

[4] K. Bagnoli, G. Wilkowski, E. Twombly, E. Punch, L. Hill, and P. Krishnaswamy, "Review of Integrity Threat Characterization Resulting from Hydrogen Gas Pipeline Service," *Pipeline Hazardous Materials Safety Administration, Department of Transportation, Washington, DC*, 2023.

[5] M. A. Kappes and T. Perez, "Hydrogen blending in existing natural gas transmission pipelines: a review of hydrogen embrittlement, governing codes, and life prediction methods," *Corrosion Reviews*, vol. 41, no. 3, pp. 319–347, Jun. 2023, doi: 10.1515/corrrev-2022-0083.

[6] V. Hasanli, "Quantifying conservatism in ASME B31.12 Option A for hydrogen pipeline repurposing," *International Journal of Hydrogen Energy*, vol. 191, p. 152188, Nov. 2025, doi: 10.1016/j.ijhydene.2025.152188.

[7] R. Depraetere, W. De Waele, M. Cauwels, T. Depover, K. Verbeken, and S. Hertelé, "Modeling of Hydrogen-Charged Notched Tensile Tests of an X70 Pipeline Steel with a Hydrogen-Informed Gurson Model," *Materials*, vol. 16, no. 13, p. 4839, Jul. 2023, doi: 10.3390/ma16134839.

[8] O. Bouledroua, D. Zelmati, Z. Hafsi, and M. B. Djukic, "Hydrogen embrittlement effects on remaining life and fatigue crack growth rate in API 5L X52 steel pipelines under cyclic pressure loading," *Engineering Failure Analysis*, vol. 166, p. 108917, Dec. 2024, doi: 10.1016/j.engfailanal.2024.108917.

[9] S. Nazar and E. Proverbio, "Modeling of hydrogen-assisted fatigue crack growth in carbon steel pipelines," *International Journal of Hydrogen Energy*, vol. 138, pp. 548–558, Jun. 2025, doi: 10.1016/j.ijhydene.2025.05.205.

[10] L. E. Faucon, T. Boot, T. Riemslag, S. P. Scott, P. Liu, and V. Popovich, "Hydrogen-accelerated fatigue of API X60 pipeline steel and its weld," *Metals*, vol. 13, no. 3, p. 563, 2023.

[11] M. A. Kappes and T. E. Perez, "Blending hydrogen in existing natural gas pipelines: Integrity consequences from a fitness for service perspective," *Journal of Pipeline Science and Engineering*, vol. 3, no. 4, p. 100141, Dec. 2023, doi: 10.1016/j.jpse.2023.100141.

[12] A. Islam, T. Alam, N. Sheibley, K. Edmonson, D. Burns, and M. Hernandez, "Hydrogen blending in natural gas pipelines: A comprehensive review of material compatibility and safety considerations," *International Journal of Hydrogen Energy*, vol. 93, pp. 1429–1461, Dec. 2024, doi: 10.1016/j.ijhydene.2024.10.384.

[13] M. F. W. Chowdhury, C. V. Tapia-Bastidas, J. Hoschke, J. Venezuela, and A. Atrens, "A review of influence of hydrogen on fracture toughness and mechanical properties of gas transmission pipeline steels," *International Journal of Hydrogen Energy*, vol. 102, pp. 181–221, Feb. 2025, doi: 10.1016/j.ijhydene.2025.01.018.

[14] N. Ahmed, M. Aldaw, R. Ahmed, and C. Teodoriu, "Modeling of necking area reduction of carbon steel in hydrogen environment using machine learning approach," *Engineering Failure Analysis*, vol. 156, p. 107864, Feb. 2024, doi: 10.1016/j.engfailanal.2023.107864.

[15] M. Gyaabeng, R. Ahmed, N. Ahmed, C. Teodoriu, and D. Devegowda, "Modeling the Impact of Hydrogen Embrittlement on the Fracture Toughness of Low-Carbon Steel Using a Machine Learning Approach," *Metals*, vol. 15, no. 6, p. 588, May 2025, doi: 10.3390/met15060588.
[16] O. Barrera *et al.*, "Understanding and mitigating hydrogen embrittlement of steels: a review of experimental, modelling and design progress from atomistic to continuum," *J Mater Sci*, vol. 53, no. 9, pp. 6251–6290, May 2018, doi: 10.1007/s10853-017-1978-5.
[17] H. Yu *et al.*, "Hydrogen Embrittlement as a Conspicuous Material Challenge─Comprehensive Review and Future Directions," *Chem. Rev.*, vol. 124, no. 10, pp. 6271–6392, May 2024, doi: 10.1021/acs.chemrev.3c00624.
[18] S. Lynch, "Hydrogen embrittlement phenomena and mechanisms," *Corrosion Reviews*, vol. 30, no. 3–4, pp. 105–123, Jun. 2012, doi: 10.1515/corrrev-2012-0502.
[19] M. B. Djukic, G. M. Bakic, V. Sijacki Zeravcic, A. Sedmak, and B. Rajicic, "The synergistic action and interplay of hydrogen embrittlement mechanisms in steels and iron: Localized plasticity and decohesion," *Engineering Fracture Mechanics*, vol. 216, p. 106528, Jul. 2019, doi: 10.1016/j.engfracmech.2019.106528.
[20] X. Wu, H. Zhang, M. Yang, W. Jia, Y. Qiu, and L. Lan, "From the perspective of new technology of blending hydrogen into natural gas pipelines transmission: Mechanism, experimental study, and suggestions for further work of hydrogen embrittlement in high-strength pipeline steels," *International Journal of Hydrogen Energy*, vol. 47, no. 12, pp. 8071–8090, Feb. 2022, doi: 10.1016/j.ijhydene.2021.12.108.
[21] H. Ghadiani, Z. Farhat, T. Alam, and Md. A. Islam, "Assessing Hydrogen Embrittlement in Pipeline Steels for Natural Gas-Hydrogen Blends: Implications for Existing Infrastructure," *Solids*, vol. 5, no. 3, pp. 375–393, Jul. 2024, doi: 10.3390/solids5030025.
[22] S. K. Dwivedi and M. Vishwakarma, "Hydrogen embrittlement in different materials: A review," *International Journal of Hydrogen Energy*, vol. 43, no. 46, pp. 21603–21616, Nov. 2018, doi: 10.1016/j.ijhydene.2018.09.201.
[23] N. E. Nanninga, Y. S. Levy, E. S. Drexler, R. T. Condon, A. E. Stevenson, and A. J. Slifka, "Comparison of hydrogen embrittlement in three pipeline steels in high pressure gaseous hydrogen environments," *Corrosion Science*, vol. 59, pp. 1–9, Jun. 2012, doi: 10.1016/j.corsci.2012.01.028.
[24] A. Campari, F. Ustolin, A. Alvaro, and N. Paltrinieri, "A review on hydrogen embrittlement and risk-based inspection of hydrogen technologies," *International Journal of Hydrogen Energy*, vol. 48, no. 90, pp. 35316–35346, Nov. 2023, doi: 10.1016/j.ijhydene.2023.05.293.
[25] R. Walallawita *et al.*, "Evaluating the Effect of Blended and Pure Hydrogen in X60 Pipeline Steel for Low-Pressure Transmission Using Hollow-Specimen Slow-Strain-Rate Tensile Testing," *Metals*, vol. 14, no. 10, p. 1132, Oct. 2024, doi: 10.3390/met14101132.
[26] I. Moro, L. Briottet, P. Lemoine, E. Andrieu, C. Blanc, and G. Odemer, "Hydrogen embrittlement susceptibility of a high strength steel X80," *Materials Science and Engineering: A*, vol. 527, no. 27–28, pp. 7252–7260, Oct. 2010, doi: 10.1016/j.msea.2010.07.027.
[27] L. Briottet, I. Moro, and P. Lemoine, "Quantifying the hydrogen embrittlement of pipeline steels for safety considerations," *International Journal of Hydrogen Energy*, vol. 37, no. 22, pp. 17616–17623, Nov. 2012, doi: 10.1016/j.ijhydene.2012.05.143.
[28] C. Wang *et al.*, "Study on hydrogen embrittlement susceptibility of X80 steel through in-situ gaseous hydrogen permeation and slow strain rate tensile tests," *International Journal of Hydrogen Energy*, vol. 48, no. 1, pp. 243–256, Jan. 2023, doi: 10.1016/j.ijhydene.2022.09.228.
[29] D. Stalheim *et al.*, "Microstructure and mechanical property performance of commercial grade API pipeline steels in high pressure gaseous hydrogen," presented at the International pipeline conference, 2010, pp. 529–537.

[30] S.-G. Kim, S.-H. Shin, and B. Hwang, "Machine learning approach for prediction of hydrogen environment embrittlement in austenitic steels," *journal of materials research and technology*, vol. 19, pp. 2794–2798, 2022.
[31] X. Xing, Z. Pang, H. Zhang, J. Liu, and G. Cui, "Study of temperature effect on hydrogen embrittlement in X70 pipeline steel," *Corrosion Science*, vol. 230, p. 111939, Apr. 2024, doi: 10.1016/j.corsci.2024.111939.
[32] C. Zhou, H. Zhou, and L. Zhang, "The Impact of Impurity Gases on the Hydrogen Embrittlement Behavior of Pipeline Steel in High-Pressure H2 Environments," *Materials*, vol. 17, no. 9, p. 2157, May 2024, doi: 10.3390/ma17092157.
[33] C. San Marchi, B. P. Somerday, K. A. Nibur, D. G. Stalheim, T. Boggess, and S. Jansto, "Fracture resistance and fatigue crack growth of X80 pipeline steel in gaseous hydrogen," presented at the Pressure Vessels and Piping Conference, 2011, pp. 841–849.
[34] B. Tekkaya, J. Wu, M. Dölz, J. Lian, and S. Münstermann, "Coupled chemical–mechanical damage modeling of hydrogen-induced material degradation," *Engineering Fracture Mechanics*, vol. 314, p. 110751, 2025.
[35] R. P. Gangloff and B. P. Somerday, *Gaseous hydrogen embrittlement of materials in energy technologies: mechanisms, modelling and future developments*. Elsevier, 2012.
[36] H. Cialone and J. Holbrook, "Sensitivity of steels to degradation in gaseous hydrogen," presented at the Hydrogen embrittlement: prevention and control, ASTM International, 1988, pp. 134–152.
[37] C. San Marchi, B. P. Somerday, K. A. Nibur, D. G. Stalheim, T. Boggess, and S. Jansto, "Fracture and fatigue of commercial grade API pipeline steels in gaseous hydrogen," presented at the Pressure vessels and piping conference, 2010, pp. 939–948.
[38] T. Li, H. Zhang, W. Hu, K. Li, Y. Wang, and Y. Lin, "Hydrogen Embrittlement Behavior and Applicability of X52 Steel in Pure Hydrogen Pipelines," *Materials*, vol. 18, no. 14, p. 3417, Jul. 2025, doi: 10.3390/ma18143417.
[39] A. Alvaro, V. Olden, A. Macadre, and O. M. Akselsen, "Hydrogen embrittlement susceptibility of a weld simulated X70 heat affected zone under H2 pressure," *Materials Science and Engineering: A*, vol. 597, pp. 29–36, Mar. 2014, doi: 10.1016/j.msea.2013.12.042.
[40] C. W. San Marchi and B. P. Somerday, "Technical reference for hydrogen compatibility of materials.," Sandia National Laboratories, 2012.
[41] R. L. Amaro, E. S. Drexler, and A. J. Slifka, "Fatigue crack growth modeling of pipeline steels in high pressure gaseous hydrogen," *International Journal of Fatigue*, vol. 62, pp. 249–257, 2014.
[42] T. Michler, C. Elsässer, K. Wackermann, and F. Schweizer, "Effect of Hydrogen in Mixed Gases on the Mechanical Properties of Steels—Theoretical Background and Review of Test Results," *Metals*, vol. 11, no. 11, p. 1847, Nov. 2021, doi: 10.3390/met11111847.
[43] S. Zhang *et al.*, "Investigating the influence mechanism of hydrogen partial pressure on fracture toughness and fatigue life by in-situ hydrogen permeation," *International Journal of Hydrogen Energy*, vol. 46, no. 39, pp. 20621–20629, 2021.
[44] R. A. Oriani, "The diffusion and trapping of hydrogen in steel," *Acta metallurgica*, vol. 18, no. 1, pp. 147–157, 1970.
[45] I. M. Robertson *et al.*, "Hydrogen Embrittlement Understood," *Metall Mater Trans A*, vol. 46, no. 6, pp. 2323–2341, Jun. 2015, doi: 10.1007/s11661-015-2836-1.
[46] M. Koyama *et al.*, "Recent progress in microstructural hydrogen mapping in steels: quantification, kinetic analysis, and multi-scale characterisation," *Materials Science and Technology*, vol. 33, no. 13, pp. 1481–1496, 2017.
[47] X. Li, X. Ma, J. Zhang, E. Akiyama, Y. Wang, and X. Song, "Review of Hydrogen Embrittlement in Metals: Hydrogen Diffusion, Hydrogen Characterization, Hydrogen Embrittlement

Mechanism and Prevention," *Acta Metall. Sin. (Engl. Lett.)*, vol. 33, no. 6, pp. 759–773, Jun. 2020, doi: 10.1007/s40195-020-01039-7.
[48] H. K. Birnbaum and P. Sofronis, "Hydrogen-enhanced localized plasticity—a mechanism for hydrogen-related fracture," *Materials Science and Engineering: A*, vol. 176, no. 1–2, pp. 191–202, 1994.
[49] M. L. Martin, Z. N. Buck, A. C. Eckhardt, D. S. Lauria, A. J. Slifka, and M. J. Connolly, "Effect of strain rate on tensile test results in hydrogen and other concerns," *Engineering Fracture Mechanics*, vol. 327, p. 111461, Oct. 2025, doi: 10.1016/j.engfracmech.2025.111461.
[50] H. Wei *et al.*, "Research on the fracture toughness of pipeline steel X80 in a hydrogen environment," *Engineering Failure Analysis*, vol. 180, p. 109917, Oct. 2025, doi: 10.1016/j.engfailanal.2025.109917.
[51] J. Ronevich, M. Agnani, and C. San Marchi, "Consistency of fatigue crack growth behavior of pipeline and low-alloy pressure vessel steels in gaseous hydrogen," *International Journal of Hydrogen Energy*, vol. 136, pp. 686–694, Jun. 2025, doi: 10.1016/j.ijhydene.2024.06.287.
[52] H. Tang *et al.*, "Fatigue crack growth behavior of X80 pipeline girth welded joints in natural gas/mixed hydrogen environment: Experimental and numerical investigations," *Corrosion Science*, vol. 252, p. 112959, 2025.
[53] J. Shang, J. Guo, B. Xing, R. Gao, and Z. Hua, "CO2 effect on the fatigue crack growth of X80 pipeline steel in hydrogen-enriched natural gas: Experiment vs DFT," *International Journal of Hydrogen Energy*, vol. 66, pp. 636–644, May 2024, doi: 10.1016/j.ijhydene.2024.04.116.
[54] H. Oesterlin, C. Fischer, and T. Michler, "Evaluation of Lifetime Predictions for Future Hydrogen Pipelines by Different Fracture Mechanics-Based Design Codes," *Energy Tech*, vol. 13, no. 2, p. 2301012, Feb. 2025, doi: 10.1002/ente.202301012.
[55] ASME B31. 12, "Hydrogen piping and pipelines," 2023.
[56] L. Paterlini, G. Re, A. Curia, M. Ormellese, and F. Bolzoni, "Mechanical Testing Methods for Assessing Hydrogen Embrittlement in Pipeline Steels: A Review," *Metals*, vol. 15, no. 10, p. 1123, Oct. 2025, doi: 10.3390/met15101123.
[57] J. Hoschke, M. F. W. Chowdhury, J. Venezuela, and A. Atrens, "A review of hydrogen embrittlement in gas transmission pipeline steels," *Corrosion Reviews*, vol. 41, no. 3, pp. 277–317, Jun. 2023, doi: 10.1515/corrrev-2022-0052.
[58] J. Venezuela, Q. Liu, M. Zhang, Q. Zhou, and A. Atrens, "A review of hydrogen embrittlement of martensitic advanced high-strength steels," *Corrosion Reviews*, vol. 34, no. 3, pp. 153–186, 2016.
[59] J. A. Ronevich, E. J. Song, B. P. Somerday, and C. W. San Marchi, "Hydrogen-assisted fracture resistance of pipeline welds in gaseous hydrogen," *International Journal of Hydrogen Energy*, vol. 46, no. 10, pp. 7601–7614, Feb. 2021, doi: 10.1016/j.ijhydene.2020.11.239.
[60] Z. Iyiola, R. Ahmed, C. Teodoriu, and N. Ahmed, "Developing a Novel Hybrid Ensemble Machine Learning Model for Predicting Reduced Elongation of Low-Carbon Steel in Hydrogen Environments," *Results in Materials*, p. 100871, 2025.
[61] N. Ahmed, R. Ahmed, S. Rhythm, A. F. B. Velasquez, and C. Teodoriu, "Experimental and Machine Learning-Based Assessment of Fatigue Crack Growth in API X60 Steel Under Hydrogen–Natural Gas Blending Conditions," *Metals*, vol. 15, no. 10, p. 1125, Oct. 2025, doi: 10.3390/met15101125.
[62] A. Campari, C. Vianello, F. Ustolin, A. Alvaro, and N. Paltrinieri, "Machine learning-aided risk-based inspection strategy for hydrogen technologies," *Process Safety and Environmental Protection*, vol. 191, pp. 1239–1253, Nov. 2024, doi: 10.1016/j.psep.2024.09.031.
[63] J. Yu, Z. Sun, Z.-H. Jin, Y.-F. Su, and H.-L. Shi, "Transfer Learning-Enhanced Physics-Informed Neural Networks for Predicting Fatigue Crack Growth in Hydrogen Pipelines," *Available at SSRN 5187020*.

[64] K. Ito, T. Otaki, T. Yokoi, K. Hyodo, and H. Mori, "Machine learning interatomic potential reveals hydrogen embrittlement origins at general grain boundaries in α-iron," *Commun Mater*, vol. 7, no. 1, p. 30, Dec. 2025, doi: 10.1038/s43246-025-01042-4.
[65] N. Ahmed, R. Ahmed, C. Teodoriu, and M. Gyaabeng, "Novel Machine Learning Modeling Approach for Fatigue Failure of Hydrogen-Transporting Pipelines," *SPE Journal*, vol. 30, no. 04, pp. 1549–1568, Apr. 2025, doi: 10.2118/220931-PA.
[66] J. Cristello, Z. Dang, R. Hugo, and S. S. Park, "Artificial intelligence based leak detection in blended hydrogen and natural gas pipelines," *International Journal of Hydrogen Energy*, vol. 91, pp. 744–764, 2024.
[67] R. P. Jewett, R. Walter, W. Chandler, and R. Frohmberg, "Hydrogen environment embrittlement of metals," 1973.
[68] H. F. Wachob and H. G. Nelson, "Influence of microstructure on the fatigue crack growth of A516 in hydrogen," presented at the Proceedings of the third international conference on effect of hydrogen on behavior of materials, 1980.
[69] W. Hoover, S. Robinson, R. Stoltz, and J. Spingarn, "Hydrogen compatibility of structural materials for energy storage and transmission," *NASA STI/Recon Technical Report N*, vol. 81, p. 29598, 1981.
[70] A. W. Loginow and E. H. Phelps, "Steels for Seamless Hydrogen Pressure Vessels," *Journal of Engineering for Industry*, vol. 97, no. 1, pp. 274–282, Feb. 1975, doi: 10.1115/1.3438550.
[71] R. Walter and W. Chandler, "Cyclic-load crack growth in ASME SA-105 grade II steel in high-pressure hydrogen at ambient temperature," presented at the Effect of hydrogen on behavior of materials, 1976.
[72] W. Clark and J. Landes, "An Evaluation of Rising Load *K* Iscc Testing," in *Stress Corrosion—New Approaches*, ASTM International100 Barr Harbor Drive, PO Box C700, West Conshohocken, PA 19428-2959, 1976, pp. 108–127. doi: 10.1520/STP28674S.
[73] R. Padmanabhan and W. E. Wood, "Hydrogen induced cracking in a low alloy steel," *Metall Trans A*, vol. 14, no. 11, pp. 2347–2356, Nov. 1983, doi: 10.1007/BF02663310.
[74] N. Bandyopadhyay, J. Kameda, and C. J. Mcmahon, "Hydrogen-induced cracking in 4340-type steel: Effects of composition, yield strength, and H2 pressure," *Metall Trans A*, vol. 14, no. 4, pp. 881–888, Apr. 1983, doi: 10.1007/BF02644292.
[75] S. L. Robinson, "Hydrogen compatibility of structural materials for energy storage and transmission applications," *Chemical/Hydrogen Energy Systems Contractor Review*, p. 146, 1978.
[76] Y. Takeda and C. J. McMahon, "Strain controlled vs stress controlled hydrogen induced fracture in a quenched and tempered steel," *Metall Trans A*, vol. 12, no. 7, pp. 1255–1266, Jul. 1981, doi: 10.1007/BF02642339.
[77] J. E. Campbell, "Effects of Hydrogen Gas on Metals at Ambient Temperature," 1970.
[78] X. Xu, R. Zhang, C. Wang, C. Liu, J. Zhang, and Y. Li, "Experimental study on the temperature dependence of gaseous hydrogen permeation and hydrogen embrittlement susceptibility of X52 pipeline steel," *Engineering Failure Analysis*, vol. 155, p. 107746, 2024.
[79] G. Álvarez, L. B. Peral, C. Rodríguez, T. E. García, and F. J. Belzunce, "Hydrogen embrittlement of structural steels: Effect of the displacement rate on the fracture toughness of high-pressure hydrogen pre-charged samples," *International Journal of Hydrogen Energy*, vol. 44, no. 29, pp. 15634–15643, Jun. 2019, doi: 10.1016/j.ijhydene.2019.03.279.
[80] G. Álvarez, A. Zafra, F. J. Belzunce, and C. Rodríguez, "Hydrogen embrittlement testing procedure for the analysis of structural steels with Small Punch Tests using notched specimens," *Engineering Fracture Mechanics*, vol. 253, p. 107906, Aug. 2021, doi: 10.1016/j.engfracmech.2021.107906.

[81] A. J. Duncan, T. M. Adams, and P.-S. Lam, "Fracture property testing of carbon steel in high pressure hydrogen," presented at the ASME Pressure Vessels and Piping Conference, 2009, pp. 225–231.
[82] F. Gutierrez-Solana and M. Elices, "High-pressure hydrogen behavior of a pipeline steel," *Current solutions to hydrogen problems in steels*, pp. 181–185, 1982.
[83] Y. Nishihara and H. Okano, "Effect of high pressure hydrogen gas on fatigue and fracture properties of API X65 linepipe steels," presented at the Pressure Vessels and Piping Conference, American Society of Mechanical Engineers, 2023, p. V005T06A067.
[84] L. Peral, A. Zafra, J. Belzunce, and C. Rodríguez, "Effects of hydrogen on the fracture toughness of CrMo and CrMoV steels quenched and tempered at different temperatures," *International journal of hydrogen energy*, vol. 44, no. 7, pp. 3953–3965, 2019.
[85] R. Zawierucha and K. Xu, "Hydrogen pipeline steels," *MATERIALS SCIENCE AND TECHNOLOGY-ASSOCIATION FOR IRON AND STEEL TECHNOLOGY-*, vol. 3, p. 5, 2005.
[86] H. Nelson, "On the mechanism of hydrogen-enhanced crack growth in ferritic steels," presented at the Proceedings of the Second International Conference on Mechanical Behavior of Materials, ASM, Metals Park, OH, 1976, pp. 690–694.
[87] H. Nelson, "Hydrogen-induced slow crack growth of a plain carbon pipeline steel under conditions of cyclic loading," presented at the Effect of hydrogen on behavior of materials, 1976.
[88] R. Walter and W. Chandler, "Influence of gaseous hydrogen on metals," 1973.
[89] B. Somerday, C. San Marchi, and K. Nibur, "Measurement of fatigue crack growth rates for SA-372 Gr. J steel in 100 MPa hydrogen gas following article KD-10," presented at the Pressure Vessels and Piping Conference, American Society of Mechanical Engineers, 2013, p. V06BT06A016.
[90] J. A. Ronevich, B. P. Somerday, and Z. Feng, "Hydrogen accelerated fatigue crack growth of friction stir welded X52 steel pipe," *International Journal of Hydrogen Energy*, vol. 42, no. 7, pp. 4259–4268, 2017.
[91] J. A. Ronevich, B. P. Somerday, and C. W. San Marchi, "Effects of microstructure banding on hydrogen assisted fatigue crack growth in X65 pipeline steels," *International Journal of Fatigue*, vol. 82, pp. 497–504, 2016.
[92] L. Breiman, "Random Forests," *Machine Learning*, vol. 45, no. 1, pp. 5–32, Oct. 2001, doi: 10.1023/A:1010933404324.
[93] S. K. Murthy, "Automatic Construction of Decision Trees from Data: A Multi-Disciplinary Survey," *Data Mining and Knowledge Discovery*, vol. 2, no. 4, pp. 345–389, Dec. 1998, doi: 10.1023/A:1009744630224.
[94] T. Cover and P. Hart, "Nearest neighbor pattern classification," *IEEE Trans. Inform. Theory*, vol. 13, no. 1, pp. 21–27, Jan. 1967, doi: 10.1109/TIT.1967.1053964.
[95] A. Natekin and A. Knoll, "Gradient boosting machines, a tutorial," *Front. Neurorobot.*, vol. 7, 2013, doi: 10.3389/fnbot.2013.00021.
[96] J. H. Friedman, "Greedy function approximation: A gradient boosting machine.," *Ann. Statist.*, vol. 29, no. 5, Oct. 2001, doi: 10.1214/aos/1013203451.
[97] L. Prokhorenkova, G. Gusev, A. Vorobev, A. V. Dorogush, and A. Gulin, "CatBoost: unbiased boosting with categorical features," *Advances in neural information processing systems*, vol. 31, 2018.
[98] J. T. Hancock and T. M. Khoshgoftaar, "CatBoost for big data: an interdisciplinary review," *J Big Data*, vol. 7, no. 1, p. 94, Dec. 2020, doi: 10.1186/s40537-020-00369-8.
[99] T. Chen and C. Guestrin, "XGBoost: A Scalable Tree Boosting System," in *Proceedings of the 22nd ACM SIGKDD International Conference on Knowledge Discovery and Data Mining*, San Francisco California USA: ACM, Aug. 2016, pp. 785–794. doi: 10.1145/2939672.2939785.

[100] H. Drucker, C. J. Burges, L. Kaufman, A. Smola, and V. Vapnik, "Support vector regression machines," *Advances in neural information processing systems*, vol. 9, 1996.
[101] L. Rokach, "Ensemble-based classifiers," *Artif Intell Rev*, vol. 33, no. 1–2, pp. 1–39, Feb. 2010, doi: 10.1007/s10462-009-9124-7.
[102] T. G. Dietterich, "Ensemble Methods in Machine Learning," in *Multiple Classifier Systems*, vol. 1857, in Lecture Notes in Computer Science, vol. 1857. , Berlin, Heidelberg: Springer Berlin Heidelberg, 2000, pp. 1–15. doi: 10.1007/3-540-45014-9_1.
[103] M. B. Djukic, G. M. Bakic, V. S. Zeravcic, A. Sedmak, and B. Rajicic, "The synergistic action and interplay of hydrogen embrittlement mechanisms in steels and iron: Localized plasticity and decohesion," *Engineering fracture mechanics*, vol. 216, p. 106528, 2019.
[104] J. R. Fekete, J. W. Sowards, and R. L. Amaro, "Economic impact of applying high strength steels in hydrogen gas pipelines," *International Journal of Hydrogen Energy*, vol. 40, no. 33, pp. 10547–10558, Sep. 2015, doi: 10.1016/j.ijhydene.2015.06.090.
[105] American Society of Mechanical Engineers, *API 579-1/ASME FFS-1 Fitness-For-Service*. American Society of Mechanical Engineers, 2016.
[106] ASME B31. 12, "Hydrogen piping and pipelines," 2023.
[107] B. C. Erdener *et al.*, "A review of technical and regulatory limits for hydrogen blending in natural gas pipelines," *International Journal of Hydrogen Energy*, vol. 48, no. 14, pp. 5595–5617, Feb. 2023, doi: 10.1016/j.ijhydene.2022.10.254.
[108] T. L. Anderson and T. L. Anderson, *Fracture mechanics: fundamentals and applications*. CRC press, 2005.
[109] T. L. Anderson and T. L. Anderson, *Fracture mechanics: fundamentals and applications*. CRC press, 2005.
[110] J. C. Newman and I. S. Raju, "An empirical stress-intensity factor equation for the surface crack," *Engineering Fracture Mechanics*, vol. 15, no. 1–2, pp. 185–192, Jan. 1981, doi: 10.1016/0013-7944(81)90116-8.
[111] E. Folias, "On the effect of initial curvature on cracked flat sheets," *International Journal of Fracture Mechanics*, vol. 5, no. 4, pp. 327–346, 1969.
[112] A. J. Slifka *et al.*, "Fatigue measurement of pipeline steels for the application of transporting gaseous hydrogen," *Journal of Pressure Vessel Technology*, vol. 140, no. 1, p. 011407, 2018.
[113] E. Drexler, A. Slifka, R. Amaro, D. Lauria, and J. W. Sowards, "Fatigue crack growth rates of API X70 pipeline steels in pressurized hydrogen gas compared with an X52 pipeline in hydrogen service," presented at the Int. Hydrog. Conf.(IHC 2016) Mater. Perform. Hydrog. Environ, 2017, pp. 210–218.
[114] C. Fischer *et al.*, "Codes and standards for the fatigue-based design of hydrogen infrastructure components," *International Journal of Fatigue*, vol. 171, p. 107564, Jun. 2023, doi: 10.1016/j.ijfatigue.2023.107564.
[115] S. Rhythm, R. Ahmed, N. Ahmed, M. Gyaabeng, and C. Teodoriu, "Experimental study of the impact of hydrogen embrittlement on the ductility of natural gas pipeline steels," *Gas Science and Engineering*, vol. 143, p. 205746, Nov. 2025, doi: 10.1016/j.jgsce.2025.205746.
[116] C. W. San Marchi and B. P. Somerday, "Technical reference for hydrogen compatibility of materials.," Sandia National Laboratories, 2012.

APPENDIX A

OU HEAT GRAPHICAL USER INTERFACE

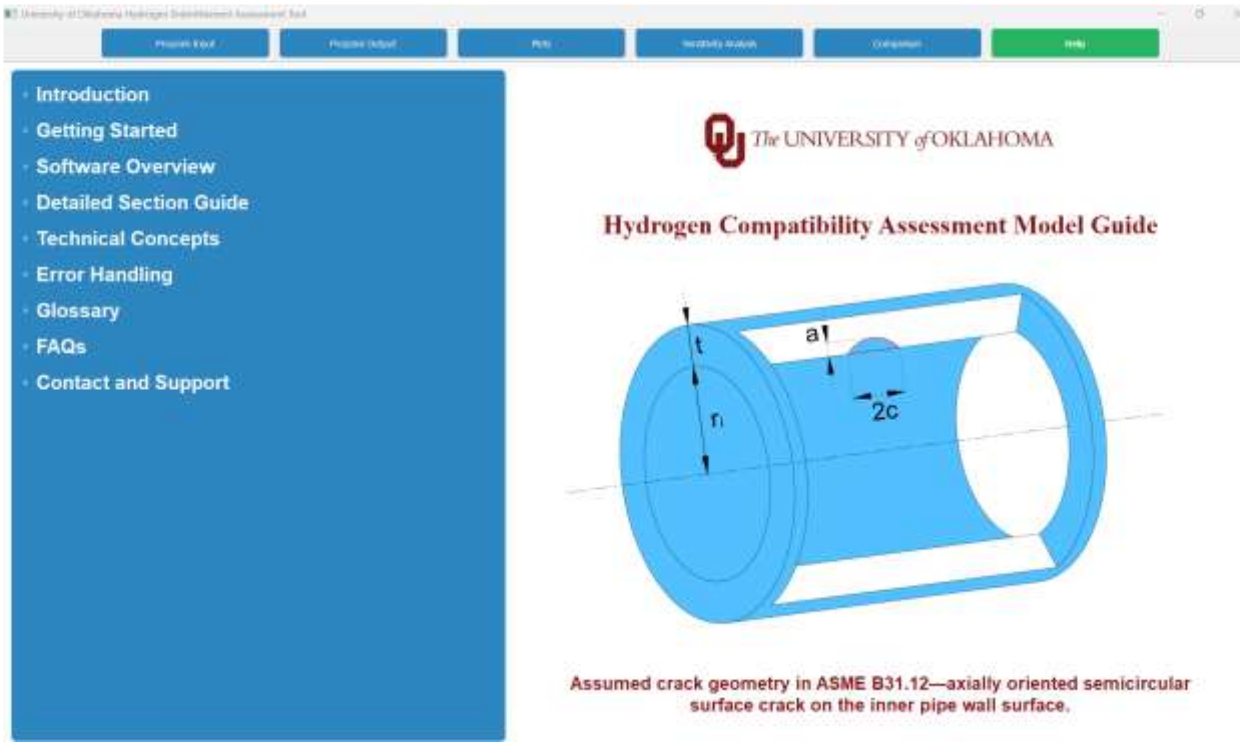

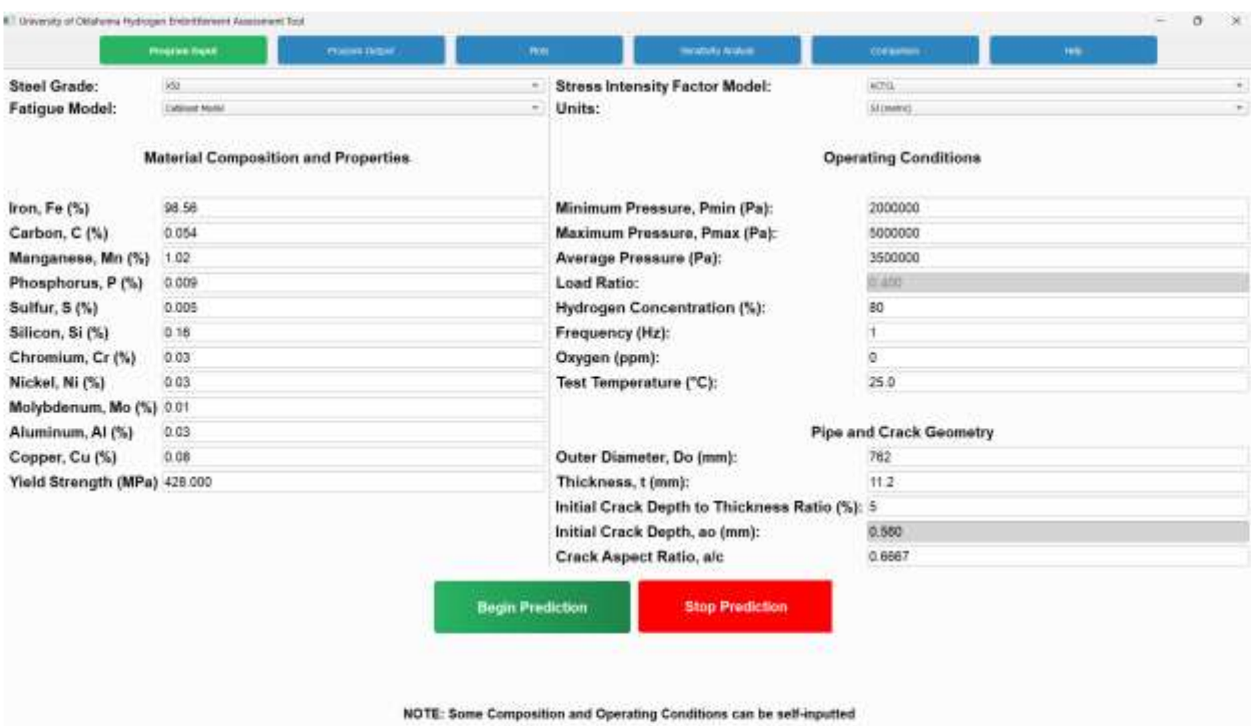

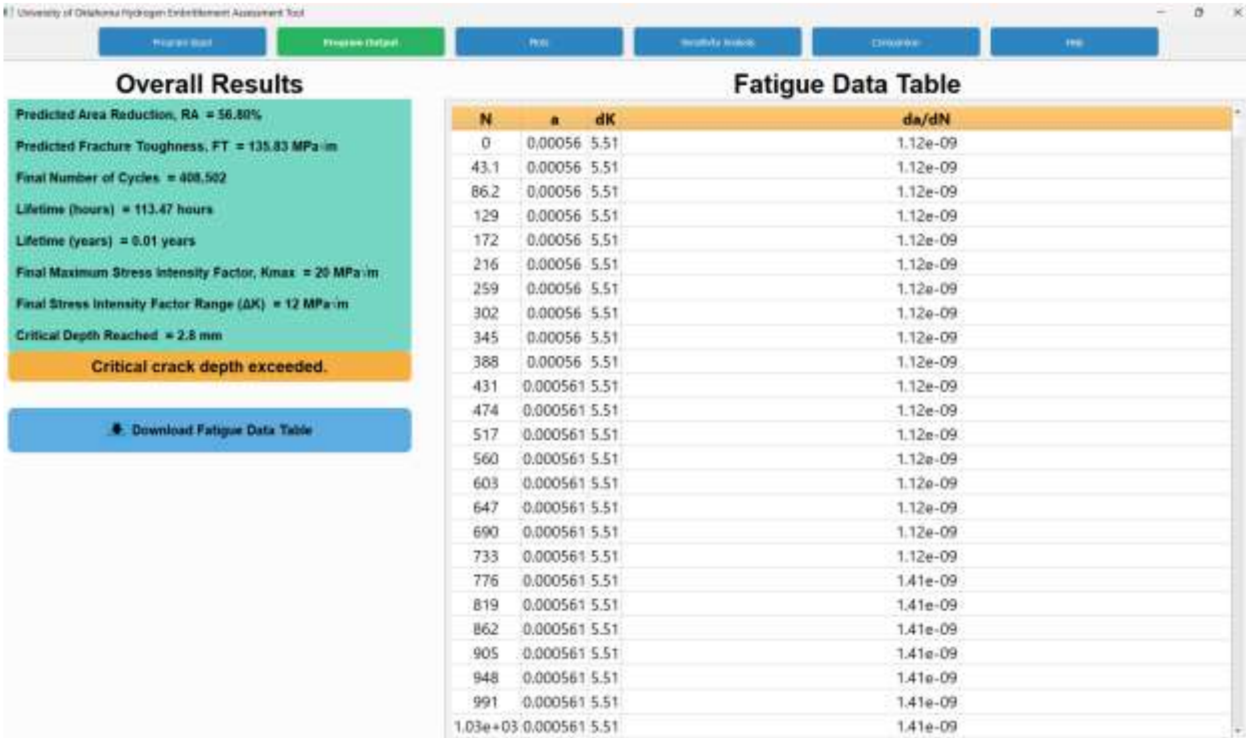
Overall Results
Predicted Area Reduction, RA = 56.80%
Predicted Fracture Toughness, FT = 135.83 MPa√m
Final Number of Cycles = 408,502
Lifetime (hours) = 113.47 hours
Lifetime (years) = 0.01 years
Final Maximum Stress Intensity Factor, Kmax = 20 MPa√m
Final Stress Intensity Factor Range (ΔK) = 12 MPa√m
Critical Depth Reached = 2.8 mm
Critical crack depth exceeded.
Download Fatigue Data Table
Fatigue Data Table
N a dK da/dN
0 0.00056 5.51 1.12e-09
43.1 0.00056 5.51 1.12e-09
86.2 0.00056 5.51 1.12e-09
129 0.00056 5.51 1.12e-09
172 0.00056 5.51 1.12e-09
216 0.00056 5.51 1.12e-09
259 0.00056 5.51 1.12e-09
302 0.00056 5.51 1.12e-09
345 0.00056 5.51 1.12e-09
388 0.00056 5.51 1.12e-09
431 0.000561 5.51 1.12e-09
474 0.000561 5.51 1.12e-09
517 0.000561 5.51 1.12e-09
560 0.000561 5.51 1.12e-09
603 0.000561 5.51 1.12e-09
647 0.000561 5.51 1.12e-09
690 0.000561 5.51 1.12e-09
733 0.000561 5.51 1.12e-09
776 0.000561 5.51 1.41e-09
819 0.000561 5.51 1.41e-09
862 0.000561 5.51 1.41e-09
905 0.000561 5.51 1.41e-09
948 0.000561 5.51 1.41e-09
991 0.000561 5.51 1.41e-09
1.03e+03 0.000561 5.51 1.41e-09

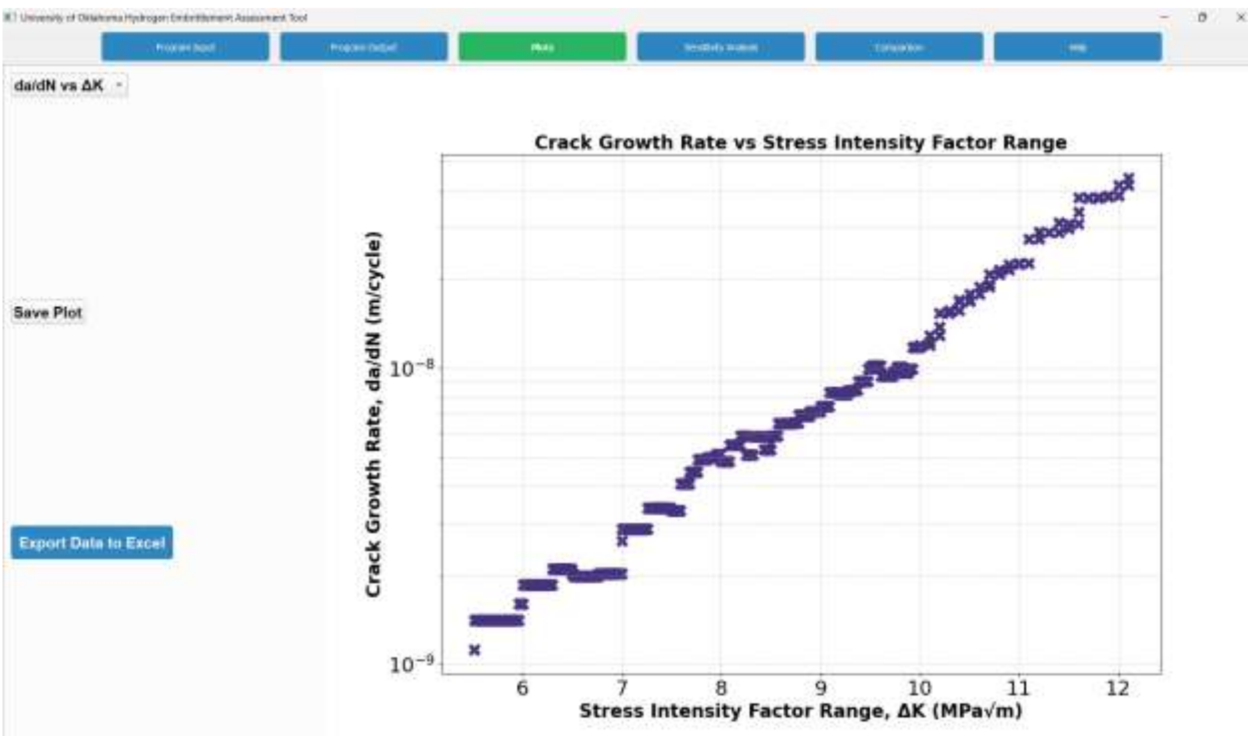
da/dN vs ΔK
Save Plot
Export Data to Excel
Crack Growth Rate vs Stress Intensity Factor Range
Crack Growth Rate, da/dN (m/cycle)
10^-8
10^-9
6
7
8
9
10
11
12
Stress Intensity Factor Range, ΔK (MPa√m)

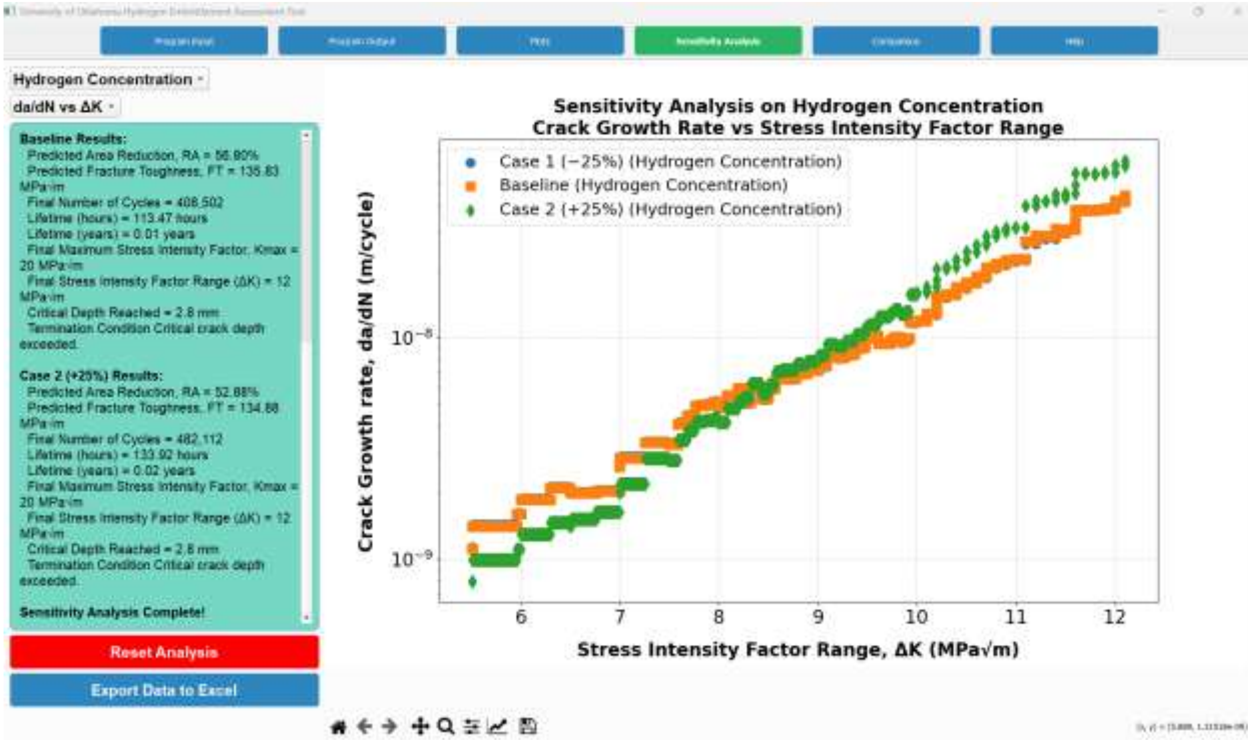
Hydrogen Concentration
da/dN vs ΔK
Baseline Results:
Predicted Area Reduction, RA = 56.80%
Predicted Fracture Toughness, FT = 135.83 MPa√m
Final Number of Cycles = 408,502
Lifetime (hours) = 113.47 hours
Lifetime (years) = 0.01 years
Final Maximum Stress Intensity Factor, Kmax = 20 MPa√m
Final Stress Intensity Factor Range (ΔK) = 12 MPa√m
Critical Depth Reached = 2.8 mm
Termination Condition Critical crack depth exceeded.
Case 2 (+25%) Results:
Predicted Area Reduction, RA = 52.88%
Predicted Fracture Toughness, FT = 134.88 MPa√m
Final Number of Cycles = 482,112
Lifetime (hours) = 133.92 hours
Lifetime (years) = 0.02 years
Final Maximum Stress Intensity Factor, Kmax = 20 MPa√m
Final Stress Intensity Factor Range (ΔK) = 12 MPa√m
Critical Depth Reached = 2.8 mm
Termination Condition Critical crack depth exceeded.
Sensitivity Analysis Complete!
Reset Analysis
Export Data to Excel
Sensitivity Analysis on Hydrogen Concentration
Crack Growth Rate vs Stress Intensity Factor Range
Case 1 (−25%) (Hydrogen Concentration)
Baseline (Hydrogen Concentration)
Case 2 (+25%) (Hydrogen Concentration)
Crack Growth rate, da/dN (m/cycle)
10⁻⁸
10⁻⁹
6
7
8
9
10
11
12
Stress Intensity Factor Range, ΔK (MPa√m)

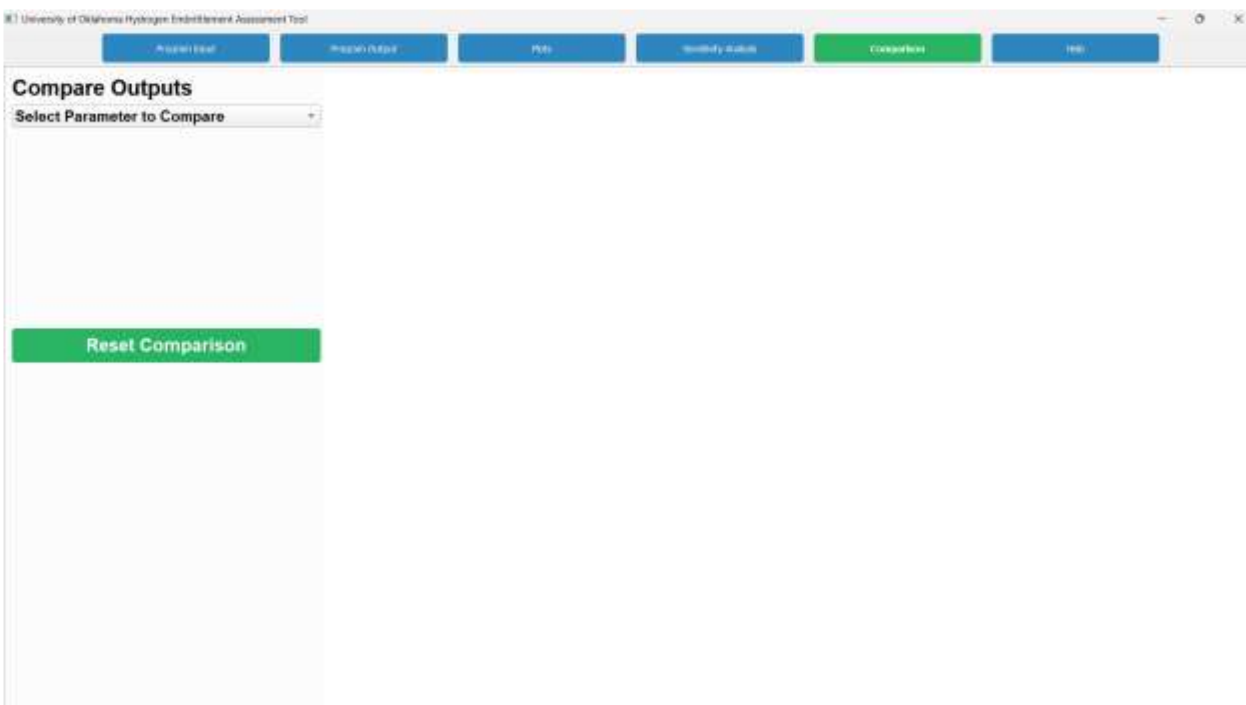
Compare Outputs
Select Parameter to Compare
Reset Comparison